Correlated Electron-Nuclear Dynamics

Dissertation

zur Erlangung des akademischen Grades

Doctor rerum naturalium

vorgelegt von

Ali Abedi Khaledi

Fachbereich Physik

Institut für Theoretische Physik

Freie Universität Berlin

Juli 2013

Erstgutacher: Prof. Dr. E. K. U. Gross

Zweitgutachter: Prof. Dr. J. Bosse

Datum der Disputation: 11. Juli 2013

Declaration of Authorship

Eigenständigkeitserklärung
Hiermit versichere ich, dass ich die vorliegende Dissertationsschrift mit dem Titel "Correlated Electron-Nuclear Dynamics" selbständig und ohne die Benutzung anderer als der angegeben Hilfsmittel angefertigt habe. Die Stellen der Arbeit, die dem Wortlaut oder dem Sinn nach anderen Werken entnommen sind, wurden unter Angabe der Quelle kenntlich gemacht.

Berlin, den 01.06.2013

To the loving memory of my father,

Madjid Abedi Khaledi (1956-2011),

who taught me how to sail through the big waves.

Abstract

With the goal of full ab initio treatment of the coupled electron-nuclear system, exposed to a time-dependent external potential, we present an exact factorization of the complete wavefunction, into a nuclear wavefunction and an electronic wavefunction. Exact equations for these wavefunctions are deduced that lead to rigorous definitions of a time-dependent potential energy surface (TDPES) and a time-dependent vector potential. This representation of the correlated electron-nuclear many-body problem is very appealing as the wavefunction satisfying the exact nuclear equation of motion leads to an N-body density and an N-body current density which reproduce the true nuclear N-body density and current density obtained from the full wavefunction of the coupled electron-nuclear system. The time evolution of the nuclear wavefunction, on the other hand, is completely determined by the TDPES and the time-dependent vector potential. Moreover, these potentials are *unique* up to within a gauge transformation. In other words, if one wants a time-dependent Schrödinger equation whose solution yields the true nuclear N-body density and current density, then the potentials appearing in this equation are (up to within a gauge transformation) uniquely given by the TDPES and time-dependent vector potential; there is no other choice. We investigate the relationship of this exact factorization to the traditional Born-Oppenheimer expansion. We furthermore study the exact TDPES in two topically demanding situations: molecules in strong fields and splitting of a nuclear wave-packet at avoided crossings of Born-Oppenheimer potential energy surfaces. We show how the TDPES for the H_2^+ molecular ion exposed to a laser field helps to identify different mechanisms of dissociation. In addition, we show that the TDPES exhibits a dynamical step that bridges piecewise adiabatic shapes when the nuclear wave-packet splits at the avoided crossing of two Born-Oppenheimer potential energy surfaces. These studies provide us with the essential elements (fundamental equations of motion and insights of the coupling potentials) for making approximations, especially for the systematic development of (semi-)classical approximations. Starting from the exact equations, we develop a mixed quantum-classical scheme to treat the coupled electron-nuclear dynamics, by taking the classical limit of the nuclear motion. We evaluate the performance of the approach in comparison with numerically exact results and provide a detailed analysis of the classical limit of the nuclear motion.

Revisiting the exact decomposition in the static case [1], we investigate the exact static potential energy surfaces in situations in which the corresponding adiabatic potential energy surfaces are strongly coupled due to conical intersections or avoided crossings. We show that in those situations the exact static surfaces have the shape of diabatic surfaces.

Contents

List of Figures

List of Tables

Abbreviations

BO	Born-Oppenheimer
PES	Potential Energy Surface
BOPES	Born-Oppenheimer Potential Energy Surface
NAC	Non-Adiabatic Couplings
EPES	Exact Potential Energy Surface
GBO	Generalized Born-Oppenheimer
GI	Gauge-Invariant
GD	Gauge-Dependent
TDSE	Time-Dependent Schrödinger Equation
TDPES	Time-Dependent Potential Energy Surface
PNC	Partial Normalization Condition
MQC	Mixed Quantum Classical
TSH	Tullys Surface Hopping
MQC	Mixed Quantum-Classical
ST	Single Trajectory
MT	Multiple Trajectory
r.h.s	right hand side
l.h.s	left hand side
a.u.	atomic units

Chapter 1

Introduction

The concept of non-adiabatic transition [2–7] has been widely used to describe dynamical processes. This concept has its root in the *adiabatic* treatment of dynamical processes in which the complete system is approximately decomposed to two parts based on the assumption that part of the system usually changes on a much shorter time-scale than the rest and hence can be assumed to adjust instantaneously to the *adiabatic* changes of the rest. "The fast part" of the system, within the adiabatic approximation, depends on "the rest" only via an environmental parameter that represents the adiabatically slow changes of "the rest" compare to the time-scale in which "the fast part" changes. This implies that "the fast part" is treated independently for each environmental parameter that represents a specific configuration of "the rest". However, this ideal picture may break down in different situations in which the coupling between "the fast part" and "the rest" is more than an adiabatic coupling via a parameter. This is when the concepts such as "non-adiabatic coupling" (NAC) and "non-adiabatic transition" between the adiabatic states come to remedy the adiabatic approximation and describe the dynamical processes. For example, in the Born-Oppenheimer (BO) approximation [8], the fast motion of light electrons is separated from the much slower motion of heavy nuclei and the Hamiltonian that describes the electronic motion has a parametric dependence on the nuclear configuration. This is justified by assuming that the electrons remain in their instantaneous eigenstate as the nuclear rearrangement occurs adiabatically slowly. This allows one to visualize a molecule or solid as a set of nuclei moving on a single potential energy surface (PES) generated by the electrons in a given eigenstate. However, the adiabatic theorem also requires the electronic eigenvalue to be well separated from the rest of its Hamiltonian's spectrum by a gap. This condition, as a matter of fact,

happens to be violated often in physics, chemistry and biology leading to a plethora of fascinating phenomena that lie beyond the Born-Oppenheimer approximation. The interplay of electronic and nuclear degrees of freedom in solids, i.e., electron-phonon coupling, may mediate electron pairing leading to superconductivity. Strong laser fields can induce strong coupling between the electronic and nuclear motions in molecules, leading to nonlinear processes such as photo-induced molecular dissociation, charge-resonance enhanced ionization, electron-hole migration after photo-excitation [9–13]. Some of the most fascinating and challenging molecular processes in femto-chemistry occur in the regime where the BO approximation is not valid, e.g., ultrafast nuclear motion through conical intersections [4], radiationless relaxation of excited electronic states [14, 15], intra- and inter-molecular electron and proton transfer [6, 7, 16], to name a few. Many of the very exciting biological processes also fall beyond the adiabatic approximation. The process of vision, for example, begins with the photoisomerization of retinal, i.e, via absorption of a photon the 11-cis retinal chromophore is excited to a higher electronic state and isomerizes to the all-trans state.

The theoretical description of electron-nuclear correlations in molecules and solids is a major challenge. A numerically accurate solution of the time-dependent Schrödinger equation provides the complete information on the system, but it is only tractable for very small molecules, such as H_2^+ and lacks the intuitive picture that PESs can provide. The standard way of studying and interpreting "non-adiabatic" processes is to expand the full wavefunction in terms of the BO states. Within this expansion, non-adiabatic processes can be viewed as a nuclear wave packet with contributions on several electronic states, coupled through the non-adiabatic coupling terms which in turn induce transitions between the electronic states. This, in principle, provides an exact description of the non-adiabatic processes. In practice, however, one is mostly restricted to the use of only a few electronic states, and even then it is applicable only to systems with a few nuclear degrees of freedom.

In order to describe non-adiabatic dynamical processes in systems with several nuclear degrees of freedom, approximations are inevitable to make the calculations feasible. Classical or semi-classical treatments of the nuclear motion that is coupled, non-adiabatically, to the electronic motion are among the most promising practical approaches, especially

to treat large systems with many nuclear degrees of freedom. In developing such approximations, several complications arise. The main concern is the separation of the electronic and nuclear motions and how to account for the effect of electronic non-adiabatic transitions on the classical nuclei.

As the central idea of this work, we propose a rigorous separation of electronic and nuclear motion by introducing an *exact* factorization of the full electron-nuclear wavefunction and derive formally exact equations for the nuclear and electronic wavefunctions that lead to rigorous definitions of a time-dependent potential energy surface (TDPES) and a time-dependent vector potential [17, 18]. In Chapter (2) of this work, we present a detailed description of the formalism (Section 2.2), including a full derivation of the equations that the electronic and nuclear wavefunctions satisfy and demonstrate the relationship of this exact factorization to the traditional BO expansion.

Our work here is a natural extension of the work of Hunter [19], in which an exact decomposition was developed for the static problem. Chapter (3) of this thesis serves to review the exact factorization for the static case and present some important features of the exact static PESs that have not been shown before.

The novel concepts of an exact TDPES and exact time-dependent vector potential are the key elements of the equation that governs the nuclear dynamics. In Chapter (4), we present a detailed study of the TDPES in various situations [18, 20, 21].

The exact splitting of electronic and nuclear degrees of freedom lends itself as a rigorous starting point for making approximations, especially for the systematic development of (semi)classical approximations. As a first step on this path, in Chapter (4), we present a mixed quantum-classical (MQC) scheme to treat the correlated electron-nuclear dynamics [22]. The performance of the scheme as well as the validity of the classical approximation are examined numerically.

Chapter 2

Exact Factorization of the Electron-Nuclear Wave-Function

A multicomponent system of N_e electrons and N_n nuclei out of equilibrium is in, non-relativistic quantum mechanics, described by the time-dependent Schrödinger equation (TDSE),

$$\hat{H}|\Psi>= i\hbar\partial_t|\Psi> . \tag{2.1}$$

It this chapter, we show that the complete electron-nuclear wavefunction for the combined system of electrons and nuclei evolving in a time-dependent external potential can be exactly factorized into an electronic wavefunction and a nuclear wavefunction. The concepts of an exact TDPES and exact time-dependent vector potential emerge naturally from the formalism. Here we present a detailed description of the formalism (Section 2.2), including a full derivation of the equations that the electronic and nuclear wavefunctions satisfy. Then we analyse features of the exact electron-nuclear coupling terms in general (Section 2.3), and demonstrate the relationship of this exact factorization to the traditional BO expansion. We close the chapter by discussing the exact factorization for the static case. The following section serves to set up the problem at hand, and review the BO approximation.

2.1 The Hamiltonian

In this section we introduce the notation and define the Hamiltonian for the combined system of electrons and nuclei. The coordinates of the N_e electrons are collectively denoted by $\underline{\underline{\mathbf{r}}}\,\underline{\underline{\mathbf{s}}}$ where $\underline{\underline{\mathbf{r}}} \equiv \{r_j\}$ and $\underline{\underline{\mathbf{s}}} \equiv \{s_j\}, j = 1...N_e$, represent electronic spatial and spin

coordinates, respectively. The N_n nuclei have masses $M_1...M_{N_n}$ and charges $Z_1...Z_{N_n}$ and coordinates collectively denoted by $\underline{\underline{\mathbf{R}}}\,\underline{\sigma}$ where $\underline{\underline{\mathbf{R}}} \equiv \{R_\alpha\}$ and $\underline{\sigma} \equiv \{\sigma_\alpha\}, \alpha = 1...N_n$, represent nuclear spatial and spin coordinates, respectively. Furthermore, we consider the system is under the influence of some time-dependent external scalar field. The system is described, non-relativistically, by the Hamiltonian

$$\hat{H} = \hat{H}_{BO}(\underline{\mathbf{r}}, \underline{\underline{\mathbf{R}}}) + \hat{V}_e^{ext}(\underline{\mathbf{r}}, t) + \hat{T}_n(\underline{\underline{\mathbf{R}}}) + \hat{V}_n^{ext}(\underline{\underline{\mathbf{R}}}, t)\,, \tag{2.2}$$

where $\hat{H}_{BO}(\underline{\mathbf{r}}, \underline{\underline{\mathbf{R}}})$ is the familiar BO electronic Hamiltonian,

$$\hat{H}_{BO}(\underline{\mathbf{r}}, \underline{\underline{\mathbf{R}}}) = \hat{T}_e(\underline{\mathbf{r}}) + \hat{W}_{ee}(\underline{\mathbf{r}}) + \hat{W}_{en}(\underline{\mathbf{r}}, \underline{\underline{\mathbf{R}}}) + \hat{W}_{nn}(\underline{\underline{\mathbf{R}}}). \tag{2.3}$$

The subscripts "e" and "n" refer to electrons and nuclei, respectively, and atomic units are used throughout ($e^2 = \hbar = m_e = 1$). Here

$$\hat{T}_e = -\sum_{j=1}^{N_e} \frac{1}{2}\nabla_j^2 \tag{2.4}$$

and

$$\hat{T}_n = -\sum_{\alpha=1}^{N_n} \frac{1}{2M_\alpha}\nabla_\alpha^2 \tag{2.5}$$

denote the kinetic-energy operators of the electrons and nuclei, respectively. All external scalar potentials on the system (e.g. electric fields) are represented by

$$\hat{V}_n^{ext} = \sum_{\alpha}^{N_n} v_n^{ext}(\boldsymbol{R}_\alpha, t)\,, \tag{2.6}$$

and

$$\hat{V}_e^{ext} = \sum_{j}^{N_e} v_e^{ext}(\boldsymbol{r}_j, t). \tag{2.7}$$

The particle-particle Coulomb interactions have the form:

$$\hat{W}_{nn} = \frac{1}{2}\sum_{\substack{\alpha,\beta=1 \\ \alpha\neq\beta}}^{N_n} \frac{Z_\alpha Z_\beta}{|\boldsymbol{R}_\alpha - \boldsymbol{R}_\beta|}\,, \tag{2.8}$$

$$\hat{W}_{ee} = \frac{1}{2}\sum_{\substack{i,j=1 \\ i\neq j}}^{N_e} \frac{1}{|\boldsymbol{r}_i - \boldsymbol{r}_j|}\,, \tag{2.9}$$

$$\hat{W}_{en} = -\sum_{j}^{N_e}\sum_{\alpha}^{N_n}\frac{Z_\alpha}{|\boldsymbol{r}_j - \boldsymbol{R}_\alpha|}\,. \tag{2.10}$$

The quantum mechanical equation of motion of such a system is given by the TDSE:

$$\hat{H}\Psi(\underline{\mathbf{r}}\ \underline{\mathbf{s}}, \underline{\underline{\mathbf{R}}}\ \underline{\sigma}, t) = i\partial_t\Psi(\underline{\mathbf{r}}\ \underline{\mathbf{s}}, \underline{\underline{\mathbf{R}}}\ \underline{\sigma}, t) \tag{2.11}$$

The full electron-nuclear wavefunction, $\Psi(\underline{\mathbf{r}}\ \underline{\mathbf{s}}, \underline{\underline{\mathbf{R}}}\ \underline{\sigma}, t)$, that satisfies the TDSE (2.11), have been given for very small systems like H_2^+ [23, 24]. The analysis of the full time-dependent wavefunction provides important clues to understand the dynamical behavior of the system, and includes quantum features of the nuclear dynamics (e.g. zero-point energies, tunneling, and interference). However, knowing the full wavefunction lacks the intuitive picture that the PES can provide.

2.1.1 The Born-Oppenheimer Approximation

The BO approximation is among the most basic approximations in the quantum theory of molecules and solids. Consider the case when there is no external time-dependence in the Hamiltonian. The BO approximation relies on the fact that electrons typically move much faster than the nuclei; on the timescale of nuclear motion, the electrons "instantly" adjust to remain on the instantaneous eigenstate. This "adiabatic approximation" allows us to visualize a molecule or solid as a set of nuclei moving on the PES generated by the electrons in a specific electronic eigenstate. The electronic Hamiltonian $H_{BO}(\underline{\mathbf{r}}, \underline{\underline{\mathbf{R}}})$ depends parametrically on the nuclear positions, via the electron-nuclear Coulomb interaction. That is, the stationary electronic Schrödinger equation is solved for each fixed nuclear configuration $\underline{\underline{\mathbf{R}}}\ \underline{\sigma}$,

$$\hat{H}_{BO}(\underline{\underline{\mathbf{R}}}\ \underline{\sigma})\phi^j_{\underline{\underline{\mathbf{R}}}\ \underline{\sigma}}(\underline{\mathbf{r}}\ \underline{\mathbf{s}}) = \epsilon^j_{BO}(\underline{\underline{\mathbf{R}}}\ \underline{\sigma})\phi^j_{\underline{\underline{\mathbf{R}}}\ \underline{\sigma}}(\underline{\mathbf{r}}\ \underline{\mathbf{s}}) \tag{2.12}$$

yielding $(\underline{\underline{\mathbf{R}}}\ \underline{\sigma})$-dependent eigenvalues $\epsilon^j_{BO}(\underline{\underline{\mathbf{R}}}\ \underline{\sigma})$ and eigenfunctions $\phi^j_{\underline{\underline{\mathbf{R}}}\ \underline{\sigma}}$. The total molecular wavefunction, $\Psi_{BO}(\underline{\underline{\mathbf{R}}}\ \underline{\sigma}, \underline{\mathbf{r}}\ \underline{\mathbf{s}})$, is then approximated as a product of the relevant electronic state, $\phi^j_{\underline{\underline{\mathbf{R}}}\ \underline{\sigma}}(\underline{\mathbf{r}}\ \underline{\mathbf{s}})$, and a nuclear wavefunction $\chi^{BO}_{j\nu}(\underline{\underline{\mathbf{R}}}\ \underline{\sigma})$ satisfying the corresponding BO nuclear Schrödinger equation

$$\left(\sum_{\alpha=1}^{N_n}\frac{1}{2M_\alpha}(-i\nabla_\alpha + \mathcal{F}^{BO}_{jj,\alpha}(\underline{\underline{\mathbf{R}}}\ \underline{\sigma}))^2 + \epsilon^j_{GBO}(\underline{\underline{\mathbf{R}}}\ \underline{\sigma})\right)\chi^{BO}_{j\nu}(\underline{\underline{\mathbf{R}}}\ \underline{\sigma}) = E\chi^{BO}_{j\nu}(\underline{\underline{\mathbf{R}}}\ \underline{\sigma}) \tag{2.13}$$

where

$$\epsilon^j_{GBO}(\underline{\underline{\mathbf{R}}}\ \underline{\underline{\sigma}}) = \epsilon^j_{BO}(\underline{\underline{\mathbf{R}}}\ \underline{\underline{\sigma}}) + \sum_{\underline{\underline{\mathbf{s}}}} \left\langle \phi^j_{\underline{\underline{\mathbf{R}}}\ \underline{\underline{\sigma}}} \right| \sum_\alpha \frac{(-i\nabla_\alpha - \mathcal{F}^{BO}_{jj,\alpha})^2}{2M_\alpha} \left| \phi^j_{\underline{\underline{\mathbf{R}}}\ \underline{\underline{\sigma}}} \right\rangle_{\underline{\underline{\mathbf{r}}}} \tag{2.14}$$

and

$$\mathcal{F}^{BO}_{jj,\alpha}(\underline{\underline{\mathbf{R}}}\ \underline{\underline{\sigma}}) = -i \sum_{\underline{\underline{\mathbf{s}}}} \langle \phi^j_{\underline{\underline{\mathbf{R}}}\ \underline{\underline{\sigma}}} | \nabla_\alpha \phi^j_{\underline{\underline{\mathbf{R}}}\ \underline{\underline{\sigma}}} \rangle_{\underline{\underline{\mathbf{r}}}}\ , \tag{2.15}$$

where $\langle ..|..|.. \rangle_{\underline{\underline{\mathbf{r}}}}$ denotes an inner product over all spatial electronic variables only. The index ν of the nuclear wave function labels the vibrational/rotational eigenstate on the jth PES. The PES, ϵ^j_{GBO}, defined by (2.14) is called the *generalized BOPES* (GBOPES). The second term on the right of Eq. (2.14) is often referred to as the "BO diagonal correction" or "adiabatic correction". However, what is commonly referred to as the BOPES is $\epsilon^j_{BO}(\underline{\underline{\mathbf{R}}}\ \underline{\underline{\sigma}})$. The potential energy surface $\epsilon^j_{BO}(\underline{\underline{\mathbf{R}}}\ \underline{\underline{\sigma}})$ is enormously important in molecular physics and quantum chemistry. It is a central tool in the analysis and interpretation of molecular absorption and emission spectra, experiments involving nuclear motion, mechanisms of dissociation, energy-transfer, for example. The nuclear dynamics on a *single* PES (sometimes called "BO dynamics") is obtained by using the Hamiltonian on the left of Eq. (2.13) in a time-dependent Schrödinger equation for a time-dependent nuclear wavefunction $\chi(\underline{\underline{\mathbf{R}}}\ \underline{\underline{\sigma}}, t)$. This corresponds to approximating the total molecular wavefunction by a time-dependent nuclear wavepacket multiplied with a static electronic BO state:

$$\Psi(\underline{\underline{\mathbf{r}}}\ \underline{\underline{\mathbf{s}}}, \underline{\underline{\mathbf{R}}}\ \underline{\underline{\sigma}}, t) \approx \chi^{BO}(\underline{\underline{\mathbf{R}}}\ \underline{\underline{\sigma}}, t) \phi^j_{\underline{\underline{\mathbf{R}}}\ \underline{\underline{\sigma}}}(\underline{\underline{\mathbf{r}}}\ \underline{\underline{\mathbf{s}}}). \tag{2.16}$$

The vector potential $\mathcal{F}^{BO}_{jj,\alpha}(\underline{\underline{\mathbf{R}}}\ \underline{\underline{\sigma}})$, especially the Berry phase associated with it, $\oint d\underline{\underline{\mathbf{R}}} \cdot \mathcal{F}^{BO}_{jj,\alpha}(\underline{\underline{\mathbf{R}}}\ \underline{\underline{\sigma}})$, captures the essential features of the behavior of a system with conical intersections. Inclusion of $\mathcal{F}^{BO}_{jj,\alpha}(\underline{\underline{\mathbf{R}}}\ \underline{\underline{\sigma}})$ can significantly shift and re-order the energy eigenvalues of molecular roto-vibrational spectra, as well as scattering cross-sections (although sometimes undetected in experiments that measure integrated quantities, due to cancellations between paths, see e.g. Refs. [25–29] and references within).

It appears from the above discussion that in the traditional treatment of molecules and solids the concepts of the PES and the Berry phase arise as a consequence of the BO approximation. Some of the most fascinating phenomena of condensed-matter physics, like superconductivity, however, appear in the regime where the BO approximation is not valid; likewise typical photodynamical processes in molecules require going beyond

the single-electronic-surface picture. This raises the question: If one were to solve the Schrödinger equation of the full electron-nuclear Hamiltonian exactly (i.e. beyond the BO approximation) do the Berry phase and the potential energy surface survive, with a possibly modified form, and if so, how and where do they show up? What is their relation to the traditional potential energy surface and Berry phase in the BO approximation? Moreover, many interesting phenomena occur when molecules or solids are exposed to time-dependent external field e.g. lasers. Can one give a precise meaning to a *time-dependent* potential energy surface and a time-dependent vector potential?

Before answering the points raised above, focussing on the time-dependent case, we briefly discuss the BO *expansion* which solves the full TDSE Eq. (2.11) exactly for the coupled electron-nuclear system.

2.1.2 The Born-Oppenheimer Expansion

The set of electronic eigenfunctions $\{\phi^j_{\underline{\underline{\mathbf{R}}}\,\underline{\sigma}}(\underline{\mathbf{r}}\,\underline{\mathbf{s}})\}$ calculated from Eq. (2.12) form a complete orthonormal set in the electronic space for each fixed $\underline{\underline{\mathbf{R}}}\,\underline{\sigma}$

$$\sum_{\underline{\mathbf{s}}} \int d\underline{\mathbf{r}} \phi^{l*}_{\underline{\underline{\mathbf{R}}}\,\underline{\sigma}}(\underline{\mathbf{r}}\,\underline{\mathbf{s}}) \phi^{j}_{\underline{\underline{\mathbf{R}}}\,\underline{\sigma}}(\underline{\mathbf{r}}\,\underline{\mathbf{s}}) = \delta_{lj}, \tag{2.17}$$

therefore the total time-dependent wavefunction of the system $\Psi(\underline{\mathbf{r}}\,\underline{\mathbf{s}}, \underline{\underline{\mathbf{R}}}\,\underline{\sigma}, t)$ can be expanded in that basis:

$$\Psi(\underline{\mathbf{r}}\,\underline{\mathbf{s}}, \underline{\underline{\mathbf{R}}}\,\underline{\sigma}, t) = \sum_{j=1}^{\infty} F_j(\underline{\underline{\mathbf{R}}}\,\underline{\sigma}, t) \phi^{j}_{\underline{\underline{\mathbf{R}}}\,\underline{\sigma}}(\underline{\mathbf{r}}\,\underline{\mathbf{s}}) \,. \tag{2.18}$$

Here

$$F_j(\underline{\underline{\mathbf{R}}}\,\underline{\sigma}, t) = \sum_{\underline{\mathbf{s}}} \int d\underline{\mathbf{r}} \phi^{j*}_{\underline{\underline{\mathbf{R}}}\,\underline{\sigma}}(\underline{\mathbf{r}}\,\underline{\mathbf{s}}) \Psi(\underline{\mathbf{r}}\,\underline{\mathbf{s}}, \underline{\underline{\mathbf{R}}}\,\underline{\sigma}, t) \tag{2.19}$$

are the expansion coefficients which are functions of the nuclear degrees of freedom and time. Eq. (2.18) is the so-called BO expansion which is an *exact* representation of the complete molecular wavefunction due to the completeness of $\{\phi^j_{\underline{\underline{\mathbf{R}}}\,\underline{\sigma}}(\underline{\mathbf{r}}\,\underline{\mathbf{s}})\}$. It applies also to fully-time-dependent problems where Ψ evolves under external time-dependent potentials $\hat{V}^e_{\text{ext}}$. In practice, for numerically feasible calculations, approximations are introduced to limit the expansion to a small subset of $\{\phi^j_{\underline{\underline{\mathbf{R}}}\,\underline{\sigma}}(\underline{\mathbf{r}}\,\underline{\mathbf{s}})\}$. By inserting the expansion (2.18) into Eq. (2.11), multiplying by $\phi^{j*}_{\underline{\underline{\mathbf{R}}}\,\underline{\sigma}}(\underline{\mathbf{r}}\,\underline{\mathbf{s}})$ from the left, and integrating over the electronic degrees of freedom, equations for the expansion coefficients $F_j(\underline{\underline{\mathbf{R}}}\,\underline{\sigma}, t)$

are determined. One obtains:

$$\Big[\sum_{\alpha}\frac{1}{2M_\alpha}(-i\nabla_\alpha \quad + \quad \mathcal{F}^{BO}_{kk,\alpha})^2 + \hat{V}^{ext}_n(t) + \epsilon^k_{GBO}(\underline{\underline{\mathbf{R}}}\,\underline{\underline{\sigma}},t)\Big]\chi^{BO}_k + \sum_{j\neq k}\Big[< \phi^k|\hat{V}^{ext}_e(t)|\phi^j > -\sum_{\alpha}\Lambda^{BO}_{kj,\alpha}\Big]F_j = i\frac{\partial\chi^{BO}_k}{\partial t}\ . \quad (2.20)$$

Here

$$\epsilon^k_{GBO}(\underline{\underline{\mathbf{R}}}\,\underline{\underline{\sigma}},t) = \sum_{\underline{\underline{\sigma}}}\Big\langle \phi^k_{\underline{\underline{\mathbf{R}}}\,\underline{\underline{\sigma}}}\Big|\ \hat{H}_{BO} + \hat{V}^{ext}_e(t) + \sum_{\alpha}\frac{(-i\nabla_\alpha - \mathcal{F}^{BO}_{kk,\alpha})^2}{2M_\alpha}\ \Big|\phi^k_{\underline{\underline{\mathbf{R}}}\,\underline{\underline{\sigma}}}\Big\rangle_{\underline{\mathbf{r}}} \quad (2.21)$$

is the time-dependent scalar potential and is the kth generalized BO potential energy, generalized to account for the time-dependent external field (c.f. Eq. (2.14)). The terms

$$\Lambda^{BO}_{kj,\alpha}(\underline{\underline{\mathbf{R}}}) = \frac{1}{2M_\alpha}\Big[\mathcal{G}^{BO}_{kj,\alpha}(\underline{\underline{\mathbf{R}}}) + 2\mathcal{F}^{BO}_{kj,\alpha}(\underline{\underline{\mathbf{R}}})\cdot(i\nabla_\alpha)\Big] \quad (2.22)$$

are called the "nonadiabatic couplings", defined by [30–32]:

$$\begin{aligned}\mathcal{F}^{BO}_{kj,\alpha}(\underline{\underline{\mathbf{R}}}) &= -i < \phi^k_{\underline{\underline{\mathbf{R}}}\,\underline{\underline{\sigma}}}|\nabla_\alpha\phi^j_{\underline{\underline{\mathbf{R}}}\,\underline{\underline{\sigma}}} > \\ \mathcal{G}^{BO}_{kj,\alpha}(\underline{\underline{\mathbf{R}}}) &= < \phi^k_{\underline{\underline{\mathbf{R}}}\,\underline{\underline{\sigma}}}|\nabla^2_\alpha\phi^j_{\underline{\underline{\mathbf{R}}}\,\underline{\underline{\sigma}}} > .\end{aligned} \quad (2.23)$$

2.2 Exact factorization of the time-dependent electron-nuclear wavefunction

The BO expansion Eq. (2.18) yields the complete molecular wavefunction exactly. Instead of having an infinite sum of terms involving an infinite set of generalized PES's and non-adiabatic couplings, the question arises whether it is possible to represent the complete, time-dependent, electron-nuclear wavefunction exactly as a *single* product of an electronic wavefunction and a nuclear wavefunction. In this section, we show that the answer is yes. We derive formally exact equations of motion for each subsystem, out of which emerge rigorous definitions of a time-dependent potential energy surface and a time-dependent vector potential.

The decomposition is similar in form to the single-surface BO approximation, yet it is exact. There is no assumption on the time scale of the motions of each subsystem, i.e. unlike in the BO approximation, we do not solve for the "fast" variables first and then feed it into the equation for the "slower" variables. Instead, the equations of

motion for each subsystem are derived together, in a variational approach. The exact decomposition, contrary to the BO separation, accounts for the full correlation between the two subsystems, regardless of the mass and energy of the nuclear subsystem. In the following we formalize the idea as a theorem which we then prove. We discuss in detail the implications of this exact decomposition.

2.2.1 The exact factorization

Theorem I. (a) *The exact solution of Eq. (2.11) can be written as a single product*

$$\Psi(\underline{\underline{\mathbf{r}}}\ \underline{\underline{\mathbf{s}}}, \underline{\underline{\mathbf{R}}}\ \underline{\underline{\sigma}}, t) = \Phi_{\underline{\underline{\mathbf{R}}}\ \underline{\underline{\sigma}}}(\underline{\underline{\mathbf{r}}}\ \underline{\underline{\mathbf{s}}}, t)\chi(\underline{\underline{\mathbf{R}}}\ \underline{\underline{\sigma}}, t) \tag{2.24}$$

where $\Phi_{\underline{\underline{\mathbf{R}}}\ \underline{\underline{\sigma}}}(\underline{\underline{\mathbf{r}}}\ \underline{\underline{\mathbf{s}}}, t)$ *satisfies the Partial Normalization Condition (PNC),*

$$\sum_{\underline{\underline{\mathbf{s}}}} \int d\underline{\underline{\mathbf{r}}} |\Phi_{\underline{\underline{\mathbf{R}}}\ \underline{\underline{\sigma}}}(\underline{\underline{\mathbf{r}}}\ \underline{\underline{\mathbf{s}}}, t)|^2 = 1 \ , \tag{2.25}$$

for any fixed nuclear configuration, $\underline{\underline{\mathbf{R}}}\ \underline{\underline{\sigma}}$*, at any time* t*.*

The PNC is crucial in making this theorem meaningful: Eq. (2.24) on its own would be rather meaningless, because, for example, one could then simply just take $\chi(\underline{\underline{\mathbf{R}}}\ \underline{\underline{\sigma}}, t) \equiv 1$. In fact, one can come up with many different decompositions that satisfy Eq. (2.24) but that violate the PNC Eq. (2.25); it is the latter that makes the decomposition unique up to within a gauge-like transformation, as we shall see shortly in Section 2.2.2. We will also see there that it is the PNC that allows the interpretation of $\Phi_{\underline{\underline{\mathbf{R}}}\ \underline{\underline{\sigma}}}(\underline{\underline{\mathbf{r}}}\ \underline{\underline{\mathbf{s}}}, t)$ as a conditional probability amplitude, and $\chi(\underline{\underline{\mathbf{R}}}\ \underline{\underline{\sigma}}, t)$ as a marginal probability amplitude, leading to their identification as electronic and nuclear wavefunctions respectively. First, we prove Part(a) of Theorem I.

Proof: Given $\Psi(\underline{\underline{\mathbf{r}}}\ \underline{\underline{\mathbf{s}}}, \underline{\underline{\mathbf{R}}}\ \underline{\underline{\sigma}}, t)$, the exact solution of the full TDSE (2.11). We choose $\chi(\underline{\underline{\mathbf{R}}}\ \underline{\underline{\sigma}}, t)$ and $\Phi_{\underline{\underline{\mathbf{R}}}\ \underline{\underline{\sigma}}}(\underline{\underline{\mathbf{r}}}\ \underline{\underline{\mathbf{s}}}, t)$, at any instant in time, as

$$\chi(\underline{\underline{\mathbf{R}}}\ \underline{\underline{\sigma}}, t) = e^{iS(\underline{\underline{\mathbf{R}}}\ \underline{\underline{\sigma}}, t)} \sqrt{\sum_{\underline{\underline{\mathbf{s}}}} \int d\underline{\underline{\mathbf{r}}} |\Psi(\underline{\underline{\mathbf{r}}}\ \underline{\underline{\mathbf{s}}}, \underline{\underline{\mathbf{R}}}\ \underline{\underline{\sigma}}, t)|^2} \, , \tag{2.26}$$

and,

$$\Phi_{\underline{\underline{\mathbf{R}}}\ \underline{\underline{\sigma}}}(\underline{\underline{\mathbf{r}}}\ \underline{\underline{\mathbf{s}}}, t) = \Psi(\underline{\underline{\mathbf{r}}}\ \underline{\underline{\mathbf{s}}}, \underline{\underline{\mathbf{R}}}\ \underline{\underline{\sigma}}, t) / \chi(\underline{\underline{\mathbf{R}}}\ \underline{\underline{\sigma}}, t) \tag{2.27}$$

where $S(\underline{\underline{\mathbf{R}}}\ \underline{\underline{\sigma}}, t)$ is real. The PNC Eq. (2.25) then follows immediately:

$$\sum_{\underline{\underline{\mathbf{s}}}} \int d\underline{\underline{\mathbf{r}}} |\Phi_{\underline{\underline{\mathbf{R}}}\ \underline{\underline{\sigma}}}(\underline{\underline{\mathbf{r}}}\ \underline{\underline{\mathbf{s}}}, t)|^2 = \frac{\sum_{\underline{\underline{\mathbf{s}}}} \int d\underline{\underline{\mathbf{r}}} |\Psi(\underline{\underline{\mathbf{r}}}\ \underline{\underline{\mathbf{s}}}, \underline{\underline{\mathbf{R}}}\ \underline{\underline{\sigma}}, t)|^2}{|\chi(\underline{\underline{\mathbf{R}}}\ \underline{\underline{\sigma}}, t)|^2} = \frac{|\chi(\underline{\underline{\mathbf{R}}}\ \underline{\underline{\sigma}}, t)|^2}{|\chi(\underline{\underline{\mathbf{R}}}\ \underline{\underline{\sigma}}, t)|^2} = 1. \tag{2.28}$$

This concludes the proof of Theorem I (a). It will become clear throughout this paper that, in many respects, the nuclear factor $\chi(\underline{\underline{\mathbf{R}}}\ \underline{\underline{\sigma}}, t)$ can be viewed as a proper nuclear wavefunction. Like in the static case [33, 34], introducing the phase factor in Eq. (2.27) allows $\chi(\underline{\underline{\mathbf{R}}}\ \underline{\underline{\sigma}}, t)$ to have the correct symmetry or antisymmetry if the nuclear subsystem contains identical nuclei.

Next comes the question; what equations do $\Phi_{\underline{\underline{\mathbf{R}}}\ \underline{\underline{\sigma}}}(\underline{\underline{\mathbf{r}}}\ \underline{\underline{\mathbf{s}}}, t)$ and $\chi(\underline{\underline{\mathbf{R}}}\ \underline{\underline{\sigma}}, t)$ satisfy? The answer entails the second part of Theorem I:

Theorem I (b) *The wavefunctions* $\Phi_{\underline{\underline{\mathbf{R}}}\ \underline{\underline{\sigma}}}(\underline{\underline{\mathbf{r}}}\ \underline{\underline{\mathbf{s}}}, t)$ *and* $\chi(\underline{\underline{\mathbf{R}}}\ \underline{\underline{\sigma}}, t)$ *satisfy:*

$$\Big(\hat{H}_{el}(\underline{\underline{\mathbf{r}}}\ \underline{\underline{\mathbf{s}}}, \underline{\underline{\mathbf{R}}}\ \underline{\underline{\sigma}}, t) - \epsilon(\underline{\underline{\mathbf{R}}}\ \underline{\underline{\sigma}}, t)\Big)\Phi_{\underline{\underline{\mathbf{R}}}\ \underline{\underline{\sigma}}}(\underline{\underline{\mathbf{r}}}\ \underline{\underline{\mathbf{s}}}, t) = i\partial_t \Phi_{\underline{\underline{\mathbf{R}}}\ \underline{\underline{\sigma}}}(\underline{\underline{\mathbf{r}}}\ \underline{\underline{\mathbf{s}}}, t), \tag{2.29}$$

$$\Big(\sum_{\alpha=1}^{N_n} \frac{1}{2M_\alpha}(-i\nabla_\alpha + \mathbf{A}_\alpha(\underline{\underline{\mathbf{R}}}\ \underline{\underline{\sigma}}, t))^2 + \hat{V}_n^{ext}(\underline{\underline{\mathbf{R}}}, t) + \epsilon(\underline{\underline{\mathbf{R}}}\ \underline{\underline{\sigma}}, t)\Big)\chi(\underline{\underline{\mathbf{R}}}\ \underline{\underline{\sigma}}, t) = i\partial_t \chi(\underline{\underline{\mathbf{R}}}\ \underline{\underline{\sigma}}, t), \tag{2.30}$$

where the electronic Hamiltonian is

$$\hat{H}_{el}(\underline{\underline{\mathbf{r}}}\ \underline{\underline{\mathbf{s}}}, \underline{\underline{\mathbf{R}}}\ \underline{\underline{\sigma}}, t) = \hat{H}_{BO}(\underline{\underline{\mathbf{r}}}, \underline{\underline{\mathbf{R}}}, t) + \hat{V}_e^{ext}(\underline{\underline{\mathbf{r}}}, t) + \hat{U}_{en}^{coup}\left[\Phi_{\underline{\underline{\mathbf{R}}}\ \underline{\underline{\sigma}}}, \chi\right]. \tag{2.31}$$

Here the electron-nuclear coupling potential $\hat{U}_{en}^{coup}\left[\Phi_{\underline{\underline{\mathbf{R}}}\ \underline{\underline{\sigma}}}, \chi\right]$, *scalar potential* $\epsilon(\underline{\underline{\mathbf{R}}}\ \underline{\underline{\sigma}}, t)$, *and vector potential* $\mathbf{A}_\alpha(\underline{\underline{\mathbf{R}}}\ \underline{\underline{\sigma}}, t)$ *terms are*

$$\hat{U}_{en}^{coup}\left[\Phi_{\underline{\underline{\mathbf{R}}}\ \underline{\underline{\sigma}}}, \chi\right] = \sum_{\alpha=1}^{N_n} \frac{1}{M_\alpha}\Big[\frac{(-i\nabla_\alpha - \mathbf{A}_\alpha(\underline{\underline{\mathbf{R}}}\ \underline{\underline{\sigma}}, t))^2}{2} + \Big(\frac{-i\nabla_\alpha \chi}{\chi} + \mathbf{A}_\alpha(\underline{\underline{\mathbf{R}}}\ \underline{\underline{\sigma}}, t)\Big) \cdot \big(-i\nabla_\alpha - \mathbf{A}_\alpha(\underline{\underline{\mathbf{R}}}\ \underline{\underline{\sigma}}, t)\big)\Big] \tag{2.32}$$

$$\epsilon(\underline{\underline{\mathbf{R}}}\ \underline{\underline{\sigma}}, t) = \sum_{\underline{\underline{\mathbf{s}}}} \Big\langle \Phi_{\underline{\underline{\mathbf{R}}}\ \underline{\underline{\sigma}}}(t) \Big| \hat{H}_{el}((\underline{\underline{\mathbf{r}}}\ \underline{\underline{\mathbf{s}}}, \underline{\underline{\mathbf{R}}}\ \underline{\underline{\sigma}}, t) - i\partial_t \Big| \Phi_{\underline{\underline{\mathbf{R}}}\ \underline{\underline{\sigma}}}(t) \Big\rangle_{\underline{\underline{\mathbf{r}}}} \tag{2.33}$$

$$\mathbf{A}_\alpha(\underline{\underline{\mathbf{R}}}\ \underline{\underline{\sigma}}, t) = \sum_{\underline{\underline{\mathbf{s}}}} \Big\langle \Phi_{\underline{\underline{\mathbf{R}}}\ \underline{\underline{\sigma}}}(t) \Big| -i\nabla_\alpha \Phi_{\underline{\underline{\mathbf{R}}}\ \underline{\underline{\sigma}}}(t) \Big\rangle_{\underline{\underline{\mathbf{r}}}} \tag{2.34}$$

$$\tag{2.35}$$

where $\langle ..|..|.. \rangle_{\underline{\underline{\mathbf{r}}}}$ *denotes an inner product over all spatial electronic variables only.*

Proof: In order to derive the equations of motion for $\Phi_{\underline{\underline{\mathbf{R}}}\,\underline{\underline{\sigma}}}(\underline{\underline{\mathbf{r}}}\,\underline{\underline{\mathbf{s}}}, t)$ and $\chi(\underline{\underline{\mathbf{R}}}\,\underline{\underline{\sigma}}, t)$ we follow the strategy employed in the static case (see ref. [33, 34]), i.e. we plug the product ansatz in the variational principle and search for the stationary point. Afterwards we prove: if $\Phi_{\underline{\underline{\mathbf{R}}}\,\underline{\underline{\sigma}}}(\underline{\underline{\mathbf{r}}}\,\underline{\underline{\mathbf{s}}}, t)$ and $\chi(\underline{\underline{\mathbf{R}}}\,\underline{\underline{\sigma}}, t)$ are the solutions of Eqs. (2.29) and (2.30), then $\Phi_{\underline{\underline{\mathbf{R}}}\,\underline{\underline{\sigma}}}(\underline{\underline{\mathbf{r}}}\,\underline{\underline{\mathbf{s}}}, t)\chi(\underline{\underline{\mathbf{R}}}\,\underline{\underline{\sigma}}, t)$ is the solution of TDSE (2.11). We begin the derivation by briefly reviewing Frenkel's stationary action principle as this is the key instrument to derive the equations of motion for each subsystem.

The quantum mechanical action is defined as

$$\mathcal{S}[\Psi, \Psi^*] = \int_{t_i}^{t_f} dt \langle \Psi | \hat{H} - i\partial_t | \Psi \rangle, \tag{2.36}$$

a functional of the time-dependent wavefunction $\Psi(t)$ and its complex conjugate. The equation of motion of the quantum system, the TDSE of Eq. (2.11), is obtained by requiring the variation of the action $\mathcal{S}$ with respect to all wavefunctions $\Psi(t)$ that satisfy the boundary condition

$$\delta\Psi(t_i) = \delta\Psi(t_f) = 0\ , \tag{2.37}$$

to be stationary, i.e.,

$$\delta_{\Psi^*}\mathcal{S} = 0. \tag{2.38}$$

Now we apply this general variational principle to our problem in the following way. We insert the product wavefunction in the action functional (2.36), with Hamiltonian given by Eq. (2.2), rewriting it as

$$\begin{aligned}
\mathcal{S}[\Phi_{\underline{\underline{\mathbf{R}}}\,\underline{\underline{\sigma}}}, \Phi^*_{\underline{\underline{\mathbf{R}}}\,\underline{\underline{\sigma}}}, \chi, \chi^*] \;=\; & \sum_{\underline{\underline{\mathbf{s}}},\underline{\underline{\sigma}}} \int_{t_i}^{t_f} dt \int d\underline{\underline{\mathbf{R}}} \int d\underline{\underline{\mathbf{r}}} \\
& \Big[|\chi|^2 \Phi^*_{\underline{\underline{\mathbf{R}}}\,\underline{\underline{\sigma}}} \left(H_{BO} + V_e^{ext} + \sum_\alpha \frac{-\nabla_\alpha^2}{2M_\alpha} - i\partial_t \right) \Phi_{\underline{\underline{\mathbf{R}}}\,\underline{\underline{\sigma}}} + \\
& |\Phi_{\underline{\underline{\mathbf{R}}}\,\underline{\underline{\sigma}}}|^2 \chi^* \left(\sum_\alpha \frac{-\nabla_\alpha^2}{2M_\alpha} + V_n^{ext} - i\partial_t \right) \chi + \\
& |\chi|^2 \Phi^*_{\underline{\underline{\mathbf{R}}}\,\underline{\underline{\sigma}}} \sum_\alpha \frac{1}{M_\alpha} (-i\nabla_\alpha \chi/\chi) \cdot (-i\nabla_\alpha \Phi_{\underline{\underline{\mathbf{R}}}\,\underline{\underline{\sigma}}}) \Big] \ .
\end{aligned} \tag{2.39}$$

The equations of motion for $\Phi_{\underline{\underline{\mathbf{R}}}\,\underline{\underline{\sigma}}}(\underline{\underline{\mathbf{r}}}\,\underline{\underline{\mathbf{s}}}, t)$ and $\chi(\underline{\underline{\mathbf{R}}}\,\underline{\underline{\sigma}}, t)$ are obtained by requiring the action functional (2.39) to be stationary with respect to variations of each wavefunction

subject to the PNC (2.25), i.e.,

$$\frac{\delta\mathcal{S}[\Phi_{\underline{\underline{\mathbf{R}}}\,\underline{\sigma}},\Phi^*_{\underline{\underline{\mathbf{R}}}\,\underline{\sigma}},\chi,\chi^*]}{\delta\Phi^*_{\underline{\underline{\mathbf{R}}}\,\underline{\sigma}}(\underline{\mathbf{r}}\,\underline{\mathbf{s}},t)}=0 \quad \text{and} \quad \frac{\delta\mathcal{S}[\Phi_{\underline{\underline{\mathbf{R}}}\,\underline{\sigma}},\Phi^*_{\underline{\underline{\mathbf{R}}}\,\underline{\sigma}},\chi,\chi^*]}{\delta\chi^*(\underline{\underline{\mathbf{R}}}\,\underline{\sigma},t)}=0 \tag{2.40}$$

Variation of Eq. (2.39) with respect to $\Phi^*_{\underline{\underline{\mathbf{R}}}\,\underline{\sigma}}(\underline{\mathbf{r}}\,\underline{\mathbf{s}})$ leads to

$$|\chi|^2\left(\hat{H}_{BO}+\hat{V}^e_{ext}+\sum_\alpha\frac{-\nabla^2_\alpha}{2M_\alpha}-i\partial_t\right)\Phi_{\underline{\underline{\mathbf{R}}}\,\underline{\sigma}}+\left[\chi^*\left(\sum_\alpha\frac{-\nabla^2_\alpha}{2M_\alpha}+\hat{V}^n_{ext}-i\partial_t\right)\chi\right]\Phi_{\underline{\underline{\mathbf{R}}}\,\underline{\sigma}}$$
$$+|\chi|^2\left(\sum_\alpha\frac{1}{M_\alpha}(-i\nabla_\alpha\chi/\chi)\cdot(-i\nabla_\alpha\Phi_{\underline{\underline{\mathbf{R}}}\,\underline{\sigma}})\right)=0$$

Dividing the expression above by $|\chi|^2$ and rearranging yields:

$$\Big(\hat{H}_{BO}\;+\;\hat{V}^e_{ext}+\sum_\alpha\frac{-\nabla^2_\alpha}{2M_\alpha}-i\partial_t\Big)\Phi_{\underline{\underline{\mathbf{R}}}\,\underline{\sigma}}+$$
$$\sum_\alpha\frac{1}{M_\alpha}(-i\nabla_\alpha\chi/\chi)\cdot(-i\nabla_\alpha\Phi_{\underline{\underline{\mathbf{R}}}\,\underline{\sigma}})=-\frac{(\sum_\alpha\frac{-\nabla^2_\alpha}{2M_\alpha}+\hat{V}^n_{ext}-i\partial_t)\chi}{\chi}\cdot\Phi_{\underline{\underline{\mathbf{R}}}\,\underline{\sigma}}\,. \tag{2.41}$$

Variation of Eq. (2.39) with respect to χ^* yields

$$\Big[\sum_{\underline{\mathbf{s}}}\int d\underline{\underline{\mathbf{r}}}\Phi^*_{\underline{\underline{\mathbf{R}}}\,\underline{\sigma}}\Big(H_{BO}+\hat{V}^e_{ext}\;+\;\sum_\alpha\frac{-\nabla^2_\alpha}{2M_\alpha}-i\partial_t\Big)\Phi_{\underline{\underline{\mathbf{R}}}\,\underline{\sigma}}\Big]\chi+$$
$$\left[\sum_\alpha\frac{-\nabla^2_\alpha}{2M_\alpha}+\hat{V}^n_{ext}\right]\chi+$$
$$\left[\sum_\alpha\frac{1}{M_\alpha}(-i\nabla_\alpha\chi/\chi)\cdot\mathbf{A}_\alpha\right]\chi=i\partial_t\chi \tag{2.42}$$

where we enforced the PNC, and defined

$$\mathbf{A}_\alpha[\Phi_{\underline{\underline{\mathbf{R}}}\,\underline{\sigma}}]:=\sum_{\underline{\mathbf{s}}}\int d\underline{\underline{\mathbf{r}}}\Phi^*_{\underline{\underline{\mathbf{R}}}\,\underline{\sigma}}(\underline{\mathbf{r}}\,\underline{\mathbf{s}})(-i\nabla_\alpha\Phi_{\underline{\underline{\mathbf{R}}}\,\underline{\sigma}}(\underline{\mathbf{r}}\,\underline{\mathbf{s}}))\,. \tag{2.43}$$

This is a real-valued vector potential (see shortly). Inserting Eq. (2.42) on the RHS of Eq. (2.41) leads, after some straightforward algebra, to Eqs. (2.29-2.34). The product wavefunction Eq. (2.24), satisfying these equations, therefore represents a stationary point of the action functional (2.39) under the PNC Eq. (2.25). To complete the proof, it remains to verify that if $\Phi_{\underline{\underline{\mathbf{R}}}\,\underline{\sigma}}(\underline{\mathbf{r}}\,\underline{\sigma},t)$ satisfies Eq. (2.29) and $\chi(\underline{\underline{\mathbf{R}}}\,\underline{\sigma},t)$ satisfies Eq. (2.30), then the product $\Phi_{\underline{\underline{\mathbf{R}}}\,\underline{\sigma}}(\underline{\mathbf{r}}\,\underline{\mathbf{s}},t)\chi(\underline{\underline{\mathbf{R}}}\,\underline{\sigma},t)$ is an exact solution of the TDSE. Approximate

solutions of the TDSE may satisfy the stationary action principle, if variations are taken over a limited set of wavefunctions, e.g. the multi-configuration time-dependent Hartree equations [35] may be derived via the Frenkel variational principle. To dispel any possible doubts that the product form of Eq. (2.24) subject to Eq. (2.25) is general, we now verify that our solution is exact and not an approximation. Applying the product rule, $i\partial_t \Psi(\underline{\underline{\mathbf{r}}}\ \underline{\underline{\mathbf{s}}}, \underline{\underline{\mathbf{R}}}\ \underline{\underline{\sigma}}, t) = \chi(\underline{\underline{\mathbf{R}}}\ \underline{\underline{\sigma}}, t) i\partial_t \Phi_{\underline{\underline{\mathbf{R}}}\ \underline{\underline{\sigma}}}(\underline{\underline{\mathbf{r}}}\ \underline{\underline{\mathbf{s}}}, t) + \Phi_{\underline{\underline{\mathbf{R}}}\ \underline{\underline{\sigma}}}(\underline{\underline{\mathbf{r}}}\ \underline{\underline{\mathbf{s}}}, t) i\partial_t \chi(\underline{\underline{\mathbf{R}}}\ \underline{\underline{\sigma}}, t)$, and inserting Eqs. (2.29) and (2.30), we obtain

$$\begin{aligned} \chi\left(i\partial_t \Phi_{\underline{\underline{\mathbf{R}}}\ \underline{\underline{\sigma}}}\right) &= \chi\left(\hat{H}_{BO} + V^e_{ext}\right)\Phi_{\underline{\underline{\mathbf{R}}}\ \underline{\underline{\sigma}}} + \chi \sum_{\alpha}^{N_n} \frac{(-i\nabla_\alpha - \mathbf{A}_\alpha)^2}{2M_\alpha} \Phi_{\underline{\underline{\mathbf{R}}}\ \underline{\underline{\sigma}}} \\ &\quad + \chi \sum_{\alpha}^{N_n} \frac{(-i\nabla_\alpha \chi/\chi + \mathbf{A}_\alpha) \cdot (-i\nabla_\alpha - \mathbf{A}_\alpha)}{M_\alpha} \Phi_{\underline{\underline{\mathbf{R}}}\ \underline{\underline{\sigma}}} - \chi\epsilon\Phi_{\underline{\underline{\mathbf{R}}}\ \underline{\underline{\sigma}}} \end{aligned} \tag{2.44}$$

$$\Phi_{\underline{\underline{\mathbf{R}}}\ \underline{\underline{\sigma}}}\left(i\partial_t \chi\right) = \Phi_{\underline{\underline{\mathbf{R}}}\ \underline{\underline{\sigma}}} \sum_{\alpha}^{N_n} \frac{(-i\nabla_\alpha + \mathbf{A}_\alpha(\underline{\underline{\mathbf{R}}}\ \underline{\underline{\sigma}}, t))^2}{2M_\alpha} \chi + \Phi_{\underline{\underline{\mathbf{R}}}\ \underline{\underline{\sigma}}} \hat{V}^{ext}_n \chi + \Phi_{\underline{\underline{\mathbf{R}}}\ \underline{\underline{\sigma}}} \epsilon\chi \tag{2.45}$$

Summing Eqs. (2.44) and (2.45) leads to the TDSE for the complete system (2.11) and completes the proof that the wavefunctions satisfying Eqs. (2.29-2.34) do solve the TDSE exactly.

Alternatively, Eqs. (2.29-2.34) can be obtained by replacing $\Psi(\underline{\underline{\mathbf{r}}}\ \underline{\underline{\mathbf{s}}}, \underline{\underline{\mathbf{R}}}\ \underline{\underline{\sigma}}, t)$, in the TDSE (2.11), by the product $\Phi_{\underline{\underline{\mathbf{R}}}\ \underline{\underline{\sigma}}}(\underline{\underline{\mathbf{r}}}\ \underline{\underline{\mathbf{s}}}, t)\chi(\underline{\underline{\mathbf{R}}}\ \underline{\underline{\sigma}}, t)$ and using the PNC (2.25). The form of electron-nuclear coupling term, Eq. (2.32), is the same as the static case (see ref. [33, 34]). The exact TDPES, Eq. (2.33), on the other hand is not simply the expectation value of $\hat{H}_{el}$ but contains, in addition, the term $< \Phi_{\underline{\underline{\mathbf{R}}}\ \underline{\underline{\sigma}}} | - i\partial_t \Phi_{\underline{\underline{\mathbf{R}}}\ \underline{\underline{\sigma}}} >$. The appearance of this term is essential to ensure the form invariance of the Eqs. (2.29-2.34) under the gauge transformation (2.46).

2.2.2 Uniqueness of the electronic and nuclear wavefunctions

We now delve a little deeper into features of our exact factorization. As briefly mentioned earlier, the factorization can be viewed in a standard probabilistic setting [1]: The square of the molecular wavefunction can be viewed as a multivariate probability distribution, that can be factorized into a marginal probability of a set of variables (the

nuclear coordinates) and a conditional probability of the rest of the variables (the electronic coordinates, conditionally dependent on the nuclear coordinates). In this sense we identify $\chi(\underline{\underline{\mathbf{R}}}\ \underline{\underline{\sigma}}, t)$ as the nuclear wavefunction (marginal probability amplitude), and $\Phi_{\underline{\underline{\mathbf{R}}}\ \underline{\underline{\sigma}}}(\underline{\mathbf{r}}\ \underline{\mathbf{s}}, t)$ as the electronic wavefunction (conditional probability amplitude). An alternative, equally valid formalism is to view, instead, the nuclear wavefunction as a conditional probability amplitude depending parametrically on the electronic coordinate, i.e. $\chi_{\underline{\mathbf{r}}\ \underline{\mathbf{s}}}(\underline{\underline{\mathbf{R}}}\ \underline{\underline{\sigma}}, t)$, with the electronic wavefunction as the marginal probability amplitude of the electronic coordinates, i.e. $\Phi(\underline{\mathbf{r}}\ \underline{\mathbf{s}}, t)$. We choose to use the former decomposition however to later make natural connections with the BO approach. In this section we argue why we can view the probability amplitudes $\chi(\underline{\underline{\mathbf{R}}}\ \underline{\underline{\sigma}}, t)$ and $\Phi_{\underline{\underline{\mathbf{R}}}\ \underline{\underline{\sigma}}}(\underline{\mathbf{r}}\ \underline{\mathbf{s}}, t)$ as nuclear and electronic wavefunctions, and we will assign some meaning to the terms that arise in their equations of motion.

A first question that arises is: is this decomposition unique? We answer this in Theorem 2.

Theorem 2 (a) *Eqs. (2.29-2.34) are form-invariant up to within the gauge-like transformation:*

$$\begin{aligned} \tilde{\Phi}_{\underline{\underline{\mathbf{R}}}\ \underline{\underline{\sigma}}}(\underline{\mathbf{r}}\ \underline{\mathbf{s}}, t) &:= e^{i\theta(\underline{\underline{\mathbf{R}}}\ \underline{\underline{\sigma}}, t)} \Phi_{\underline{\underline{\mathbf{R}}}\ \underline{\underline{\sigma}}}(\underline{\mathbf{r}}\ \underline{\mathbf{s}}, t) \\ \tilde{\chi}(\underline{\underline{\mathbf{R}}}\ \underline{\underline{\sigma}}, t) &:= e^{-i\theta(\underline{\underline{\mathbf{R}}}\ \underline{\underline{\sigma}}, t)} \chi(\underline{\underline{\mathbf{R}}}\ \underline{\underline{\sigma}}, t) \end{aligned} \tag{2.46}$$

$$\begin{aligned} &\mathbf{A}_\alpha(\underline{\underline{\mathbf{R}}}\ \underline{\underline{\sigma}}, t) \to \tilde{\mathbf{A}}_\alpha(\underline{\underline{\mathbf{R}}}\ \underline{\underline{\sigma}}, t) = \mathbf{A}_\alpha(\underline{\underline{\mathbf{R}}}\ \underline{\underline{\sigma}}, t) + \nabla_\alpha \theta(\underline{\underline{\mathbf{R}}}\ \underline{\underline{\sigma}}, t) \\ &\epsilon(\underline{\underline{\mathbf{R}}}\ \underline{\underline{\sigma}}, t) \to \tilde{\epsilon}(\underline{\underline{\mathbf{R}}}\ \underline{\underline{\sigma}}, t) = \epsilon(\underline{\underline{\mathbf{R}}}\ \underline{\underline{\sigma}}, t) + \partial_t \theta(\underline{\underline{\mathbf{R}}}\ \underline{\underline{\sigma}}, t) \end{aligned} \tag{2.47}$$

(b) *The wavefunctions $\Phi_{\underline{\underline{\mathbf{R}}}\ \underline{\underline{\sigma}}}(\underline{\mathbf{r}}\ \underline{\mathbf{s}}, t)$ and $\chi(\underline{\underline{\mathbf{R}}}\ \underline{\underline{\sigma}}, t)$ are unique up to within the $(\underline{\underline{\mathbf{R}}}\ \underline{\underline{\sigma}}, t)$-dependent phase transformation, Eq. (2.46).*

Proof: To prove part (a), simply substitute Eqs. (2.46) and (2.47) into Eqs (2.29)–(2.34). Part (b) is readily shown by first assuming that $\Phi_{\underline{\underline{\mathbf{R}}}\ \underline{\underline{\sigma}}}\chi$ and $\tilde{\Phi}_{\underline{\underline{\mathbf{R}}}\ \underline{\underline{\sigma}}}\tilde{\chi}$ are two different representations of the exact wave function $\Psi(\underline{\mathbf{r}}\ \underline{\mathbf{s}}, \underline{\underline{\mathbf{R}}}\ \underline{\underline{\sigma}}, t)$ i.e.

$$\Psi(\underline{\mathbf{r}}\ \underline{\mathbf{s}}, \underline{\underline{\mathbf{R}}}\ \underline{\underline{\sigma}}, t) = \Phi_{\underline{\underline{\mathbf{R}}}\ \underline{\underline{\sigma}}}(\underline{\mathbf{r}}\ \underline{\mathbf{s}}, t)\chi(\underline{\underline{\mathbf{R}}}\ \underline{\underline{\sigma}}, t) = \tilde{\Phi}_{\underline{\underline{\mathbf{R}}}\ \underline{\underline{\sigma}}}(\underline{\mathbf{r}}\ \underline{\mathbf{s}}, t)\tilde{\chi}(\underline{\underline{\mathbf{R}}}\ \underline{\underline{\sigma}}, t) \tag{2.48}$$

Then

$$\frac{\chi}{\tilde{\chi}} = \frac{\tilde{\Phi}_{\underline{\underline{\mathbf{R}}}\ \underline{\underline{\sigma}}}}{\Phi_{\underline{\underline{\mathbf{R}}}\ \underline{\underline{\sigma}}}} =: g(\underline{\underline{\mathbf{R}}}\ \underline{\underline{\sigma}}, t) \tag{2.49}$$

and

$$|\tilde{\Phi}_{\underline{\underline{\mathbf{R}}}\,\underline{\sigma}}(\underline{\mathbf{r}}\,\underline{\mathbf{s}},t)|^2 = |g(\underline{\underline{\mathbf{R}}}\,\underline{\sigma},t)|^2|\Phi_{\underline{\underline{\mathbf{R}}}\,\underline{\sigma}}(\underline{\mathbf{r}}\,\underline{\mathbf{s}},t)|^2. \tag{2.50}$$

From the theorem we know that both $\tilde{\Phi}_{\underline{\underline{\mathbf{R}}}\,\underline{\sigma}}(\underline{\mathbf{r}}\,\underline{\mathbf{s}},t)$ and $\Phi_{\underline{\underline{\mathbf{R}}}\,\underline{\sigma}}(\underline{\mathbf{r}}\,\underline{\mathbf{s}},t)$ satisfy the PNC. Hence,

$$\sum_{\underline{\mathbf{s}}}\int d\underline{\mathbf{r}}|\tilde{\Phi}_{\underline{\underline{\mathbf{R}}}\,\underline{\sigma}}(\underline{\mathbf{r}}\,\underline{\mathbf{s}},t)|^2 = |g(\underline{\underline{\mathbf{R}}}\,\underline{\sigma},t)|^2\sum_{\underline{\mathbf{s}}}\int d\underline{\mathbf{r}}|\Phi_{\underline{\underline{\mathbf{R}}}\,\underline{\sigma}}(\underline{\underline{\mathbf{R}}}\,\underline{\sigma},t)|^2 \tag{2.51}$$

and $|g(\underline{\underline{\mathbf{R}}}\,\underline{\sigma},t)|^2 = 1$. Therefore, $g(\underline{\underline{\mathbf{R}}}\,\underline{\sigma},t)$ must be equal to a purely $(\underline{\underline{\mathbf{R}}}\,\underline{\sigma},t)$-dependence phase:

$$g(\underline{\underline{\mathbf{R}}}\,\underline{\sigma},t) = e^{i\theta(\underline{\underline{\mathbf{R}}}\,\underline{\sigma},t)}. \tag{2.52}$$

This completes the proof of theorem 2.

The interpretation of $\Phi_{\underline{\underline{\mathbf{R}}}}$ and χ as electronic and nuclear wavefunctions follows from the following observations. The probability density of finding the nuclear configuration $\underline{\underline{\mathbf{R}}}$ at time t, $\sum_{\underline{\mathbf{s}}}\int|\Psi(\underline{\mathbf{r}}\,\underline{\mathbf{s}},\underline{\underline{\mathbf{R}}}\,\underline{\sigma},t)|^2d\underline{\mathbf{r}} = |\chi(\underline{\underline{\mathbf{R}}}\,\underline{\sigma},t)|^2$, as can readily be shown by substituting the product wavefunction Eq. (2.24) into the left-hand-side and using the PNC Eq. (2.25). Not only does $\chi(\underline{\underline{\mathbf{R}}}\,\underline{\sigma},t)$ therefore yield the nuclear (N_n-body) probability density, we shall see later in Section 2.3.1, that it also reproduces the exact nuclear (N_n-body) current-density. The modulus-square of the electronic wavefunction, $|\Phi_{\underline{\underline{\mathbf{R}}}\,\underline{\sigma}}(\underline{\mathbf{r}}\,\underline{\mathbf{s}},t)|^2 = |\Psi(\underline{\mathbf{r}}\,\underline{\mathbf{s}},\underline{\underline{\mathbf{R}}}\,\underline{\sigma},t)|^2/|\chi(\underline{\underline{\mathbf{R}}}\,\underline{\sigma},t)|^2$, on the other hand, gives the conditional probability of finding the electrons at $\underline{\mathbf{r}}$ with spin configuration $\underline{\mathbf{s}}$, given that the nuclear configuration is $\underline{\underline{\mathbf{R}}}\,\underline{\sigma}$.

Note that, strictly speaking, the definition of the conditional probability amplitude $|\Phi_{\underline{\underline{\mathbf{R}}}\,\underline{\sigma}}(\underline{\mathbf{r}}\,\underline{\mathbf{s}},t)|^2$ via Eq. (2.26), only holds for non-zero marginal probabilities $|\chi(\underline{\underline{\mathbf{R}}}\,\underline{\sigma},t)|^2$. In the case the nuclear density, and the full molecular wavefunction, have a node at some $\underline{\underline{\mathbf{R}}}_0$, the electronic wavefunction would be defined by taking a limit. However, it is actually very unlikely that the nuclear density has a node [36, 37]. This can be seen by expanding the full electron-nuclear wavefunction, $\Psi(\underline{\mathbf{r}}\,\underline{\mathbf{s}},\underline{\underline{\mathbf{R}}}\,\underline{\sigma},t)$, in terms of the BO-electronic states, as in Eq. (2.18). Then, the nuclear density can be expressed as an infinite sum of non-negative terms:

$$|\chi(\underline{\underline{\mathbf{R}}}\,\underline{\sigma},t)|^2 = \sum_{j=1}^{\infty}|F_j(\underline{\underline{\mathbf{R}}}\,\underline{\sigma},t)|^2\,. \tag{2.53}$$

In general, it is extremely unlikely that every term in the summation becomes zero at the same nuclear configuration $\underline{\underline{\mathbf{R}}}_0\,\underline{\sigma}_0$, unless dictated by symmetry [33, 34] (see end of

this section for a discussion on symmetry). Symmetry dictated nodes lead to a finite, well-defined, value of $|\Phi_{\underline{\underline{\mathbf{R}}}\,\underline{\underline{\sigma}}}(\underline{\underline{\mathbf{r}}}\,\underline{\underline{\mathbf{s}}}, t)|^2$ due to the linear behavior of the wavefunctions in the vicinity of these nodes.

Eqs. (2.29)-(2.34) determine the *exact* time-dependent molecular wavefunction, given an initial state. As written, the nuclear equation is particularly appealing as a Schrödinger equation with both scalar and vector-potential coupling terms contributing effective forces on the nuclei including any geometric phase effects. We call $\epsilon(\underline{\underline{\mathbf{R}}}\,\underline{\underline{\sigma}}, t)$ and $\mathbf{A}(\underline{\underline{\mathbf{R}}}\,\underline{\underline{\sigma}}, t)$ the *exact TDPES* and *exact time-dependent Berry connection*, respectively. These two quantities, along with the electron-nuclear coupling potential $\hat{U}_{en}^{coup}[\Phi_{\underline{\underline{\mathbf{R}}}\,\underline{\underline{\sigma}}}, \chi]$, mediate the coupling between the nuclear and the electronic degrees of freedom in a formally exact way. The three subsections of Section 2.3 are each devoted to a closer study of these terms.

We conclude this section by discussing the symmetry properties of $\chi(\underline{\underline{\mathbf{R}}}\,\underline{\underline{\sigma}}, t)$ and $\Phi_{\underline{\underline{\mathbf{R}}}\,\underline{\underline{\sigma}}}(\underline{\underline{\mathbf{r}}}\,\underline{\underline{\mathbf{s}}}, t)$: The nuclear wavefunction $\chi(\underline{\underline{\mathbf{R}}}\,\underline{\underline{\sigma}}, t)$ must preserve the symmetry of the full electron-nuclear wavefunction $\Psi(\underline{\underline{\mathbf{r}}}\,\underline{\underline{\mathbf{s}}}, \underline{\underline{\mathbf{R}}}\,\underline{\underline{\sigma}}, t)$ with respect to exchange of identical nuclei. This constrains the allowed gauge transformation (2.46)-(2.47). The electronic wavefunction $\Phi_{\underline{\underline{\mathbf{R}}}\,\underline{\underline{\sigma}}}(\underline{\underline{\mathbf{r}}}\,\underline{\underline{\mathbf{s}}}, t) = \Psi(\underline{\underline{\mathbf{r}}}\,\underline{\underline{\mathbf{s}}}, \underline{\underline{\mathbf{R}}}\,\underline{\underline{\sigma}}, t)/\chi(\underline{\underline{\mathbf{R}}}\,\underline{\underline{\sigma}}, t)$ is invariant under any nuclear permutation because any fermionic sign cancels out between the full molecular wavefunction and the nuclear wavefunction.

In the rest of this work, we drop the spin indices $\underline{\underline{\sigma}}$ and $\underline{\underline{\mathbf{s}}}$ for notational simplicity.

2.2.3 Simple Illustration: the H atom in an electric field

The example of the Hydrogen atom in an electric field provides a simple demonstration of our formalism. The Hamiltonian is

$$H = -\frac{1}{2M}\nabla_R^2 - \frac{1}{2}\nabla_r^2 - \frac{1}{|\boldsymbol{R} - \boldsymbol{r}|} + (\boldsymbol{r} - \boldsymbol{R}) \cdot \mathbf{E}(t) \tag{2.54}$$

where $\boldsymbol{r}$ and $\boldsymbol{R}$ are the electron and proton coordinate respectively, $\mathbf{E}(\mathbf{t})$ is the applied electric field in dipole approximation, and M is the proton mass. The exact solution is known: in terms of the center of mass and relative coordinates, $\mathbf{R}_{\mathrm{CM}} = (\boldsymbol{r} + M\boldsymbol{R})/(M+1), \mathbf{u} = \boldsymbol{r} - \boldsymbol{R}$, the problem is separable, and we have

$$\Psi(\mathbf{R}_{\mathrm{CM}}, \mathbf{u}, t) = e^{i\left(\mathbf{K}\cdot\mathbf{R}_{CM} - \frac{K^2}{2(M+1)}t\right)}\phi(\mathbf{u}, t) \tag{2.55}$$

where $\phi(\mathbf{u},t)$ satisfies the following equation:

$$\left(-\frac{\nabla_u^2}{2\mu}-\frac{1}{u}+\mathbf{u}\cdot\mathbf{E}(t)\right)\phi(\mathbf{u},t)=i\partial_t\phi(\mathbf{u},t) \tag{2.56}$$

and $\mu=M/(M+1)$ is the reduced mass. The full wavefunction, Eq. (2.55), represents free-particle plane-wave motion in the center of mass coordinate, with $\mathbf{K}$ representing the total momentum of the system. The form of Eq. (2.55) suggests one possible factorization for Eqs. (2.24) –(2.25) as:

$$\begin{aligned}\chi(\boldsymbol{R},t) &= e^{i\left(\frac{-K^2t}{2(M+1)}+\frac{M}{(M+1)}\mathbf{K}\cdot\boldsymbol{R}\right)}\\ \Phi_{\boldsymbol{R}}(\mathbf{r},t) &= e^{i\mu\mathbf{K}\cdot\mathbf{r}}\phi(\mathbf{r}-\boldsymbol{R},t)\end{aligned} \tag{2.57}$$

with the exact Berry potential and TDPES given by

$$\mathbf{A}(\mathbf{R},t)=-i\int\phi^*(\mathbf{r}-\mathbf{R},t)\nabla_{\mathbf{R}}\phi(\mathbf{r}-\mathbf{R},t)d\mathbf{r}=0 \tag{2.58}$$

$$\epsilon(\mathbf{R},t)=\frac{K^2}{2(M+1)}+\mathbf{R}\cdot\mathbf{E}(t). \tag{2.59}$$

The vector potential, Eq. (2.58), is zero in the gauge implicit in our choice for Eqs. (2.57). This is easily confirmed by inserting Eqs. (2.57) in the nuclear equation (2.30), which reads for our problem,

$$\left(\frac{1}{2M}\left(-i\nabla+\mathbf{A}\right)^2-\mathbf{R}\cdot\mathbf{E}(t)+\epsilon(\mathbf{R},t)\right)\chi(\mathbf{R},t)=i\partial_t\chi(\mathbf{R},t) \tag{2.60}$$

Eqs. (2.59) and (2.60) show that, in this case the role of the TDPES is to cancel out the external laser field in the nuclear equation, which is exactly as it should be. Only by this cancellation the nuclear motion can be a plane wave.

2.3 The exact electron-nuclear coupling terms

We now take a closer look at each of the three terms $\mathbf{A}(\underline{\underline{\mathbf{R}}}\,\underline{\sigma},t)$, $\epsilon(\underline{\underline{\mathbf{R}}}\,\underline{\sigma},t)$, and $\hat{U}_{en}^{coup}[\Phi_{\underline{\underline{\mathbf{R}}}\,\underline{\sigma}},\chi]$, that mediate the coupling between electron and nuclear dynamics exactly. In these three terms, all of the non-adiabatic coupling effects of the BOexpansion are effectively contained.

2.3.1 The time-dependent vector potential

Eqs. (2.29)-(2.34) demonstrate that a vector-potential indeed appears in the exact treatment of coupled electron-ion dynamics. In this section, we point out some properties of this object to help us understand what it represents.

First, we show that the vector potential $\mathbf{A}_\alpha$ is real. Taking the gradient with respect to nuclear coordinates of the PNC (Eq. (2.25)), yields

$$\begin{aligned} 0 &= \nabla_\alpha \int d\underline{\underline{\mathbf{r}}} \Phi^*_{\underline{\underline{\mathbf{R}}}}(\underline{\underline{\mathbf{r}}}) \Phi_{\underline{\underline{\mathbf{R}}}}(\underline{\underline{\mathbf{r}}}) \\ &= 2\Re \int d\underline{\underline{\mathbf{r}}} \Phi^*_{\underline{\underline{\mathbf{R}}}}(\underline{\underline{\mathbf{r}}}) \nabla_\alpha \Phi_{\underline{\underline{\mathbf{R}}}}(\underline{\underline{\mathbf{r}}}) \end{aligned} \tag{2.61}$$

(using the product rule). Comparing with the definition Eq. (2.34), we readily conclude $\mathbf{A}_\alpha$ is real.

Second, we insert Eqs. (2.27) and (2.26) into Eqs. (2.34) to reveal the following expression for the vector potential:

$$\mathbf{A}_\alpha(\underline{\underline{\mathbf{R}}}, t) = \frac{\Im \langle \Psi(t) | \nabla_\alpha \Psi(t) \rangle_{\underline{\underline{\mathbf{r}}}}}{|\chi(\underline{\underline{\mathbf{R}}}, t)|^2} - \nabla_\alpha S(\underline{\underline{\mathbf{R}}}, t) \tag{2.62}$$

This shows that the vector potential is the difference of the paramagnetic nuclear velocity fields derived from the full and nuclear wavefunctions. In fact, since $\Im \langle \Psi(t) | \nabla_\alpha \Psi(t) \rangle_{\underline{\underline{\mathbf{r}}}}$ is the true nuclear (many-body) current density, Eq. (2.62) implies that the gauge-invariant current density, $\Im(\chi^* \nabla_\alpha \chi) + |\chi|^2 \mathbf{A}_\alpha$, that follows from the nuclear Hamiltonian in Eq. (2.30) does indeed reproduce the exact nuclear current density [38]. As discussed in the previous section, the solution $\chi(\underline{\underline{\mathbf{R}}}, t)$ of Eq. (2.29) yields a proper nuclear many-body wavefunction: Its absolute value squared gives the exact nuclear (N_n-body) density while its phase yields the correct nuclear (N_n-body) current density. (The nuclear kinetic energy evaluated from $\chi(\underline{\underline{\mathbf{R}}}, t)$ does not equal the nuclear kinetic energy evaluated from the full molecular wavefunction, and their difference is determined by U_{en}^{coup}, as will be discussed in Section 2.3.3).

Another interesting aspect of expression (2.62) is that it can help to shed light on the question of whether the exact vector potential gives rise to a Berry phase or whether it can actually be gauged away by a suitable choice of $\theta(\underline{\underline{\mathbf{R}}}, t)$ in Eqs. (2.46)-(2.47). Provided the phase $S(\underline{\underline{\mathbf{R}}}, t)$ is spatially smooth, the last term on the right-hand-side of Eq. (2.62) can be gauged away, so any true Berry connection (that cannot be gauged

away) must come from the first term. When the exact $\Psi(t)$ is real-valued (e.g. for a non-current-carrying ground state) then the first term on the right-hand-side of Eq. (2.62) vanishes and hence gives a vanishing contribution to the exact Berry connection. Whether, and under which conditions, the full vector potential (2.62) can be gauged away remains an open question at this point. We will discuss this issue further with numerical examples in chapter (3).

Finally, it is also instructive to express the vector potential in terms of the BO electronic basis states of Section 2.1.2. We first expand the electronic wavefunction:

$$\Phi_{\underline{\underline{\mathbf{R}}}}(\underline{\mathbf{r}},t)=\sum_{j=1}^{\infty}C_j(\underline{\underline{\mathbf{R}}},t)\phi^j_{\underline{\underline{\mathbf{R}}}}(\underline{\mathbf{r}}) \tag{2.63}$$

where orthonormality of the ϕ^j (Eq. (2.17)) means

$$C_j(\underline{\underline{\mathbf{R}}},t)=\int d\underline{\mathbf{r}}\,\phi^{j*}_{\underline{\underline{\mathbf{R}}}}(\underline{\mathbf{r}})\Phi_{\underline{\underline{\mathbf{R}}}}(\underline{\mathbf{r}},t)\ . \tag{2.64}$$

The PNC condition becomes

$$\sum_{j=1}^{\infty}|C_j(\underline{\underline{\mathbf{R}}},t)|^2=1. \tag{2.65}$$

Inserting Eq. (2.63) into Eq. (2.34), and noting the definition of the non-adiabatic derivative coupling $\mathcal{F}^{BO}_{kj,\alpha}(\underline{\underline{\mathbf{R}}})$ of Eq. 2.23, we obtain

$$\begin{aligned}\mathbf{A}_\alpha(\underline{\underline{\mathbf{R}}},t)=\sum_{j=1}^{\infty}\Big(&-iC_j^*(\underline{\underline{\mathbf{R}}},t)\nabla_\alpha C_j(\underline{\underline{\mathbf{R}}},t)\quad+\quad|C_j(\underline{\underline{\mathbf{R}}},t)|^2\mathcal{F}^{BO}_{jj,\alpha}(\underline{\underline{\mathbf{R}}})\\&+\sum_{l\neq j}^{\infty}C_l^*(\underline{\underline{\mathbf{R}}},t)C_j(\underline{\underline{\mathbf{R}}},t)\mathcal{F}^{BO}_{lj,\alpha}(\underline{\underline{\mathbf{R}}})\Big)\ .\end{aligned} \tag{2.66}$$

The exact Berry potential is thereby expressed as a linear combination of the diagonal and off-diagonal BO derivative couplings. Any gauge-invariant part of the Berry connection, that would give rise to a non-zero Berry phase, arises from the part of Eq. 2.66 that has a non-zero curl. In the case of a real-valued electronic wavefunction, each of the three terms of Eq. 2.66 vanishes independently giving rise to a zero vector potential.

2.3.2 The Time-Dependent Potential Energy Surface

The TDPES $\epsilon(\underline{\underline{\mathbf{R}}}, t)$ of Eq. (2.33) provides an exact time-dependent generalization of the adiabatic BO potential energy surface. As such, it should prove to be a powerful interpretive tool for general time-dependent problems. This will be explored in chapter (4). We now begin by analyzing the expression Eq. (2.33) in a little more detail.

First, consider the expectation value of the electron-nuclear coupling term, $\langle \Phi_{\underline{\underline{\mathbf{R}}}} | \hat{U}_{en}^{coup} | \Phi_{\underline{\underline{\mathbf{R}}}} \rangle$ of Eq. (2.32) that appears in the TDPES. Only the first term of Eq. (2.32) contributes to the expectation value: the second term goes to zero, due to the very last parenthesis, $\langle \Phi_{\underline{\underline{\mathbf{R}}}} | -i\nabla_\alpha - \mathbf{A}_\alpha(\underline{\underline{\mathbf{R}}}, t) | \Phi_{\underline{\underline{\mathbf{R}}}} \rangle$, which vanishes due to the definition of the vector potential (2.34). So we have

$$\begin{aligned} \epsilon(\underline{\underline{\mathbf{R}}}, t) = \langle \Phi_{\underline{\underline{\mathbf{R}}}} | \hat{H}_{BO} + \hat{V}_e^{ext}(\underline{\underline{\mathbf{r}}}, t) | \Phi_{\underline{\underline{\mathbf{R}}}} \rangle_{\underline{\underline{\mathbf{r}}}} \quad &- \quad i \langle \Phi_{\underline{\underline{\mathbf{R}}}} | \partial_t \Phi_{\underline{\underline{\mathbf{R}}}} \rangle_{\underline{\underline{\mathbf{r}}}} + \\ &\sum_\alpha \frac{\langle \Phi_{\underline{\underline{\mathbf{R}}}} | \left(-i\nabla_\alpha - \mathbf{A}_\alpha(\underline{\underline{\mathbf{R}}}, t) \right)^2 | \Phi_{\underline{\underline{\mathbf{R}}}} \rangle_{\underline{\underline{\mathbf{r}}}}}{2M_\alpha} \\ = \langle \Phi_{\underline{\underline{\mathbf{R}}}} | \hat{H}_{BO} + \hat{V}_e^{ext}(\underline{\underline{\mathbf{r}}}, t) | \Phi_{\underline{\underline{\mathbf{R}}}} \rangle_{\underline{\underline{\mathbf{r}}}} \quad &- \quad i \langle \Phi_{\underline{\underline{\mathbf{R}}}} | \partial_t \Phi_{\underline{\underline{\mathbf{R}}}} \rangle_{\underline{\underline{\mathbf{r}}}} + \\ &\sum_\alpha \frac{\langle \nabla_\alpha \Phi_{\underline{\underline{\mathbf{R}}}} | \nabla_\alpha \Phi_{\underline{\underline{\mathbf{R}}}} \rangle_{\underline{\underline{\mathbf{r}}}}}{2M_\alpha} - \sum_\alpha \frac{\mathbf{A}_\alpha^2(\underline{\underline{\mathbf{R}}}, t)}{2M_\alpha} \end{aligned} \tag{2.67}$$

where the second line results from expanding the square in the first, and making use of the definition of the vector potential (2.34).

As we did for the vector potential, we now provide an expression for the TDPES as an expansion over BO states. Inserting Eq. (2.63) into Eq. (2.67) and performing a little straightforward algebra, we obtain

$$\begin{aligned}\epsilon(\underline{\underline{\mathbf{R}}},t) &= \sum_j |C_j(\underline{\underline{\mathbf{R}}},t)|^2 V^j_{BO}(\underline{\underline{\mathbf{R}}}) \\ &+ \sum_{jl} C^*_j(\underline{\underline{\mathbf{R}}},t) C_l(\underline{\underline{\mathbf{R}}},t) \langle \phi^j_{\underline{\underline{\mathbf{R}}}} | \hat{V}^{ext}_e(\underline{\mathbf{r}},t) | \phi^l_{\underline{\underline{\mathbf{R}}}} \rangle_{\underline{\mathbf{r}}} - \sum_j i C^*_j(\underline{\underline{\mathbf{R}}},t) \partial_t C_j(\underline{\underline{\mathbf{R}}},t) \\ &+ \sum_\alpha \frac{1}{2M_\alpha} \Big[\sum_j |\nabla_\alpha C_j|^2 + \sum_{jl} C^*_j C_l \left(i\nabla_\alpha \cdot \mathcal{F}^{BO}_{jl,\alpha} - \mathcal{G}^{BO}_{jl,\alpha} \right) \\ &\qquad - 2 \sum_{jl} \Im\big(C_l \nabla_\alpha C^*_j \mathcal{F}^{BO}_{jl,\alpha} \big) - \mathbf{A}^2_\alpha(\underline{\underline{\mathbf{R}}},t) \Big] \end{aligned} \tag{2.68}$$

(the expansion of the last term $\mathbf{A}^2_\alpha$ may be obtained from Eq. 2.66). Notice that all the BO surfaces, as well as non-adiabatic couplings, are contained in the the exact TDPES.

2.3.3 Electron-Nuclear Correlation

The TDPES and Berry connection discussed in the previous two sections directly determine the evolution of the nuclear wavefunction (Eq. (2.30)), containing the effect of coupling to the electrons in an exact way. The electron-nuclear coupling term $\hat{U}^{coup}_{en}$ enters the nuclear equation indirectly via its role in determining $\Phi_{\underline{\underline{\mathbf{R}}}}$ through Eq. (2.29) and (5.5). Eq. (2.32) expresses $\hat{U}^{coup}_{en}$ as a functional of the electronic and nuclear wavefunctions, and now we shall derive another expression for it that shows that it measures the difference between the nuclear kinetic energy evaluated from the full wavefunction and that evaluated on the nuclear wavefunction. We isolate the term involving $\hat{U}^{coup}_{en}$ in Eq. (2.29), and insert $\Phi_{\underline{\underline{\mathbf{R}}}} = \Psi/\chi$. This leads to:

$$\frac{\hat{U}^{coup}_{en}\Phi_{\underline{\underline{\mathbf{R}}}}}{\Phi_{\underline{\underline{\mathbf{R}}}}} = \frac{i\partial_t \Psi}{\Psi} - \frac{i\partial_t \chi}{\chi} - \frac{\hat{H}_{BO}\Phi_{\underline{\underline{\mathbf{R}}}}}{\Phi_{\underline{\underline{\mathbf{R}}}}} - \hat{V}^e_{\text{ext}} + \epsilon(\underline{\underline{\mathbf{R}}},t) \; . \tag{2.69}$$

Next we insert in Eq. (2.69) the TDSE (2.11) and (2.30), satisfied by Ψ and χ to obtain

$$\frac{\hat{U}^{coup}_{en}\left[\Phi_{\underline{\underline{\mathbf{R}}}},\chi\right]\Phi_{\underline{\underline{\mathbf{R}}}}(\underline{\mathbf{r}},t)}{\Phi_{\underline{\underline{\mathbf{R}}}}(\underline{\mathbf{r}},t)} = \frac{\hat{T}_n\Psi}{\Psi} - \frac{\hat{\tilde{T}}_n\chi}{\chi} \tag{2.70}$$

where

$$\hat{\tilde{T}}_n = \sum_{\alpha=1}^{N_n} \frac{1}{2M_\alpha}(-i\nabla_\alpha + \mathbf{A}_\alpha(\underline{\underline{\mathbf{R}}},t))^2 \tag{2.71}$$

Multiplying Eq. (2.70) by $|\Phi_{\underline{\underline{\mathbf{R}}}}|^2|\chi|^2$ and integrating over all coordinates leads to:

$$\langle\Psi|\hat{T}_n|\Psi\rangle_{\underline{\mathbf{r}},\underline{\underline{\mathbf{R}}}} - \langle\chi|\hat{\tilde{T}}_n|\chi\rangle_{\underline{\underline{\mathbf{R}}}} = \int d\underline{\underline{\mathbf{R}}}|\chi(\underline{\underline{\mathbf{R}}},t)|^2\langle\Phi_{\underline{\underline{\mathbf{R}}}}|\hat{U}_{en}^{coup}|\Phi_{\underline{\underline{\mathbf{R}}}}\rangle_{\underline{\mathbf{r}}}. \tag{2.72}$$

This means the nuclear kinetic energy evaluated from the full molecular wavefunction, and that evaluated via the expectation value of the nuclear kinetic energy operator in Eq. (2.30) on the nuclear wavefunction are not equal: their difference is given by the nuclear-density-weighted integral of the electron-nuclear coupling potential.

2.4 Conclusions

In this chapter, we have shown that there exists a rigorous factorization of the exact molecular wavefunction into a nuclear wavefunction and an electronic wavefunction, each of which retains the usual probabilistic meaning. The exact nuclear N_n-body density is $|\chi(\underline{\underline{\mathbf{R}}},t)|^2$ while $|\Phi_{\underline{\underline{\mathbf{R}}}}(\underline{\mathbf{r}},t)|^2$ represents the conditional probability of finding the electrons at $\underline{\mathbf{r}}$, given the nuclear configuration $\underline{\underline{\mathbf{R}}}$. Equations (2.29)—(2.34) are the equations of motion that the electronic wavefunction and nuclear wavefunction satisfy, and show explicitly how the electronic and nuclear systems are exactly coupled. These equations enable the TDPES (Eq. (2.33)) and the time-dependent vector potential (Eq. (2.34)) to be defined as rigorous concepts, and we have discussed some general properties of them, and of the electron-nuclear coupling operator Eq. (2.32). The crucial point of our work is that it provides a *unique* definition of TDPES and time-dependent vector potential (unique up to within a gauge transformation): If one wants the TD many-body Schrödinger equation (2.30) to give the correct N-body density and current density of the nuclei, then the scalar potential and the vector potential *must* be given by eq. (2.33) and (2.34). There is no choice apart from the gauge. That means that with any advanced technique that yields the TD molecular wavefunction $\Psi(\underline{\mathbf{r}},\underline{\underline{\mathbf{R}}},t)$ one can evaluate the TDPES and vector potential by first calculating the factors from Eqs. (2.27)-(2.26) and then evaluating the TDPES and vector potential from Eqs. (2.33)-(2.34).

From a practical point of view, Eqs. (2.29)-(2.34) are not easier to solve than the time-dependent Schrödinger equation for the full electron-nuclear system. Rather they form the rigorous starting point for making approximations, especially for the systematic development of (semi)classical approximations (see Chapter 4).

Chapter 3

Exact Static Potential Energy Surfaces: A fresh look at an old concept

In the previous Chapter (2), we presented an exact factorization of the full time-dependent electron-nuclear wavefunction. The idea of an exact factorization was first introduced by Hunter [1] for the static case. He also deduced the exact equation of motion for the nuclear factor and introduced a concept of *non-adiabatic* potential energy surfaces for the static case [39]. Following Hunter's work on the non-adiabatic potentials, Czub and Wolniewicz [37] discovered the nodeless character of the nuclear wavefunction for diatomic molecules and showed that the corresponding non-adiabatic potentials exhibit spikes where the vibrational states have nodes. This was later investigated by Hunter [36, 40] as well. The equation for the electronic factor for the time-independent case was given, some two decades later, by Gidopoulos and Gross [33, 34]. They also provide a neat variational derivation of the equations and present the nuclear equation that contains an *exact* vector potential as well as an *exact* potential energy surface (EPES).

In this Chapter, we first briefly review the exact factorization of the electron-nuclear wavefunction for the static case, presented in [33, 34](Section 3.1). Then, we discuss the EPES of two cases in which the relevant BO surfaces exhibit points of avoided crossing and conical intersection (Section 3.2.4). Before entering the discussion of the EPESs, we present the model systems that are used to study the exact surfaces and the procedure of calculating them (Section 3.2).

3.1 Exact factorization for the static case in a nutshell

The exact factorization of the full molecular state suggests that a molecular state, $\Psi^K(\underline{\mathbf{r}}, \underline{\underline{\mathbf{R}}})$, that is a solution of the time-independent Schrödinger equation,

$$\hat{H}\Psi^K(\underline{\mathbf{r}}, \underline{\underline{\mathbf{R}}}) = E^K \Psi^K(\underline{\mathbf{r}}, \underline{\underline{\mathbf{R}}}), \tag{3.1}$$

can be represented, formally exactly, as a product of the nuclear factor $\chi^K(\underline{\underline{\mathbf{R}}})$ and the electronic factor $\Phi^K_{\underline{\underline{\mathbf{R}}}}(\underline{\mathbf{r}})$, i.e.,

$$\Psi^K(\underline{\mathbf{r}}, \underline{\underline{\mathbf{R}}}) = \chi^K(\underline{\underline{\mathbf{R}}})\Phi^K_{\underline{\underline{\mathbf{R}}}}(\underline{\mathbf{r}}) \tag{3.2}$$

where the electronic factor satisfies the PNC:

$$\int d\underline{\mathbf{r}} |\Phi^K_{\underline{\underline{\mathbf{R}}}}(\underline{\mathbf{r}})|^2 = 1, \tag{3.3}$$

for each fixed nuclear configuration $\underline{\underline{\mathbf{R}}}$. As proved by Gidopoulos and Gross [33, 34], varying the expectation value of the molecular Hamiltonian (2.2), $\hat{H}$, with respect to $\Phi^K_{\underline{\underline{\mathbf{R}}}}(\underline{\mathbf{r}})$ and $\chi^K(\underline{\underline{\mathbf{R}}})$, under the PNC, leads to derivation of the electronic equation,

$$\hat{H}^K_{el}(\underline{\mathbf{r}}, \underline{\underline{\mathbf{R}}})\Phi^K_{\underline{\underline{\mathbf{R}}}}(\underline{\mathbf{r}}) = \epsilon^K(\underline{\underline{\mathbf{R}}})\Phi^K_{\underline{\underline{\mathbf{R}}}}(\underline{\mathbf{r}}), \tag{3.4}$$

and, nuclear equation,

$$\Big(\sum_{\alpha=1}^{N_n} \frac{1}{2M_\alpha}(-i\nabla_\alpha + \mathbf{A}^K_\alpha(\underline{\underline{\mathbf{R}}}))^2 + \hat{V}^{ext}_n(\underline{\underline{\mathbf{R}}}) + \epsilon^K(\underline{\underline{\mathbf{R}}})\Big)\chi^K(\underline{\underline{\mathbf{R}}}) = E^K\chi^K(\underline{\underline{\mathbf{R}}}). \tag{3.5}$$

Here, the electronic Hamiltonian is

$$\hat{H}^K_{el}(\underline{\mathbf{r}}, \underline{\underline{\mathbf{R}}}) = \hat{H}_{BO}(\underline{\mathbf{r}}, \underline{\underline{\mathbf{R}}}) + \hat{V}^{ext}_e(\underline{\mathbf{r}}) + \hat{U}^{coup,K}_{en}, \tag{3.6}$$

and the electron-nuclear coupling operator $\hat{U}_{en}^{coup,K}$, scalar potential $\epsilon^K(\underline{\underline{\mathbf{R}}})$, and vector potential $\mathbf{A}_\alpha^K(\underline{\underline{\mathbf{R}}})$ terms are

$$\hat{U}_{en}^{coup,K} = \sum_{\alpha=1}^{N_n} \frac{1}{M_\alpha}\Big[\frac{(-i\nabla_\alpha - \mathbf{A}_\alpha^K(\underline{\underline{\mathbf{R}}}))^2}{2} + \Big(\frac{-i\nabla_\alpha \chi^K}{\chi^K} + \mathbf{A}_\alpha^K(\underline{\underline{\mathbf{R}}})\Big)\cdot\big(-i\nabla_\alpha - \mathbf{A}_\alpha^K(\underline{\underline{\mathbf{R}}})\big)\Big] \tag{3.7}$$

$$\epsilon^K(\underline{\underline{\mathbf{R}}}) = \sum_{\underline{\mathbf{s}}} \Big\langle \Phi_{\underline{\underline{\mathbf{R}}}}^K \Big| \hat{H}_{el}^K((\underline{\mathbf{r}},\underline{\underline{\mathbf{R}}}) \Big| \Phi_{\underline{\underline{\mathbf{R}}}}^K \Big\rangle_{\underline{\mathbf{r}}} \tag{3.8}$$

$$\mathbf{A}_\alpha^K(\underline{\underline{\mathbf{R}}}) = \Big\langle \Phi_{\underline{\underline{\mathbf{R}}}}^K \Big| -i\nabla_\alpha \Phi_{\underline{\underline{\mathbf{R}}}}^K \Big\rangle_{\underline{\mathbf{r}}}, \tag{3.9}$$

where $\epsilon^K(\underline{\underline{\mathbf{R}}})$ is invariant under the gauge-transformation

$$\tilde{\Phi}_{\underline{\underline{\mathbf{R}}}}^K(\underline{\mathbf{r}}) := e^{i\theta_K(\underline{\underline{\mathbf{R}}})}\Phi_{\underline{\underline{\mathbf{R}}}}^K(\underline{\mathbf{r}}), \tag{3.10}$$

and the vector potential is transformed as

$$\mathbf{A}_\alpha^K(\underline{\underline{\mathbf{R}}}) \to \tilde{\mathbf{A}}_\alpha^K(\underline{\underline{\mathbf{R}}}) = \mathbf{A}_\alpha^K(\underline{\underline{\mathbf{R}}}) + \nabla_\alpha \theta_K(\underline{\underline{\mathbf{R}}}). \tag{3.11}$$

Eqs. (3.4-3.5), like the time-dependent version (2.29-2.30), are form invariant under the gauge transformation

$$\begin{aligned} \tilde{\Phi}_{\underline{\underline{\mathbf{R}}}}^K(\underline{\mathbf{r}}) &:= e^{i\theta_K(\underline{\underline{\mathbf{R}}})}\Phi_{\underline{\underline{\mathbf{R}}}}^K(\underline{\mathbf{r}}) \\ \tilde{\chi}^K(\underline{\underline{\mathbf{R}}}) &:= e^{-i\theta_K(\underline{\underline{\mathbf{R}}})}\chi^K(\underline{\underline{\mathbf{R}}}), \end{aligned} \tag{3.12}$$

i.e. , the products $\tilde{\Phi}_{\underline{\underline{\mathbf{R}}}}^K(\underline{\mathbf{r}})\tilde{\chi}^K(\underline{\underline{\mathbf{R}}})$ and $\Phi_{\underline{\underline{\mathbf{R}}}}^K(\underline{\mathbf{r}})\chi^K(\underline{\underline{\mathbf{R}}})$ are equivalent representations of the full wavefunction, $\Psi^K(\underline{\mathbf{r}},\underline{\underline{\mathbf{R}}})$, that is an eigenstate of the full electron-nuclear Hamiltonian (2.2).

Here we should emphasize the difference between the BO approximation and the exact factorization as the two may look very similar at first sight: in the exact factorization, unlike the BO approximation, we do not solve the electronic equation (2.12) first and then feed the nuclear equation with the calculated potential, ϵ_{BO}^j, to obtain the vibrational states, $\chi_{j\nu}^{BO}$. Instead, the equations of motion for each subsystem are derived together, in a variational approach. The resulting electronic equation (3.4) then depends on the nuclear wavefunction and the Eqs. (3.4) and (3.5) must be solved self consistently. That is why there is one and the same index, K, for both the electronic and nuclear wavefunctions and their product yields the eigenstate of the full molecular

system with the same quantum number. Therefore, contrary to the BO separation, The exact decomposition accounts for the full coupling between the electrons and nuclei, regardless of the nuclear mass and energy.

As shown above, an exact concept of potential energy surface (3.8) emerges from the exact factorization of the molecular wavefunction for the static case. So far, only the exact potential energy surfaces close to the molecular ground state of a few systems have been investigated [36, 37, 40]. The main difference between the investigated exact surfaces and the BO surface of the ground-state are the presence of spikes at the position of the nodes of the vibrational states. This feature is due to the nodeless character of the exact nuclear densities and can be seen by expanding the full molecular state, $\Psi^K(\underline{\mathbf{r}}, \underline{\underline{\mathbf{R}}})$, in terms of the BO-electronic states (similar to Eq. (2.18)). Then, the corresponding nuclear density can be expressed as an infinite sum of non-negative terms:

$$|\chi^K(\underline{\underline{\mathbf{R}}})|^2 = \sum_{j=1}^{\infty} |\chi_j^{BO,K}(\underline{\underline{\mathbf{R}}})|^2 \,, \tag{3.13}$$

where $\chi_j^{BO,K}(\underline{\underline{\mathbf{R}}}) =< \phi^j_{\underline{\underline{\mathbf{R}}}} | \Psi^K >_{\underline{\mathbf{r}}}$. In general, it is extremely unlikely that every term in the summation becomes zero at the same nuclear configuration $\underline{\underline{\mathbf{R}}}_0$, unless dictated by symmetry [33, 34]. Hence, the exact nuclear density may become nodeless where the corresponding BO-vibrational state is zero. In that case the corresponding exact potential energy surface (3.8) exhibits a spike for the same nuclear configuration. Since contributions from another electronic states make the exact nuclear density depart from being zero, the spikes of the exact potential energy surfaces may be considered as non-adiabatic corrections and remained the only feature of the exact surfaces that has been addressed so far. However, the spikes of the EPESs and the nodeless character of the exact nuclear wave-function are not considered among the very important non-adiabatic effects that cause the breakdown of the BO approximation.

The main focus of this chapter is to study the EPES for two different cases (Section 3.3 and 3.4) in which the BO approximation dramatically breaks down. This breakdown happens often in photochemistry of polyatomic molecules due to a large number of energetically close electronic states involved in the molecular processes. In such situations, we usually deal with the *avoided crossings* of the BOPESs or with the points of exact degeneracy of BO surfaces, i.e., *conical intersections*. Points of avoided crossings and

conical intersections of BO surfaces provide pathways for radiationless relaxation processes and ultrafast interstate crossings once the photochemical processes are studied within the BO framework. However, experimental data or exact solution of the TDSE (if accessible) can only infer to these points and an investigation of the relevant BO surfaces is required to confirm that such points actually exist. Another phenomenon related to the conical intersection, is the Berry phase effect [25, 41, 42], i.e., electronic wave-function changes sign after completing a closed path around the conical intersection. Therefore, in the adiabatic description of molecular processes the corresponding vibrational wave-function should also be double-valued such that the full wave-function is single-valued. In the Herzberg and Longuet-Higgens model [25, 43], for example, the two (single-valued) nuclear wavefunctions associated with a two-state conical intersection between traditional BO surfaces, each have a phase $S = \pm\phi/2$, undefined at the origin. This has a singular gradient, yielding a delta-function at the origin in the curl of the vector potential, thus contributing a non-zero Berry phase. Whether a similar effect may occur for the exact vector potential remains to be explored.

3.2 Description of the Models

3.2.1 H_2^+ in One Dimension

A one dimensional model for the H_2^+ molecular ion, subject to a linearly polarized laser field, can be made by restricting the motion of the nuclei and the electron to the direction of the polarization axis of the laser field. Hence, the problem can be modeled with a 1D Hamiltonian featuring "soft-Coulomb" interactions [44–48]:

$$\hat{H}(t) = -\frac{1}{2\mu_e}\frac{\partial^2}{\partial x^2} - \frac{1}{M}\frac{\partial^2}{\partial R^2} - \frac{1}{\sqrt{1+(x-R/2)^2}} - \frac{1}{\sqrt{1+(x+R/2)^2}} + \frac{1}{\sqrt{0.03+R^2}} + \hat{V}_l(x,t) \tag{3.14}$$

where R and x are the internuclear distance and the electronic coordinate as measured from the nuclear center-of-mass, respectively, and the electronic reduced mass is given by $\mu_e = (2M)/(2M+1)$, M being the proton mass. The laser field, within dipole approximation, is represented by $\hat{V}_l(x,t) = q_e x E(t)$ where $E(t)$ denotes the electric field amplitude and the reduced charge $q_e = (2M+2)/(2M+1)$. One-dimensional soft-Coulomb atoms and molecules have proven extremely useful in the study of strong-field dynamics since

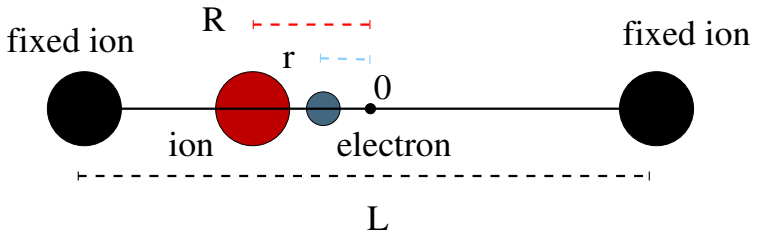

FIGURE 3.1: A sketch of the Shin-Metiu model. The two black solid circles represent the two identical ions that are held fixed at distance L. The movable ion (red solid circle) is restricted to move on the line connecting the two fixed ions but the electron (blue solid circle) can go beyond the fixed ions.

they allow numerically accurate solutions to problems involving correlated electron dynamics as well as correlated electron-nuclear dynamics that would be computationally far more demanding for the full three-dimensional atoms and molecules, while capturing the essential physics of the latter, e.g. multi-photon ionization, above-threshold ionization and dissociation, enhanced ionization, non-sequential double-ionization, high-harmonic generation, and non-BO effects (e.g. Refs. [46–53]). In simplifying the real molecule to a 1D-model it is assumed that: (i) The molecule is always aligned with the polarization axis of the laser field. (ii) Due to the linear polarization of the laser field, the magnetic quantum number of the electron is conserved. (iii) The electron mostly follows the applied field.

3.2.2 Shin-Metiu Model

This model was introduced by Shin and Metiu [54] to study the non-adiabatic coupling between the electronic and nuclear motion in charge transfer dynamics. It consists of three ions and a single electron (figure 3.1). Two ions are fixed at a distance of L, the third ion and the electron are free to move in one dimension along the line joining the two fixed ions. The Hamiltonian of this system reads

$$\begin{aligned}\hat{H}(r,R) = &-\frac{1}{2}\frac{\partial^2}{\partial r^2} - \frac{1}{2M}\frac{\partial^2}{\partial R^2} + \frac{1}{|\frac{L}{2}-R|} + \frac{1}{|\frac{L}{2}+R|} \\ &- \frac{\operatorname{erf}\left(\frac{|R-r|}{R_f}\right)}{|R-r|} - \frac{\operatorname{erf}\left(\frac{|r-\frac{L}{2}|}{R_r}\right)}{|r-\frac{L}{2}|} - \frac{\operatorname{erf}\left(\frac{|r+\frac{L}{2}|}{R_l}\right)}{|r+\frac{L}{2}|}.\end{aligned} \tag{3.15}$$

Here, the symbols $\underline{\mathbf{r}}$ and $\underline{\underline{\mathbf{R}}}$ are replaced by r and R, the coordinates of the electron and the movable ion measured from the center of the two fixed ions and M is the

nuclear mass. The parameters, R_f, R_l and R_r, can be chosen to produce different coupling strength between the electronic and nuclear motions. In Hamiltonian (3.15), the electron interacts with each of the ions via a soft coulomb potential,

$$\hat{V}_{en} = -Z\frac{\operatorname{erf}\left(\frac{|r-R_n|}{R_c}\right)}{|r-R_n|}, \tag{3.16}$$

where Z is the ion charge, here, equal to one for all the three, r and R_n are the position of the electron and ions, respectively, and,

$$\operatorname{erf}(x) = \frac{2}{\sqrt{\pi}}\int_0^x e^{-t^2}\,\mathrm{d}t, \tag{3.17}$$

is the *error function*. The softening parameter, R_c, can be chosen differently (R_f, R_l and R_r) for the interaction with each of the ions.

3.2.3 H_3^{2+} in two dimensions

In a system with N_n nuclear degrees of freedom, degenerate points of the BOPESs lie in what is called the intersection space, or seam. The dimensionality of the seam is $N_n - 2$. Therefore, to have a *point* as the intersection between the BO surfaces there should be two nuclear degrees of freedom. In order to produce such a situation we set up a 2-dimensional model Hamiltonian that consists of two fixed nuclei apart from each other with a distance L, represented by the vectors $\mathbf{R}_- = (-L/2, 0)$ and $\mathbf{R}_+ = (L/2, 0)$, one moving ion and one moving electron interacting with each other with soft Coulomb interaction, mimicking H_3^{2+} molecular ion (see Fig. 3.2). The Hamiltonian of this system reads

$$\begin{aligned}\hat{H}_{tot}\left(\boldsymbol{r},\mathbf{R}\right) \;=\; & -\frac{\nabla^2_{\mathbf{R}}}{2M} - \frac{\nabla^2_{\boldsymbol{r}}}{2} + \\ & \frac{-1}{\sqrt{a+|\boldsymbol{r}-\mathbf{R}_+|^2}} + \frac{-1}{\sqrt{a+|\boldsymbol{r}-\mathbf{R}_-|^2}} + \frac{-1}{\sqrt{a+|\boldsymbol{r}-\mathbf{R}|^2}} + \\ & \frac{1}{\sqrt{b+|\mathbf{R}-\mathbf{R}_+|^2}} + \frac{1}{\sqrt{b+|\mathbf{R}-\mathbf{R}_-|^2}} + \frac{1}{\sqrt{b+L^2}} + \\ & V_{conf}(\mathbf{R})\end{aligned} \tag{3.18}$$

where $\boldsymbol{r} = (x, y)$ and $\mathbf{R} = (X, Y)$ are the positions of the electron and moving ion with a mass M, respectively. The additional confinement potential $V_{conf}(\mathbf{R})$,

$$V_{conf}(\mathbf{R}) = \left(\frac{R}{R_0}\right)^4, \tag{3.19}$$

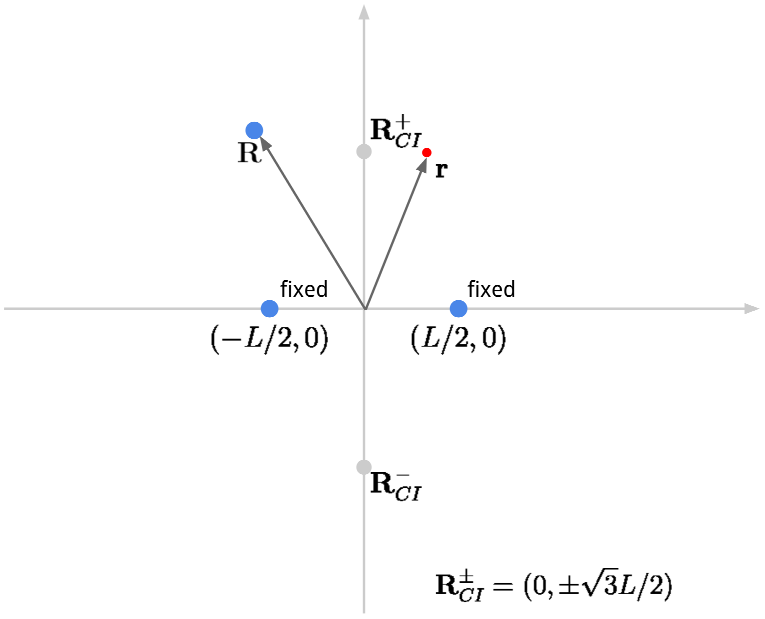

FIGURE 3.2: A sketch of the H_3^{2+} model. The two blue solid circles along the X axis represent two identical ions that are held fixed at the denoted points. Movable ion (blue solid circle) and the electron (red solid circle) are free to move on the XY plane. To make the model system bound, a confinement potential (see the tex) is introduced. The positions of the conical intersections between the first excited BO surface and the second excited BO surface are marked by two gray solid circles along the Y axis.

is introduced to make the system bound. The values of the parameters a, b and R_0 can be chosen arbitrarily to produce different coupling strength between the electronic and nuclear motions.

3.2.4 Details of the calculations

In order to obtain the EPESs (3.8), we first solve the full molecular eigenvalue problem (3.1) and calculate the full molecular eigenstates, Ψ^K. In all the cases we study here, the molecular states are not current-carrying, hence Ψ^K is real. Therefore, as the first choice we set $\chi = \sqrt{\int d\underline{\underline{\mathbf{r}}} |\Psi|^2}$ and calculate $\Phi_{\underline{\underline{\mathbf{R}}}}(\underline{\underline{\mathbf{r}}})$ ($\Phi_{\underline{\underline{\mathbf{R}}}}(\underline{\underline{\mathbf{r}}}) = \Psi/\chi$). Then we check if $\Phi_{\underline{\underline{\mathbf{R}}}}(\underline{\underline{\mathbf{r}}})$ is single valued. If so, $\Phi_{\underline{\underline{\mathbf{R}}}}(\underline{\underline{\mathbf{r}}})$ can be chosen real as it was and the vector potential (3.9), $\mathbf{A}_\nu(\underline{\underline{\mathbf{R}}})$, is always zero. This is indeed the case in all the three cases we have studied. From the calculated $\Phi_{\underline{\underline{\mathbf{R}}}}(\underline{\underline{\mathbf{r}}})$ and χ we can calculate the EPESs either from Eq. (3.8) or by inverting the Eq. (3.5).

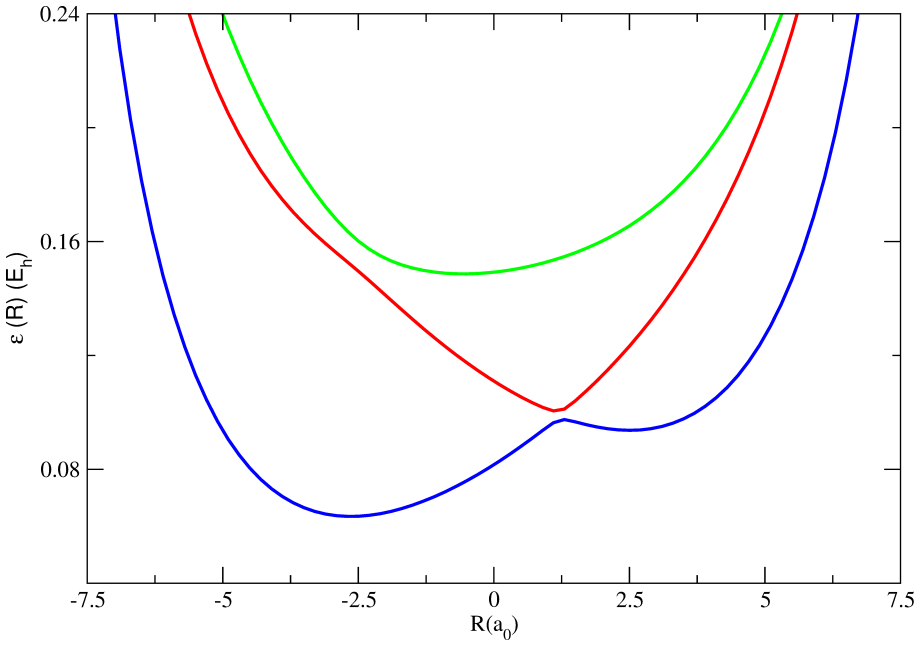

FIGURE 3.3: The first three BOPESs of the Shin-Metiu-Model (3.2.2) for $R_f = 5.0\ a_0$, $R_l = 3.45\ a_0$ and $R_r = 3.0\ a_0$: V^1_{BO} (blue); V^2_{BO} (red); and V^3_{BO} (green).

3.3 Strong Coupling I

We consider a situation when the electronic and nuclear motions are strongly coupled. This strong coupling in the BO framework is called the non-adiabatic couplings between different electronic states. Here we employ the Shin-Metiu model described in (3.2.2) with $R_f = 5.0\ a_0$, $R_l = 3.45\ a_0$ and $R_r = 3.0\ a_0$ to study the exact potential surfaces in a strong electron-nuclear coupling regime. The first three BOPESs of the system are plotted in figure (3.3). There are two avoided crossings between the plotted BOPESs: one between V^1_{BO} and V^2_{BO} around $R_{ac12} = 1.25\ a_0$ and the other one between V^2_{BO} and V^3_{BO} around $R_{ac23} = -3.0\ a_0$.

The electron-nuclear coupling potential (3.7), $\hat{U}^{coup,K}_{en}$, in the exact electronic equation (3.4) is inversely proportional to the nuclear mass. In the limit of infinite nuclear masses, $\hat{U}^{coup,K}_{en}$ becomes zero and the exact electronic equation becomes identical with the BO electronic equation (2.12). Hence, the BOPESs (2.14) can be viewed as the infinite nuclear mass limit of the exact potential energy surfaces (3.8). The other extreme limit for the electron-nuclear coupling potential (3.7) happens when the nuclear mass is equal to the electronic mass. The first three exact potential energy surfaces for this case are shown in Figure (3.4). Surprisingly, the exact surfaces are similar to the

N_R	ΔR (a_0)	R_{max} (a_0)	N_r	Δr (a_0)	$\lvert r_{max}\rvert$ (a_0)
96	0.1	9.5	251	0.1	25

TABLE 3.1: Numerical parameters employed for the numerical calculation of Shin-Metiu model (sec. 3.3)

diabatic surfaces as they follow the shape of one of the BO surfaces, go smoothly through the region of avoided crossings and switch to follow another BO surface. In a diabatic representation the full molecular wave-function is described in terms of diabatic states, $d^j_{\underline{\underline{\mathbf{R}}}}(\underline{\mathbf{r}})$,

$$\Psi(\underline{\mathbf{r}},\underline{\underline{\mathbf{R}}}) = \sum_j \beta_j(\underline{\underline{\mathbf{R}}}) d^j_{\underline{\underline{\mathbf{R}}}}(\underline{\mathbf{r}}). \tag{3.20}$$

However, the diabatic representation is not unique and depending on the problem one must find the most convenient diabatic states to describe the full wave-function. The diabatic electronic wave-functions, $d^j_{\underline{\underline{\mathbf{R}}}}(\underline{\mathbf{r}})$, are the eigenstates of different electronic Hamiltonians, H_j,

$$\hat{H}_j d^j_{\underline{\underline{\mathbf{R}}}}(\underline{\mathbf{r}}) = D_j(\underline{\underline{\mathbf{R}}}) d^j_{\underline{\underline{\mathbf{R}}}}(\underline{\mathbf{r}}). \tag{3.21}$$

The electronic Hamiltonian may be represented by

$$\hat{H}_j = \hat{T}_e + \hat{V}_j(\underline{\mathbf{r}},\underline{\underline{\mathbf{R}}}), \tag{3.22}$$

where $\hat{V}_j(\underline{\mathbf{r}},\underline{\underline{\mathbf{R}}})$ is the electron-nuclear interaction that is different for every diabatic state. The way $\hat{V}_j(\underline{\mathbf{r}},\underline{\underline{\mathbf{R}}})$ is chosen is usually intuitive and based on our understanding of the system and the problem we are dealing with. On the other hand, the electron-nuclear coupling potential (3.7) of the exact electronic equation (3.4) together with $\hat{W}_{en}$ (2.10), provide a formally exact electron-nuclear interaction potential in the electronic equation. In this respect, $\hat{W}_{en} + \hat{U}^{coup,j}_{en}$ can be viewed as an exact concept of the electron-nuclear interaction, $\hat{V}_j(\underline{\mathbf{r}},\underline{\underline{\mathbf{R}}})$, of diabatic electronic Hamiltonian (3.22).

So far, we have discussed the concept of exact potential energy surfaces in two limits: (i) infinite nuclear mass (ii) nuclear mass equal to the electronic mass. We have shown that the exact potential energy surfaces in these two limits recover the concepts of: (i) *adiabatic* potential energy surfaces and (ii) *diabatic* potential energy surfaces. Therefore, the exact electronic equation (3.4) can be interpreted as a universal electronic equation that leads to the *adiabatic* and *diabatic* electronic equations in these limits. In figure (3.5) we plot the first exact potential energy surface of various nuclear masses between the

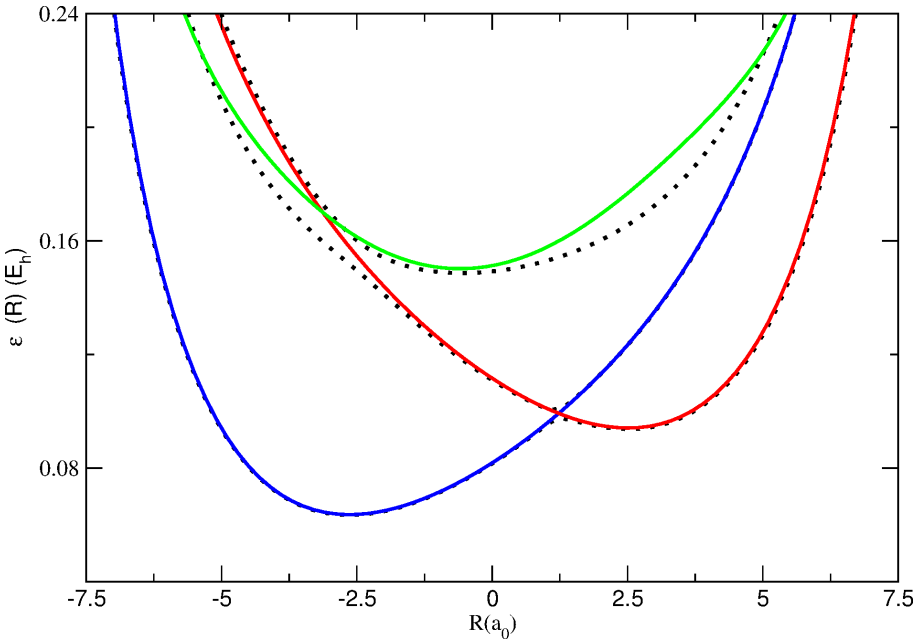

FIGURE 3.4: The first three exact potential energy surfaces of the system (see the text). The first three BOPESs are plotted for the reference.

limiting cases. As the nuclear density is very localized for the heavy nuclei, its value drops under the accuracy of the numerical calculations for the larger nuclear masses faster. Therefore, we cannot always give the exact potential energy surfaces for the whole R-space. That is why some of the potentials in figure (3.5) are trimmed. This figure (3.5) provides us with an instructive picture how the exact potential energy surface changes with the nuclear mass and swings between the two limits.

Another interesting concept to discuss in connection with the adiabatic and diabatic representation is the exact electronic conditional wave-function. In figure (3.6) the first three exact electronic densities are plotted together with the first three BO electronic densities. These two sets represent the two limits discussed before. The BO electronic densities undergo abrupt changes at the points of avoided crossings of the adiabatic potential. For example, the first BO state, $\phi_R^{BO,1}$, peaks at the position of the fixed ion on the left for $R < 1$ and for $R > 1$ the peak moves to the position of the fixed ion on the right while each of the first two exact electronic densities, $|\Phi_R^1|^2$ and $|\Phi_R^2|^2$, show only one major peak on the left and right fixed ions, respectively. In other words, the adiabatic states have mixed characters, i.e., the two minima of the adiabatic potential energy surface of the ground state, represent two different states of the system, each of which is described by its corresponding diabatic representation. The exact electronic

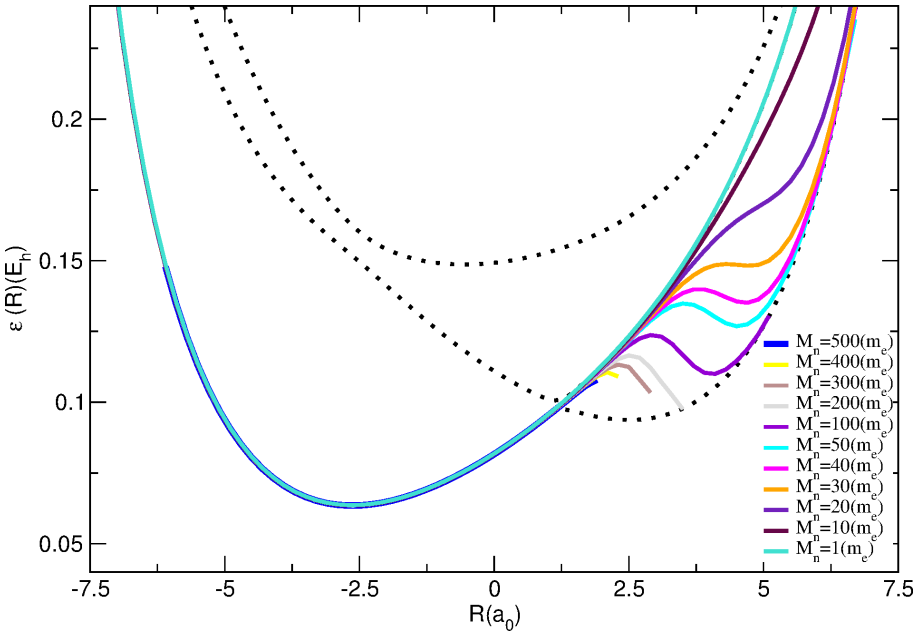

FIGURE 3.5: The exact potential energy surfaces of the molecular ground state for different nuclear masses (denoted on the plot). The first three BOPESs are plotted for the reference.

densities plotted in (3.6), like the exact potentials, are similar to the diabatic electronic densities. The diabatic states, similar to the exact electronic states discussed here, are obtained by assuming that in the Shin-Metiu Hamiltonian (3.15) the interaction of the electron with one of the fixed ions (on the right or left) is neglected (see the discussion by Shin and Metiu in [54]).

3.4 Strong Coupling II

The BOPESs provide an intuitive picture to analyse and interpret molecular processes. The conical intersections of the BOPESs are particularly important due to the crucial role they play in studying the molecular processes. There are two major issues in connection with these points: (i) Geometric phase: Geometric/Berry-Pancharatnam phases [55] are usually interpreted as arising from an approximate decoupling of a system from "the rest of the world", thereby making the system Hamiltonian dependent on some "environmental" parameters. For example, in the static BO approximation, the electronic Hamiltonian (2.3) depends parametrically on the nuclear positions; i.e., the stationary electronic Schrödinger equation is solved for each fixed nuclear configuration $\underline{\underline{\mathbf{R}}}$, (2.12) yielding $\underline{\underline{\mathbf{R}}}$-dependent eigenvalues (the BOPES) and eigenfunctions (the BO electronic

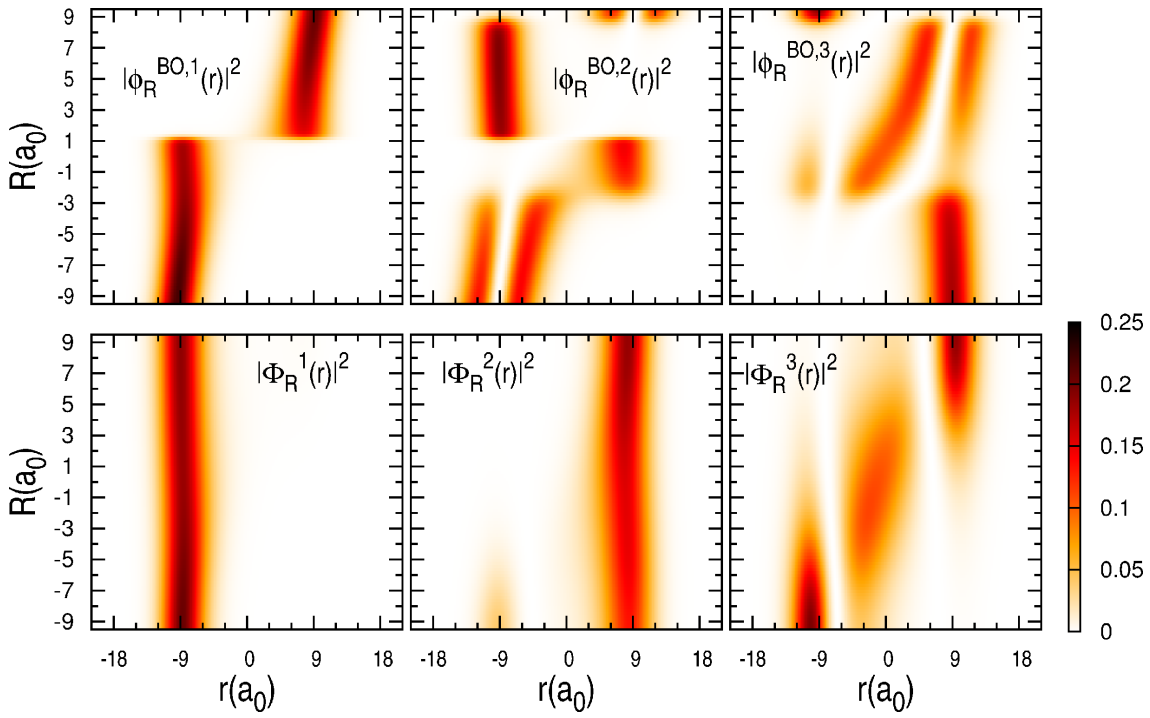

FIGURE 3.6: The first three exact conditional electronic densities (bottom) together with the first three BO conditional electronic densities (top) as denoted on the plots

wavefunctions). If the total molecular wavefunction is approximated by a single product of a BO electronic wavefunction and a nuclear wavefunction (see Sec. (2.1.1) for more details), the equation of motion of the latter contains a Berry-type vector potential. In this pure adiabatic description of the system, this vector potential cannot be gauged away in the presence of conical intersections. Because, in order to have a single valued electronic wavefunction, they cannot be chosen real. Hence, a vector potential enters the nuclear equation and leads to a Berry phase when traveling around the points of intersection. However, it is not yet clear if the appearance of Berry phases is a consequence of the BO approximation or it survives in the exact treatment. (ii) The conical intersections, also called funnels, due to their important role in providing the pathways for ultrafast interstate crossings and non-radiative relaxation from a molecular excited state to the ground state. However, it is a theoretical challenge to study the nuclear dynamics through these points due to the infinite non-adiabatic coupling between the electronic states at the point. A diabatic representation of the molecular wavefunction provides an alternative approach that has the interpretative features of the BOPESs and does not contain singular points of the conical intersections. The drawback, however, is that there are many choices and choosing a proper representation is very complicated .

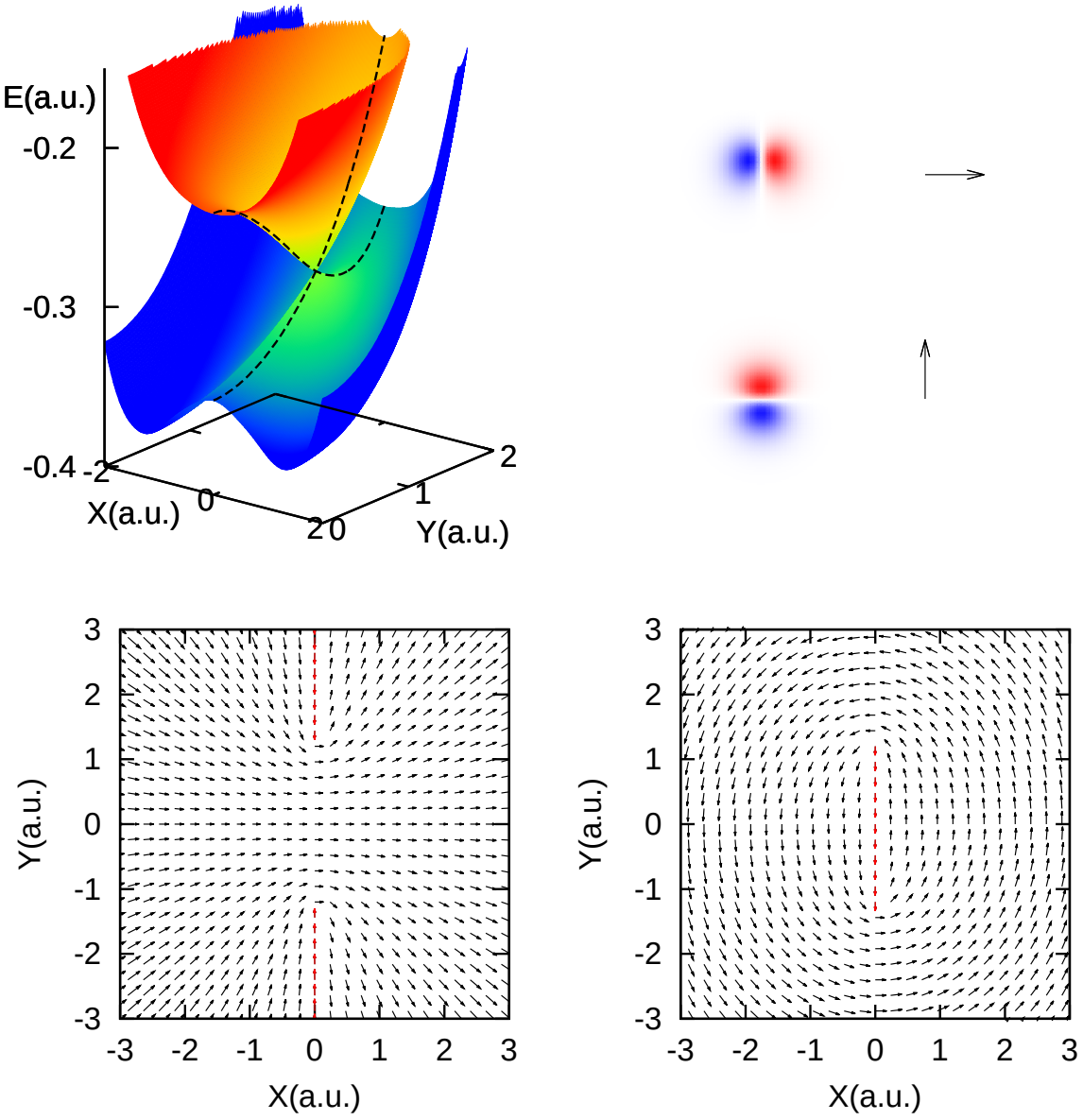

FIGURE 3.7: (top-left) The first (blueish) and second (reddish) excited BOPESs, (top-right) the arrow representation for p-orbital-like wavefunctions at a certain $\mathbf{R}$, and the BO electronic wavefunctions in the arrow representation for the first excited BO state (bottom-left) and the second excited BO state (bottom-right). A set of red arrows represents the discontinuity line for phase changes.

$N_R(x,y)$	$\Delta R\ (x,y)$	$\lvert R_{max}\rvert\ (x,y)$	$N_r\ (x,y)$	$\Delta r\ (x,y)$	$\lvert r_{max}\rvert\ (x,y)$
(101,101)	(0.12,0.12)	(6,6)	(81,81)	(0.3,0.3)	(12.0,12.0)

TABLE 3.2: Numerical parameters employed for the numerical calculation of the H_3^{2+} model .

In this section, we seek to shed light on the issues discussed above by studying the EPESs of a system that shows conical intersections in its BOPESs. To this end, we have developed a model system (see 3.2.3) that contains conical intersections between the second and third BOPESs when a, b, and R_0 are chosen as 0.5, 10.0, and 3.5, respectively.

For the numerical calculation we solve the time-independent Schrödinger equation (3.1) for the model of H_3^{2+} on real space grids using the parameters of the table (3.2). Note that we treat a system with four degrees of freedom that makes the calculations numerically challenging.

First, we investigate the BO states of this model Hamiltonian. The ground BO state $\phi_{\mathbf{R}}^{BO,1}$ shows a s-like wavefunction without any nodes while the first excited BO state $\phi_{\mathbf{R}}^{BO,2}$ and the second excited BO state $\phi_{\mathbf{R}}^{BO,3}$ show p-like wavefunction with a single nodal line. Since all the three ions have the same interaction potentials (3.18), there is symmetry-induced degeneracies between $\phi_{\mathbf{R}}^{BO,2}$ and $\phi_{\mathbf{R}}^{BO,3}$ at the equilateral positions, $\mathbf{R}_{\pm}^{CI} = (0, \pm Y_{CI})$, where $Y_{CI} = 1.2$. The BOPESs for the first and second excited electronic states ϵ_{BO}^2 and ϵ_{BO}^3, and the corresponding "real-valued" electronic BO wavefunctions, $\phi_{\mathbf{R}}^{BO,2}$ and $\phi_{\mathbf{R}}^{BO,3}$, are depicted in Fig. (3.7). The p-orbital-like shape of the electronic wavefunctions for each nuclear position $\mathbf{R}$ motivates us to represent the electronic wavefunction as flow of vectors. The direction of each vector at $\mathbf{R}$ is given by $\int \boldsymbol{r}\phi_{\mathbf{R}}^{BO,j}(\boldsymbol{r})d\boldsymbol{r}$ which is the direction of the phase of p-orbital-like wavefunction. Here, the phases of both $\phi_{\mathbf{R}}^{BO,2}$ and $\phi_{\mathbf{R}}^{BO,3}$ are discontinuous (Fig. 3.7). These discontinuities persist as long as we insist to have real electronic wavefunctions and one can only move the position of the discontinuities by multiplying the BO electronic wavefunctions by a phase factor. We choose the phase of the BO electronic wavefunctions such that the discontinuities appear at the lines L_1 and L_2 for $\phi_{\mathbf{R}}^{BO,2}$ and $\phi_{\mathbf{R}}^{BO,3}$, respectively, where $L_1 = \{(X,Y)|X = 0, |Y| > Y_{CI}\}$ and $L_2 = \{(X,Y)|X = 0, |Y| < Y_{CI}\}$. Hence, the conical intersections exist at $\mathbf{R}_{\pm}^{CI}$ between the two states.

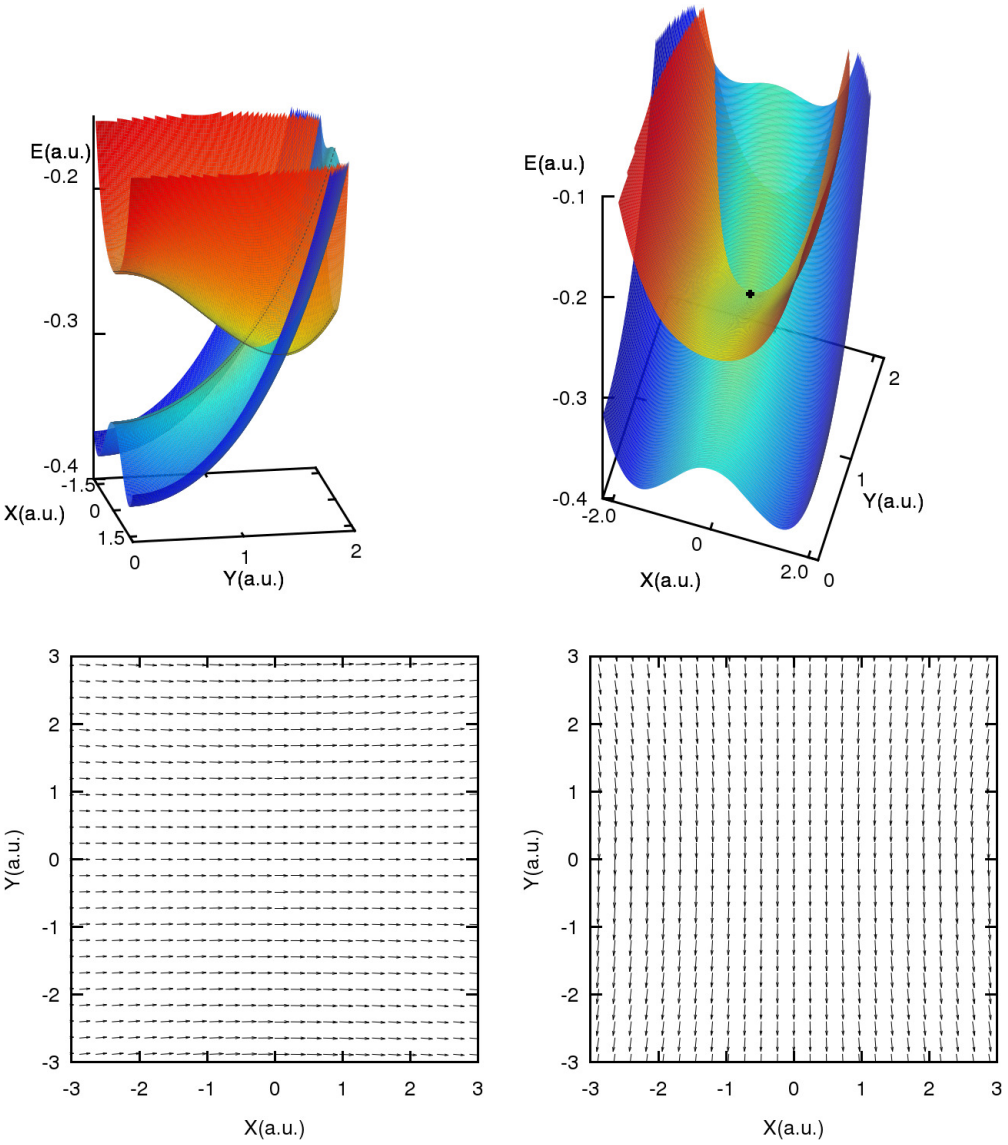

FIGURE 3.8: Exact potential energy surfaces ϵ_A^{exact} (Blue) and ϵ_B^{exact} (Red) for $M_n = m_e$ and according to the total molecular energies: $E_A = -0.0122E_h$ and $E_B = 0.0498E_h$ (top) and the corresponding electronic wavefunctions, $\Phi_{\mathbf{R}}^A$ (bottom, left) and $\Phi_{\mathbf{R}}^B$ (bottom, right) .

Now, we look at the exact calculations. In order to study the EPESs in the diabatic limit, we choose the nuclear mass equal to the electronic mass, $M = m_e$. Then, we calculate the exact states (3.1) which are eigenfunctions of the full Hamiltonian (3.18). We look at the exact states in the energy range above the minima of the lower state. Here we study two of them, $\Psi^{A,B}$, that yield the exact nuclear wavefunctions, $\chi^{A,B}(\mathbf{R})$, that similar to the lowest vibrational states of the two BOPESs exhibit no node. The corresponding exact energies are $E_A = -0.0122E_h$ and $E_B = 0.0498E_h$. The exact nuclear wavefunctions, $\chi^{A,B}(\mathbf{R})$, are plotted in Fig. (3.9), and the corresponding electronic wavefunctions, $\Phi^{A,B}_{\mathbf{R}}$, are shown at the bottom of Fig. (3.8). The real-valued exact electronic wavefunctions, $\Phi^{A,B}_{\mathbf{R}}$, contrary to their BO counterparts, are smooth and their phases change continuously. In particular, along the Y-axis they go smoothly through the degenerate points of the BO potentials. Here, we should mention that the $\chi^{A,B}(\mathbf{R})$ are non zero at the position of the BO conical intersections. In Fig. (3.8) (top), the EPESs, $\epsilon^{exact}_{A,B}(\mathbf{R})$, corresponding to the exact molecular states, $\Psi^{A,B}$, and the point of conical intersection is indicated by a dot. The exact surfaces, similar to the 1D system discussed in Sec. (3.3), behave similar to the diabatic potential energy surfaces, have the shape of one of the BO surfaces in one side of conical intersections, pass smoothly through the conical intersections and follow the shape of the other BO surface. On the other hand, the vector potential is zero here, because the exact electronic wavefunctions are smooth and real-valued. Hence, while in the adiabatic description of the system, a Berry phase appears, in the exact treatment, within the exact factorization framework, no Berry phase appears.

We conclude the discussion over the EPESs by recalling the discussion of the previous section (2.3.1) about the exact time-dependent vector potential. the exact vector potential, in the static case as well, can be expressed in terms of the full molecular state, Ψ^K, and the phase of the corresponding nuclear wavefunction:

$$\mathbf{A}^K_\alpha(\underline{\underline{\mathbf{R}}}) = \frac{\Im\left\langle \Psi^K \middle| \nabla_\alpha \Psi^K \right\rangle_{\underline{\underline{\mathbf{r}}}}}{|\chi^K(\underline{\underline{\mathbf{R}}})|^2} - \nabla_\alpha S^K(\underline{\underline{\mathbf{R}}}), \tag{3.23}$$

where, $\chi^K(\underline{\underline{\mathbf{R}}}) = e^{iS^K}(\underline{\underline{\mathbf{R}}})|\chi^K(\underline{\underline{\mathbf{R}}})|$. From the equation (3.23) on can actually extract the conditions under which the vector potential cannot be gauged away. One condition would be when a molecular state is current-carrying. Then, due to the degeneracy, the full molecular state is complex. The other condition is when the phase, $S(\underline{\underline{\mathbf{R}}})$, is not smooth, that happens in situations such as the existence of the conical intersections in

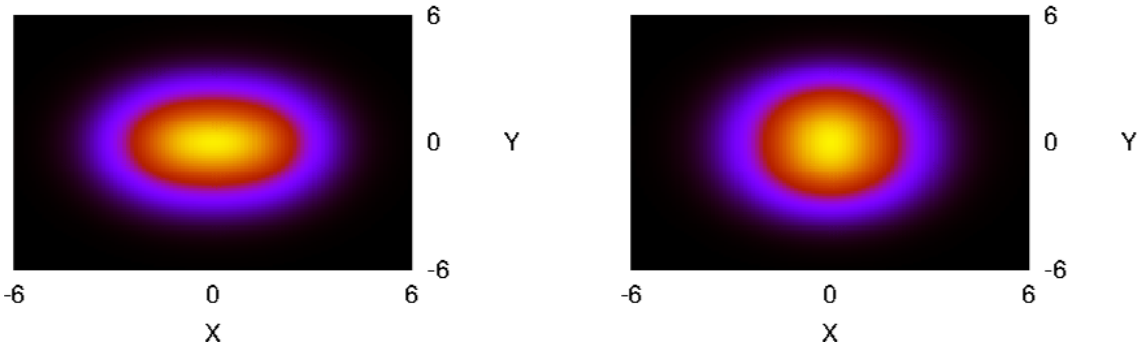

FIGURE 3.9: Exact nuclear densities, $|\chi_A|^2$ (left) and $|\chi_B|^2$ (right), corresponding to total energies: $E_A = -0.0122E_h$ and $E_B = 0.0498E_h$

the BO framework. However, we have seen at least one example that shows that the exact electronic wavefunctions are real-valued and smooth when the adiabatic states are not. Our observations, might be insufficient to conclude that the conical intersections and the Berry phases associated to them, are artifacts of the BO approximation but they certainly are in support of the statement. Our results, furthermore, support the implementation of the diabatic surfaces to study molecular processes. The exact electron-nuclear coupling operator (3.7) in the exact electronic equation (3.4), together with the electron-nuclear Coulomb interaction potential, provide a rigorous form of the diabatic electron-nuclear interaction potential that can be a good starting point to develop approximations.

Chapter 4

Exact time-dependent potential energy surface

In Chapter (2) we have presented a detailed description of the exact factorization of the full time-dependent electron-nuclear wavefunction. A full derivation of the equations that govern the electronic and nuclear motion was provided. We have shown that the concepts of an exact time-dependent potential energy surface and an exact time-dependent vector potential emerge naturally from the formalism. This representation of the correlated electron-nuclear many-body problem is exciting as the wavefunction $\chi(\underline{\underline{\mathbf{R}}},t)$ that satisfies the exact nuclear equation of motion (2.30) leads to a nuclear N-body density, $\Gamma(\underline{\underline{\mathbf{R}}},t) = |\chi(\underline{\underline{\mathbf{R}}},t)|^2$, and a nuclear N-body current density, $\mathbf{J}_\nu(\underline{\underline{\mathbf{R}}},t) = \Im(\chi^*\nabla_\nu\chi) + \Gamma(\underline{\underline{\mathbf{R}}},t)\mathbf{A}_\nu$, which reproduce the true nuclear N-body density and current density obtained from the full wave-function, $\Psi(\underline{\mathbf{r}},\underline{\underline{\mathbf{R}}},t)$ [56]. In this sense, $\chi(\underline{\underline{\mathbf{R}}},t)$, can be viewed as the proper nuclear wave-function. The time evolution of $\chi(\underline{\underline{\mathbf{R}}},t)$, on the other hand, is completely determined by the TDPES, $\epsilon(\underline{\underline{\mathbf{R}}},t)$, and the vector potential, $\mathbf{A}_\nu(\underline{\underline{\mathbf{R}}},t)$. Moreover, these potentials are *unique* up to within a gauge transformation. This uniqueness is straightforwardly proven by following the steps of the current-density version [57] of the Runge-Gross theorem [58]. In other words, if one wants a TDSE (2.30) whose solution, $\chi(\underline{\underline{\mathbf{R}}},t)$, yields the true nuclear N-body density and current density of the complete system, then the potentials appearing in this TDSE are (up to within a gauge transformation) uniquely given by Eqs. (2.33-2.34); there is no other choice. In particular, when the time-dependent vector potential can be gauged away by a proper gauge-transformation, the TDPES uniquely describes the nuclear dynamics and provides us with an alternative way of visualizing and interpreting

the non-adiabatic processes. Studying the molecular process using a *single* TDPES is particularly relevant if one thinks of a classical or semi-classical treatment of the nuclei where a well-defined single classical force would be highly desirable.

In this chapter, we study and analyze the TDPES of the exactly solvable systems in various situations, in particular, in comparison with the BOPESs. We first discuss the details of the calculations. Then, we investigate the generic features of the exact TDPES *without* external laser but in the presence of strong non-adiabatic couplings, using the of the Shin-Metiu model (3.2.2). A major result will be that the exact TDPES exhibits nearly discontinuous steps connecting different static BOPES, reminiscent of Tully's surface hopping [6] in the classical limit. At the end, we present the features of the exact TDPES in the presence of strong laser fields for the H_2^+ molecular ion (3.2.1) that proves to be a useful interpretive tool to identify different mechanisms of dissociation.

4.1 Details of the calculations

In this section, we present the numerical procedure that leads to the calculation of the TDPES. In order to calculate the TDPES one needs to have access to the electronic wave-function, $\Phi_{\underline{\underline{\mathbf{R}}}}(\underline{\mathbf{r}}, t)$, and the nuclear wavefunction, $\chi(\underline{\underline{\mathbf{R}}}, t)$, at every instant of time. As in the systems that are studied in this chapter, there is only one electronic degree of freedom and one nuclear degree of freedom, from now on the symbols $\underline{\mathbf{r}}$ and $\underline{\underline{\mathbf{R}}}$ are replaced by r (or x) and R. To obtain $\Phi_R(r,t)$ and $\chi(R,t)$, we do not solve the Eqs. (2.29-2.30), Instead, we calculate them through, $\Psi(r,R,t)$, the solution of the TDSE (2.11) of the complete system. Starting from an initial state, we propagate the TDSE numerically, using the second-order split-operator method [59], to obtain the full molecular wavefunction $\Psi(\underline{\mathbf{r}}, \underline{\underline{\mathbf{R}}}, t)$. As there is only one nuclear degree of freedom, in the systems that are studied in this chapter, we can fix the gauge in Eqs. (2.46)-(2.47) such that the vector potential (2.34) vanishes identically. For one-dimentional problems this is always possible with the choice:

$$\frac{d}{dR}S(R,t) = \frac{\Im \int dr \Psi^*(r,R,t)\frac{d\Psi(r,R,t)}{dR}}{|\chi(R,t)|^2}. \tag{4.1}$$

So we can calculate $S(R,t)$, the phase of the nuclear wavefunction, as well as

$$|\chi(R,t)|^2 = \int dx |\Psi(r,R,t)|^2,$$

the nuclear density, from the computed exact time-dependent molecular wavefunction. Being equipped with the nuclear wave-function, $\chi(R,t)$ $(= |\chi(R,t)|e^{iS(R,t)})$, we then compute the TDPES by inverting the nuclear equation of motion (2.30). Alternatively, we may calculate the electronic wave-function,

$$\Phi_R(r,t) = \frac{\Psi(r,R,t)}{\chi(R,t)},$$

and obtain the TDPES from[1] (2.33).

4.2 Steps in the exact time-dependent potential energy surface

In this section, we present a detailed study of the TDPES in the situations where electronic and nuclear motions are strongly coupled. As discussed in the previous section (4.1), in order to obtain the TDPES, the full electron-nuclear wave-function has to be calculated. Therefore, we need to choose a system that is simple enough to allow for a numerically exact treatment and that nevertheless exhibits characteristic features associated with the non-adiabatic dynamics. Here, we employ the Shin-Metiu model (3.2.2).

In the gauge (4.1) that we have implemented to perform the calculations, the TDPES alone determines the time evolution of $\chi(R,t)$. In order to investigate the TDPES in detail, we may study its gauge-invariant (GI) and gauge-dependent (GD) constituents separately [2],

$$\epsilon(R,t) = \epsilon_{GI}(R,t) + \epsilon_{GD}(R,t), \tag{4.2}$$

where

$$\epsilon_{GI}(R,t) = \langle\Phi_R(t)|\,\hat{H}_{BO}\,|\Phi_R(t)\rangle_r + \frac{\hbar^2}{2M}\,\langle\nabla_R\Phi_R(t)|\nabla_R\Phi_R(t)\rangle_r - \frac{\mathbf{A}^2(R,t)}{2M}, \tag{4.3}$$

and

$$\epsilon_{GD}(R,t) = \langle\Phi_R(t)|\,-i\hbar\partial_t\,|\Phi_R(t)\rangle_r\,. \tag{4.4}$$

In arriving at Eqs. (4.3-4.4), we have used the representation (2.67) of $\epsilon(R,t)$. The GI part of the TDPES, ϵ_{GI}, is not affected by the gauge transformation (2.47). The GD part, on the other hand, varies from gauge to gauge. They both have important features

[1] In this thesis we have mainly followed the former procedure. The later procedure has been used in some cases to check.

[2] It can be easily proved that $\tilde{\epsilon}_{GI}(\underline{\underline{\mathbf{R}}},t) = \epsilon_{GI}(\underline{\underline{\mathbf{R}}},t)$ and $\tilde{\epsilon}_{GD}(\underline{\underline{\mathbf{R}}},t) = \epsilon_{GD}(\underline{\underline{\mathbf{R}}},t) + \partial_t\theta(\underline{\underline{\mathbf{R}}},t)$ under the transformations in Eqs. (2.47).

N_R	ΔR (a_0)	R_{max} (a_0)	N_r	Δr (a_0)	$\lvert r_{max}\rvert$ (a_0)	Δt $(a.u.)$
381	0.025	9.5	512	0.4	102.2	0.05

TABLE 4.1: Numerical parameters employed for the numerical simulations of the time-evolution of the Metiu-Shin model.

that will be discussed and analyzed in the following section. In order to analyze the TDPES, we use the BO electronic states, $\{\phi_R^{(l)}(r)\}_{l=1,\ldots}$, and BOPESs, $\epsilon_{BO}^{(l)}(\underline{\underline{\mathbf{R}}})$, which are the eigenstates and eigenvalues of the BO electronic Hamiltonian (2.3), respectively (for more details see the discussion of the section (2.1.1)). If the full wave-function, $\Psi(\underline{\mathbf{r}}, \underline{\underline{\mathbf{R}}}, t)$, is expanded in this basis (2.1.2),

$$\Psi(\underline{\mathbf{r}}, \underline{\underline{\mathbf{R}}}, t) = \sum_l F_l(\underline{\underline{\mathbf{R}}}, t)\phi_{\underline{\underline{\mathbf{R}}}}^{(l)}(\underline{\mathbf{r}}), \tag{4.5}$$

then the nuclear density maybe written as

$$\left|\chi(\underline{\underline{\mathbf{R}}}, t)\right| = \sqrt{\sum_l \left|F_l(\underline{\underline{\mathbf{R}}}, t)\right|^2}. \tag{4.6}$$

This is obtained by integrating the squared modulus of Eq. (4.5) over the electronic coordinates with normalized adiabatic states. The exact electronic wave-function may also be expanded in terms of the BO states (2.63),

$$\Phi_{\underline{\underline{\mathbf{R}}}}(\underline{\mathbf{r}}, t) = \sum_l C_l(\underline{\underline{\mathbf{R}}}, t)\phi_{\underline{\underline{\mathbf{R}}}}^{(l)}(\underline{\mathbf{r}}). \tag{4.7}$$

The expansion coefficients of Eqs. (4.5) and (4.7) are related,

$$F_l(\underline{\underline{\mathbf{R}}}, t) = C_l(\underline{\underline{\mathbf{R}}}, t)\chi(\underline{\underline{\mathbf{R}}}, t), \tag{4.8}$$

by virtue of the factorization (2.24). The PNC then reads

$$\sum_l \left|C_l(\underline{\underline{\mathbf{R}}}, t)\right|^2 = 1, \quad \forall\ \underline{\underline{\mathbf{R}}}, t. \tag{4.9}$$

In all the cases, studied in the following sections, the initial wave-function is the product of a real normalized Gaussian wave-packet, centered at $R_c = -4.0\ a_0$ with the variance $\sigma = 1/\sqrt{2.85}$ (black line in Fig. 4.1), and the second BO electronic state, $\phi_R^2(r)$, i.e.,

$$\Psi_{initial} = \frac{1}{\sigma\sqrt{2\pi}} e^{\frac{-(R+4)}{2\sigma^2}} \phi_R^{(2)}(r). \tag{4.10}$$

To achieve the desirable numerical accuracy, we have repeated the same calculations with differens box sizes and grid-spacing. Table (4.1) gives a set of parameters that provid an efficient convergence. For calculating the NACs for the classical calculations of section (4.2.4), we have used more grid points along the nuclear axis ($N_R = 1000$).

4.2.1 Strong non-adiabatic coupling

We first study a case in which the electronic and nuclear motions are strongly coupled. In order to produce that situation, we choose the parameters of the Hamiltonian (3.15) as $R_f = 5.0\ a_0$, $R_l = 3.1\ a_0$ and $R_r = 4.0\ a_0$ such that the first BOPES, $\epsilon_{BO}^{(1)}$, is strongly coupled to the second BOPES, $\epsilon_{BO}^{(2)}$, around the avoided crossing at $R_{ac} = -1.90\ a_0$ and there is a weak coupling to the rest of the surfaces. The four lowest BOPESs for this set of parameters are shown in Fig. 4.1 (left panel), along with the initial nuclear density. The same figure (right panel) presents the time-evolution of the populations of the BO states,

$$\rho_l(t) = \int d\underline{\underline{\mathbf{R}}} \left| F_l(\underline{\underline{\mathbf{R}}}, t) \right|^2 , \tag{4.11}$$

and underlines the strong non-adiabatic character of the system with the intense population exchange taking place at the passage through the avoided crossing ($t \simeq 12\ fs$).

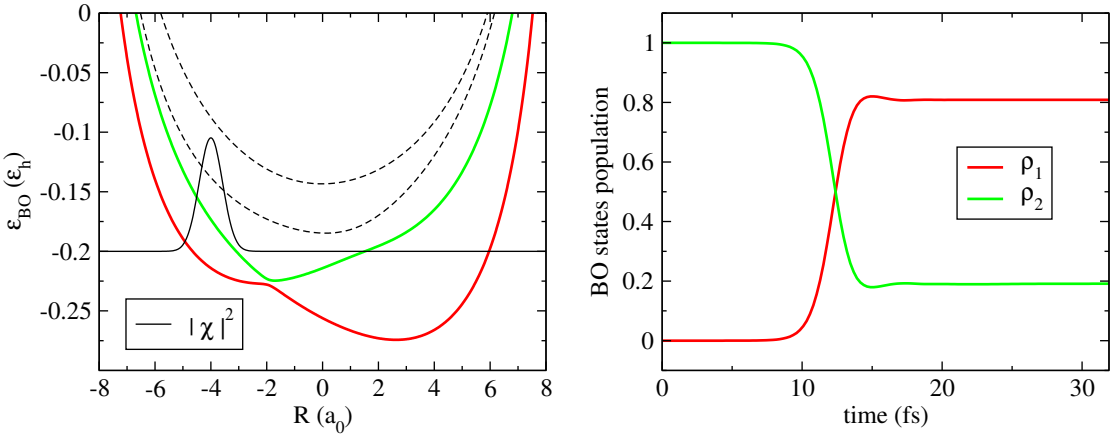

FIGURE 4.1: Left: lowest four BO surfaces, as functions of the nuclear coordinate. The first (red line) and second (green line) surfaces will be considered in the actual calculations that follow, the third and forth (dashed black lines) are shown as reference. The squared modulus (reduced by ten times and rigidly shifted in order to superimpose it on the energy curves) of the initial nuclear wave-packet is also shown (black line). Right: populations of the BO states along the time evolution. The strong non-adiabatic nature of the model is underlined by the population exchange at the crossing of the coupling region.

The GI part of the TDPES (4.3) shows, in general, two distinct features: (i) in the vicinity of the avoided crossing, as the nuclear wave-packet passes through a region of non-adiabatic coupling between different BOPESs, $\epsilon_{GI}(R,t)$ resembles the *diabatic* surface that smoothly connects the two adiabatic surfaces; (ii) far from the avoided crossing, it presents *dynamical steps* between regions in R-space where it is on top of one or the other BOPES. The GD part of the TDPES (4.4), on the other hand, is a piecewise constant function of the nuclear coordinate. This is illustrated in detail in Fig. 4.2 that contains the GI part of the TDPES (upper panel), the GD part of the TDPES (middle panel) and the nuclear density together with $|F_1|^2$ and $|F_2|^2$ (lower pannel) for three different snapshots of times. In all the plots, the regions highlighted within the boxes are the regions which we refer to in the following discussion. Outside such regions, the value of the nuclear density drops under the numerical accuracy of the calculations and the resulting potentials are not meaningful. That is why the TDPES are trimmed. The left panels show, at the initial time, (top) the GI part of the TDPES (black dots), with the two lowest BOPESs ($\epsilon^{(1)}_{BO}(R)$, dashed red line, and $\epsilon^{(2)}_{BO}(R)$, dashed green line) as reference, (center) the GD part of the exact potential (dark-green dots) which is a costant function of R and is set to be the zero of the GD potentials[3] and (bottom) the nuclear density (dashed black line) and its components on the BO states (4.6), $|F_1(R,t)|^2$ (red line) and $|F_2(R,t)|^2$ (green line). At time $t = 0\ fs$, the electronic wave-function, $\Phi_R(r,t)$, coincides with the second adiabatic state $\phi^{(2)}_R(r)$, therefore the GI component of the TDPES is identical with $\epsilon^{(2)}_{BO}(R)$, apart from a slight deviation due to the second term in Eq. (4.3). This is easily confirmed by the expression of $\epsilon_{GI}(R,t)$ in terms of the BO states and energies

$$\begin{aligned}\epsilon_{GI}(R,t) &= \sum_l |C_l(R,t)|\epsilon^{(l)}_{BO}(R) \\ &+ \frac{1}{2M}\Big[\sum_l |\nabla_R C_l|^2 + \sum_{lj} C^*_l C_j \left(i\nabla_R \cdot \mathcal{F}^{BO}_{lj} - \mathcal{G}^{BO}_{lj}\right) - 2\sum_{lj} \Im\big(C_j \nabla_\alpha C^*_l \mathcal{F}^{BO}_{lj,\alpha}\big)\Big]\end{aligned} \tag{4.13}$$

The leading term in Eq. (4.13) is the average of the BOPESs weighted by $|C_l(R,t)|^2$,

[3] The GD of the TDPES depends on the phase of the electronic wave-function, as can be proved by using the PNC in the second term on r.h.s of the expression

$$\epsilon_{GD}(R,t) = \int dr\, |\Phi_R(r,t)|^2\, \dot{\gamma}_R(r,t) - \frac{i}{2}\partial_t \int dr\, |\Phi_R(r,t)|^2\,. \tag{4.12}$$

Here, the symbol $\dot{\gamma}_R(r,t)$ has been used to indicate the time-derivative of the phase of the electronic wave-function.

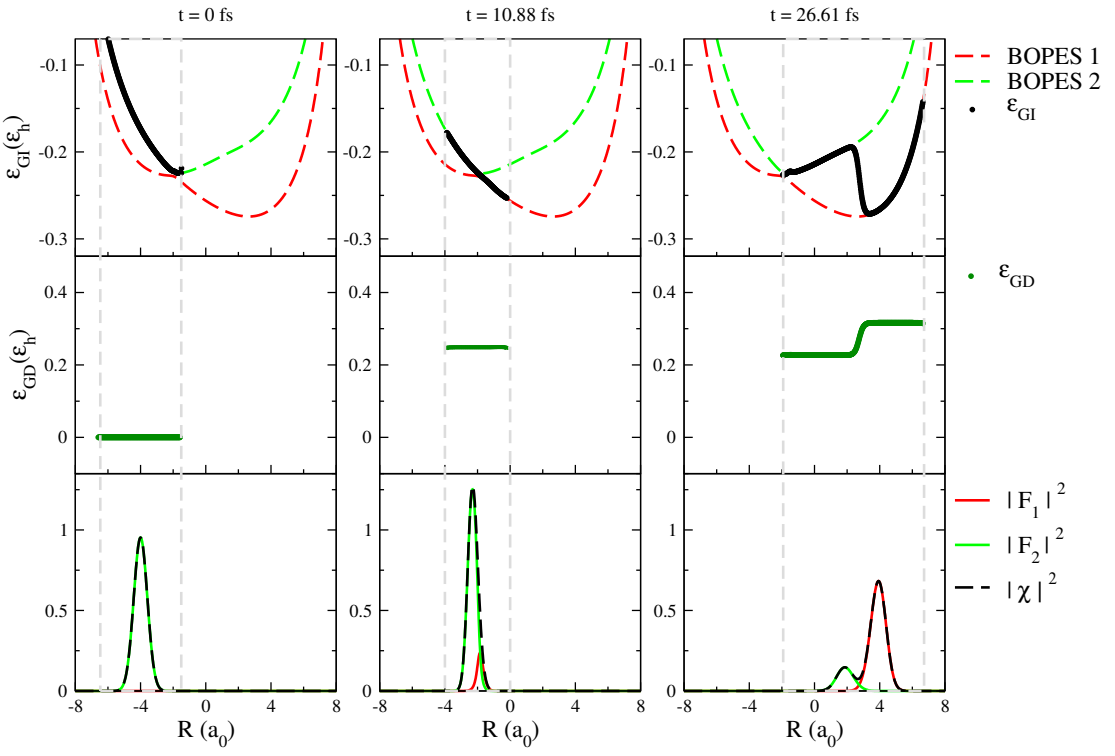

FIGURE 4.2: TDPES and nuclear densities at different time-steps, namely $t = 0\ fs$, $t = 10.88\ fs$ and $t = 26.61\ fs$. The different panels show: (top) GI part of the TDPES (black dots) and the two lowest BOPESs (first, dashed red line, and second, dashed green line) as reference; (center) the GD part of the TDPES (green dots); (bottom) nuclear density (dashed black line) and $|F_l(R,t)|^2$ ($l = 1$ red line and $l = 2$ green line). The gray boxes define the regions in R-space where the energies have been calculated, since the nuclear density is (numerically) not zero.

since the second term is $\mathcal{O}(M^{-1})$. The GD component of the TDPES in Eq. (4.4), in terms of the BO states, becomes

$$\epsilon_{GD}(R,t) = \sum_l |C_l(R,t)|^2\, \dot{\gamma}_l(R,t) \tag{4.14}$$

where $\dot{\gamma}_l(R,t)$ is the time-derivative of the phase of the coefficients $C_l(R,t)$ ($C_l(R,t) = e^{i\gamma_l(R,t)}|C_l(R,t)|$). The nuclear density, along with its components on the BO states from Eq. (4.6), is presented in Fig. 4.2. At the initial time, $|\chi(R,t)|^2 = |F_2(R,t)|^2$.

At $t = 10.88\ fs$ in Fig. 4.2 (central panels), (top) the GI part of the TDPES resembles the diabatic surface [54] that smoothly passes through the avoided crossing. This behavior allows the nuclear density moving on the upper BOPES to be partially "transferred" to the lower state, as the consistent increase of the population of state $\phi_R^{(1)}(r)$ (red curve in the bottom plot in Fig. 4.2) confirms. In region highlighted by the dashed box, the GD part of the exact potential is constant, therefore, it does not affect the nuclear dynamics.

At later times ($t = 26.61\ fs$ shown in the right panels of Fig. 4.2), when the nuclear wave-packet has split at the avoided crossing, both components of the TDPES present a pronounced stepwise behavior: the GI part follows one or the other BOPES in different regions of R-space that are connected by a step, whereas the GD part is stepwise constant, with steps appearing in the same region.

The generic features of the TDPES are formed by bringing together the features of the GI and GD part of it. The shape of the TDPES, at the initial times, is formed by the GI part and the effect of the GD part is not more than a constant shift of the overall potential. Hence, The TDPES that drives the nuclear dynamics, behaves like a diabatic surface and "opens" in the direction of the wave-packet's motion in order to facilitate the population exchange between the adiabatic states. After the wave-packet splits at the avoided crossing, in different regions in R-space, the TDPES is parallel to one or the other BOPES and a step forms in the interface.

The exact TDPES represented in Fig. 4.2 can be viewed from a different perspective. The nuclear wave-packet from a semi-classical point of view can be represented as an ensemble of classical trajectories, along which point-particles evolve under the action of a classical force which is the gradient of ϵ_{GI}. According to our observations, on different sides of a step such a force is calculated from different BOPESs. This is reminiscent of the *jumping between the adiabatic surfaces* in algorithms such as Tully's surface hopping [60, 61] (TSH). However, while Tully surface hopping is a stochastic algorithm, the jumps in the exact TDPES correspond to an exact solution of the TDSE. When the time-dependent vector potential cannot be set to zero, a gauge can be chosen in which ϵ_{GD} is zero and a time-dependent vector potential together with ϵ_{GI} specifies the classical force that the nuclei experience in different slices of R-space. The success of these algorithms in reproducing non-adiabatic processes becomes clear in the light of the fact that the exact TDPES itself is parallel to different BOPESs in different regions along the nuclear coordinate. The usually abrupt transitions between the adiabatic surfaces, i.e., the steps in the exact treatment, is analogous with the stochastic jumps between BO surfaces in the TSH.

4.2.2 Analysis of the steps

The behavior of the GI part of the TDPES is mainly determined by the first term in Eq. (4.13). The steps appear in the region around R_0, the cross-over of $|F_1(R,t))|^2$ and $|F_2(R,t))|^2$. In particular, at this point $|F_1(R_0,t)|^2 = |F_2(R_0,t)|^2 = |X(t)|$ and, irrespective of this value, the expansion coefficients in the electronic wave-function (4.7) have the value $|C_1(R_0,t)|^2 = |C_2(R_0,t)|^2 = 1/2$. This relation holds as a consequence of Eq. (4.8), which can be written as

$$|C_l(R_0,t)|^2 = \frac{|F_l(R_0,t)|^2}{|F_1(R_0,t)|^2 + |F_2(R_0,t)|^2} = \frac{1}{2} \quad \text{with} \quad l = 1,2, \tag{4.15}$$

and is clearly shown in Fig. 4.3. Here we present, in the upper panel, the GI part (black line) and the GD part (blue line, rigidly shifted along the energy axis) of the exact potential at time $t = 26.62\ fs$. The BO surfaces (dashed red and green lines) are also plotted as reference. In the lower panel, we plot the coefficients of the expansions in Eq. (4.5) (dashed red and green lines) and in Eq. (4.7) (continuous red and green lines). The continuous black line represents the nuclear density.

The expression of the GI component of the TDPES for a two-state system, from Eq. (4.13) neglecting terms $\mathcal{O}(M^{-1})$, is

$$\epsilon_{GI}(R,t) = |C_1(R,t)|^2\, \epsilon^{(1)}_{BO}(R) + |C_2(R,t)|^2\, \epsilon^{(2)}_{BO}(R). \tag{4.16}$$

If $|C_l(R,t)|^2$ is Taylor-expanded around R_0, up to within the linear deviations,

$$\begin{aligned} \left|C_{\frac{1}{2}}(R,t)\right|^2 &= \left.\frac{\left|F_{\frac{1}{2}}(R,t)\right|^2}{|\chi(R,t)|^2}\right|_{R_0} + \nabla_R \left.\frac{\left|F_{\frac{1}{2}}(R,t)\right|^2}{|\chi(R,t)|^2}\right|_{R_0} (R - R_0) \\ &= \frac{1}{2} \pm \frac{\alpha(t)}{2}\,(R - R_0)\,, \end{aligned} \tag{4.17}$$

one can identify the parameter $\alpha(t)$, defined as

$$\alpha(t) = \frac{(\nabla_R\,|F_1(R,t)|)_{R_0} - (\nabla_R\,|F_2(R,t)|)_{R_0}}{|X(t)|}. \tag{4.18}$$

Where $\alpha(t)$ is the slope of the coefficients in the step region from that the width of the region can be determined. Using the relation, $0 \leq \left|C_{\frac{1}{2}}(R,t)\right|^2 \leq 1$, we get

$$0 \leq \frac{1}{2} + \frac{\alpha(t)}{2}\,(R - R_0) \leq 1 \quad \text{with} \quad \frac{\Delta R}{2} = |R - R_0| \leq \frac{1}{\alpha(t)}. \tag{4.19}$$

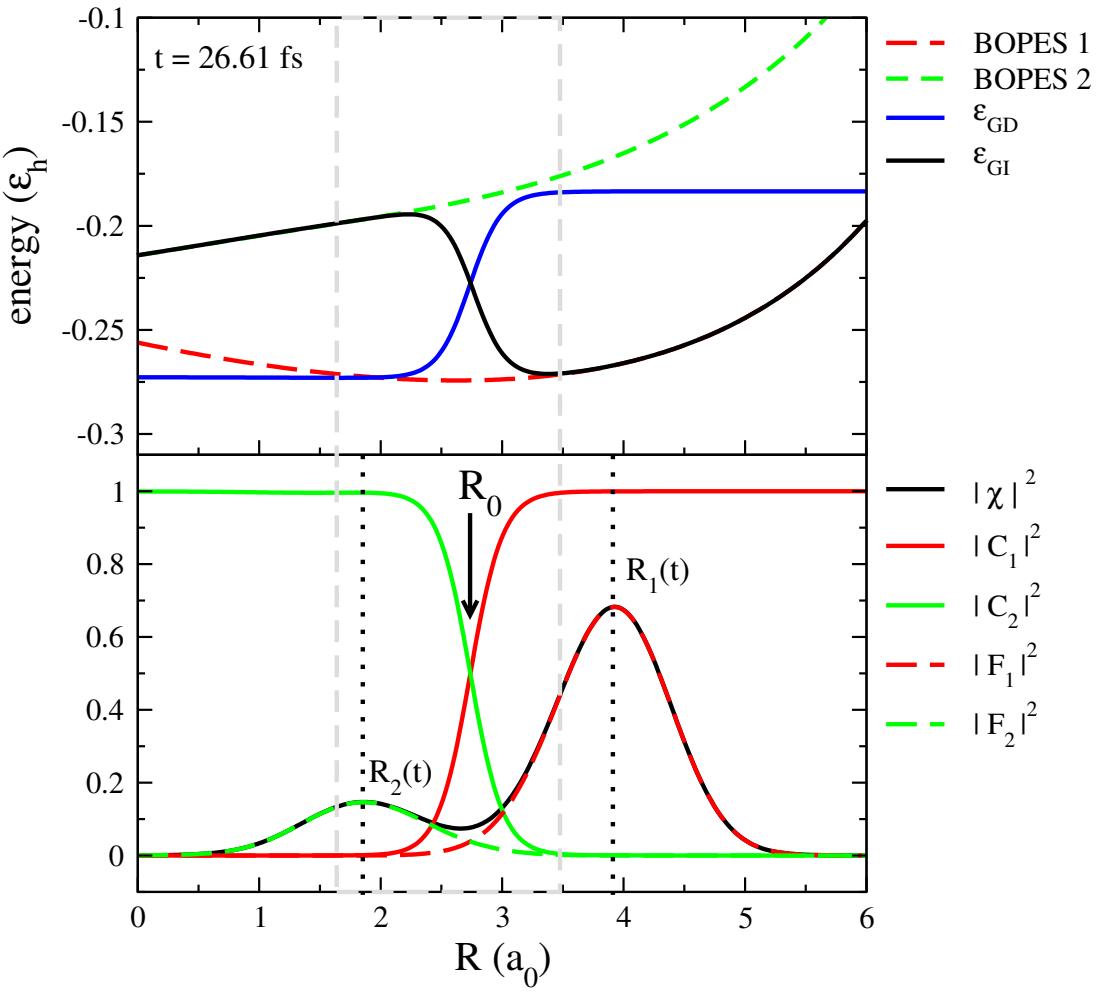

FIGURE 4.3: Top: GI part (black line) and the GD part (blue line, rigidly shifted along the energy axis) of the exact potential at time $t = 26.61\ fs$. The first (dashed red) and second (dashed green) BOPESs are shown as reference. Bottom: coefficients $|F_l(R,t)|^2$ of the expansion of the full wave-function (Eq. (4.5)) on the BO states ($l = 1$ dashed red line, $l = 2$ dashed green line) and coefficients $|C_l(R,t)|^2$ of the expansion of the electronic wave-function ($l = 1$ continuous red line, $l = 2$ continuous green line); the black line represents the nuclear density. R_0 is the position where the coefficients $|F_1(R,t)|^2$ and $|F_2(R,t)|^2$ have the same value and the dashed box highlights the region of the step.

Therefore, ΔR is small because the step is steep, as consequence of a large $\alpha(t)$. $\alpha(t)$ can be large either because $|X(t)|$ is small, i.e., the cross-over is located in a region of small nuclear density, or because the terms in the numerator of Eq. (4.18) have opposite slopes at R_0 (this is the case depicted in Fig. 4.3). Outside the region ΔR, one or the

other coefficients $|C_l(R,t)|^2$ dominates, leading to

$$\epsilon_{GI}(R,t) = \begin{cases} \epsilon_{BO}^{(2)}(R), & R < R_0 \\ \\ \epsilon_{BO}^{(1)}(R), & R > R_0. \end{cases} \tag{4.20}$$

The GD part of the TDPES (4.14), $\epsilon_{GD}(R,t)$, can be analyzed similarly. It may be written, in terms of the two BO states, as

$$\epsilon_{GD}(R,t) = |C_1(R,t)|^2 \dot{\gamma}_1(R,t) + |C_2(R,t)|^2 \dot{\gamma}_2(R,t) \tag{4.21}$$

and we recall that $\gamma_l(R,t)$ is the phase of the coefficient $C_l(R,t)$. As in Eq. (4.20), outside the step region, this part of the potential becomes

$$\epsilon_{GD}(R,t) = \begin{cases} \dot{\gamma}_2(R,t), & R < R_0 \\ \\ \dot{\gamma}_1(R,t), & R > R_0. \end{cases} \tag{4.22}$$

Moreover, Fig. 4.3 shows that in these regions $\dot{\gamma}_1(R,t)$ and $\dot{\gamma}_2(R,t)$ are constant functions of R. This is a consequence of the gauge we chose. The gauge condition, $A(R,t) = \langle \Phi_R(t)| - i\nabla_R \Phi_R(t)\rangle_r = 0$, in terms of the two BO states involved in the dynamics, reads

$$\begin{aligned} 0 = \sum_{l=1,2} |C_l(R,t)|^2 \nabla_R \gamma_l(R,t) - \frac{i}{2} \nabla_R \sum_{l=1,2} |C_l(R,t)|^2 \\ + \sum_{l,k=1,2} C_l^*(R,t) C_k(R,t) \mathcal{F}_{lk}^{BO}(R). \end{aligned} \tag{4.23}$$

However, the second term of the r.h.s. is identically zero, due to the PNC in Eq. (4.9), and the third term can be neglected, due to the presence of the non-adiabatic couplings, $\mathcal{F}_{lk}^{BO}(R)$, that are small far from the avoided crossing. The gauge condition then states

$$|C_1(R,t)|^2 \nabla_R \gamma_1(R,t) = -|C_2(R,t)|^2 \nabla_R \gamma_2(R,t), \tag{4.24}$$

or equivalently

$$\nabla_R \gamma_2(R,t) = 0 \quad \text{for} \quad R < R_0 \quad \text{where} \quad |C_1(R,t)|^2 = 0 \tag{4.25}$$

$$\nabla_R \gamma_1(R,t) = 0 \quad \text{for} \quad R > R_0 \quad \text{where} \quad |C_2(R,t)|^2 = 0. \tag{4.26}$$

We obtain $\gamma_l(R,t) = \Gamma_l(t)$, namely the phase of the coefficient $C_l(R,t)$ is only a function

of time (constant in space) in the region where the squared modulus of the corresponding coefficient is equal to unity. Similarly, $\dot{\gamma}_l(R,t) = \dot{\Gamma}_l(t)$, as shown in Fig. 4.3.

In the step region, around R_0, the expression of the TDPES can be approximated as

$$\begin{aligned}\epsilon(R,t) =& \frac{\epsilon^{(1)}_{BO}(R) + \epsilon^{(2)}_{BO}(R)}{2} + \frac{\dot{\gamma}_1(R,t) + \dot{\gamma}_2(R,t)}{2} \\ &+ \alpha(t)\left[\frac{\epsilon^{(1)}_{BO}(R) - \epsilon^{(2)}_{BO}(R)}{2} + \frac{\dot{\gamma}_1(R,t) - \dot{\gamma}_2(R,t)}{2}\right](R - R_0). \end{aligned} \tag{4.27}$$

The first two terms on the r.h.s. are the average of the BO energies plus the average value of the time-derivative of the phases $\gamma_1(R,t)$ and $\gamma_2(R,t)$; the terms in square brackets are the energy gaps between the BO surfaces and between the time-derivative of the phases, which give the contribution proportional to the parameter $\alpha(t)$. From Fig. 4.3, we notice that, around R_0, the slope of ϵ_{GD} is opposite to the slope of ϵ_{GI} and this is a general feature in the studied system (in the absence of a time-dependent external field).

A rough estimate of the second term in square brackets in Eq. (4.27) is obtained from semi-classical considerations [62]. We introduce the symbol $\lambda_l(R,t)$ to indicate the phase of the coefficients $F_l(R,t)$ in the expansion (4.5) and, using Eq. (4.8), we write the relation between $\gamma_l(R,t)$ and $\phi_l(R,t)$

$$\gamma_1(R,t) - \gamma_2(R,t) = \lambda_1(R,t) - \lambda_2(R,t). \tag{4.28}$$

Regarding each $F_l(R,t)$ as a "partial" nuclear wave-packet propagating on the corresponding BO surface and neglecting the couplings to the other surfaces, the phases can be approximated as

$$\lambda_l(R,t) = P_l(t)(R - R_l(t)) + \int^t d\tau \left[P_l(\tau)\dot{R}_l(\tau) - H_l\left(P_l(\tau), R_l(\tau), \tau\right)\right], \tag{4.29}$$

where $R_l(t), P_l(t)$ are the mean position and momentum, respectively, and the second term is the classical action. The mean positions, $R_1(t)$ and $R_2(t)$, at time $t = 26.61\ fs$ are shown in Fig. 4.3. The time-derivative of this expression leads to

$$\dot{\lambda}_l(R,t) = \dot{P}_l(t)\left(R - R_l(t)\right) - H_l\left(P_l(t), R_l(t), t\right) \tag{4.30}$$

$$\simeq -\left[\nabla_R \epsilon^{(l)}_{BO}(R)\Big|_{R_l(t)}\left(R - R_l(t)\right) + \epsilon^{(l)}_{BO}(R)\Big|_{R_l(t)}\right] - \frac{P_l^2}{2M}, \tag{4.31}$$

where we used $H_l \simeq P_l^2/(2M) + \epsilon_{BO}^{(l)}(R_l)$ and the classical equation of motion $\dot{P}_l = -\nabla_R \epsilon_{BO}^{(l)}(R)|_{R_l}$. In square brackets, we identify the zero-th and first order terms of the Taylor-expansion of $\epsilon_{BO}^{(l)}(R)$ around R_l, from which we conclude that the spatial dependence of the term $\dot{\gamma}_1(R,t) - \dot{\gamma}_2(R,t)$ in the region of the step (ΔR around R_0) is dominated by

$$\dot{\gamma}_1(R,t) - \dot{\gamma}_2(R,t) \simeq -\left(\epsilon_{BO}^{(1)}(R \sim R_1(t)) - \epsilon_{BO}^{(2)}(R \sim R_2(t))\right) + \mathcal{O}\left((R-R_1)^2, (R-R_2)^2\right). \tag{4.32}$$

The leading term in this expression has the opposite slope if compared to the first term in square brackets in Eq. (4.27) and almost cancels it. We will confirm this observation in Fig. 4.8 below, where the full TDPES will be shown.

4.2.3 Weaker non-adiabatic coupling

Now we study a case of weaker non-adiabatic coupling between the two lowest BO states. In order to make the coupling weaker, we choose the parameters in the Hamiltonian (3.15) as $L = 19.0\ a_0$, $R_f = 3.8\ a_0$, $R_l = 2.0\ a_0$ and $R_r = 5.5\ a_0$. The BO surfaces, along with the evolution of the populations of the BO states, are shown in Fig. 4.4. The

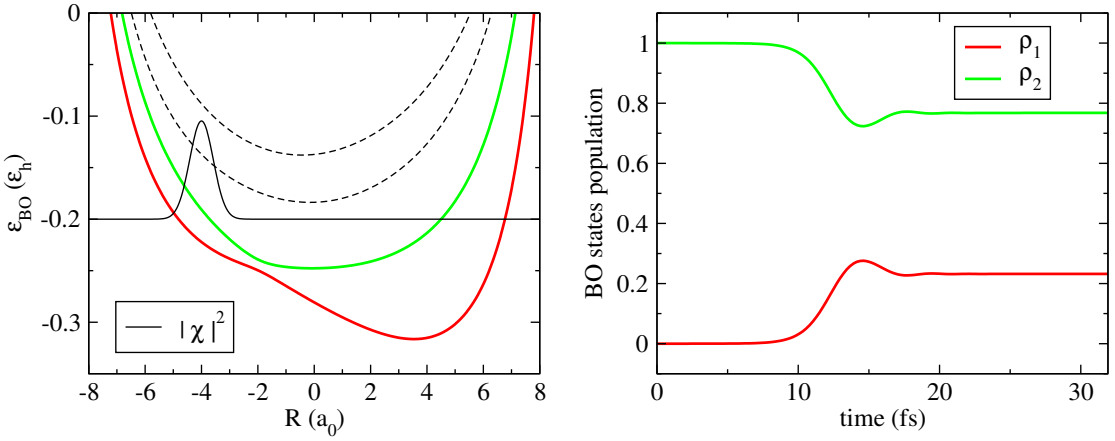

FIGURE 4.4: Same as Fig. 4.1 but for a weaker non-adiabatic coupling between the two lowest BO states.

initial conditions for the dynamical evolution of this system are the same as in the previous example, however the coupling between the two lowest electronic states is weaker, thus leading to a reduced population exchange, clearly shown in Fig. 4.4 (right panel). Nonetheless, the process described here shows similarities to the previous case, as can

be seen from Fig. 4.5. The GI part of the TDPES presents again two main features,

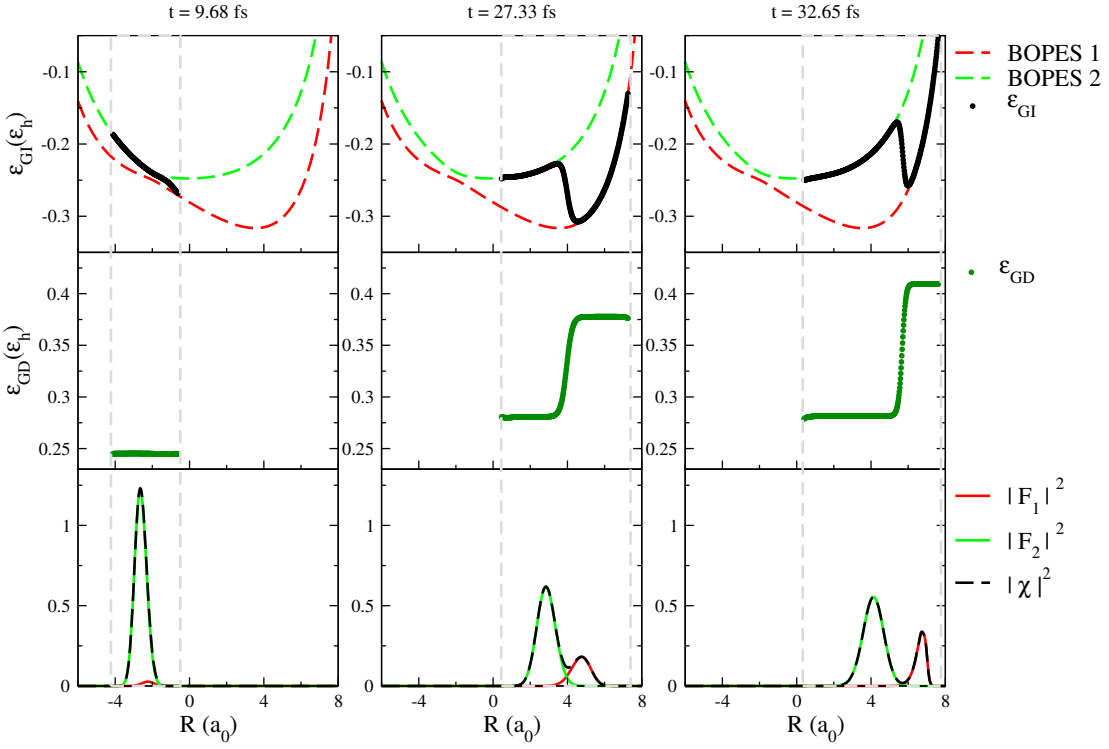

FIGURE 4.5: Same as Fig. 4.2 but for a weaker non-adiabatic coupling between the two lowest BO states, at time-steps 9.68 fs, 27.33 fs and 32.65 fs.

(i) the diabatization at the avoided crossing, when the nuclear wave-packet crosses the region of relatively strong non-adiabatic coupling and (ii) the steps at the cross-over of $|F_1(R,t)|^2$ and $|F_2(R,t)|^2$, signature of the splitting of the nuclear density. The GD part is either constant, before the splitting at the avoided crossing, or stepwise constant, with steps appearing in the same region as the steps in the GI term, but with opposite slope. At different snapshots in time, i.e., 9.68 fs, 27.33 fs and 32.65 fs, these properties are shown in Fig. 4.5, along with the nuclear density and its components on the BO states. The notation used in this figures is the same as in Fig. 4.2.

A slightly different behavior from the situation of strong non-adiabatic coupling can be identified in $\epsilon_{GI}(R,t)$ before the passage through the avoided crossing. As the nuclear wave-packet approaches the avoided crossing, the GI part of the TDPES "opens" towards the direction of motion, resembling the diabatic surface that connects the BO surfaces through the avoided crossing. This is clearly shown in Fig. 4.6 (left) at time $t = 9.68\ fs$ for the strongly coupled system. In the case of weaker non-adiabatic coupling, $\epsilon_{GI}(R,t)$, at the avoided crossing, lies between the BO surfaces, as shown in Fig. 4.6 (right).

Therefore, the diabatization feature strictly depends on the strength of the non-adiabatic

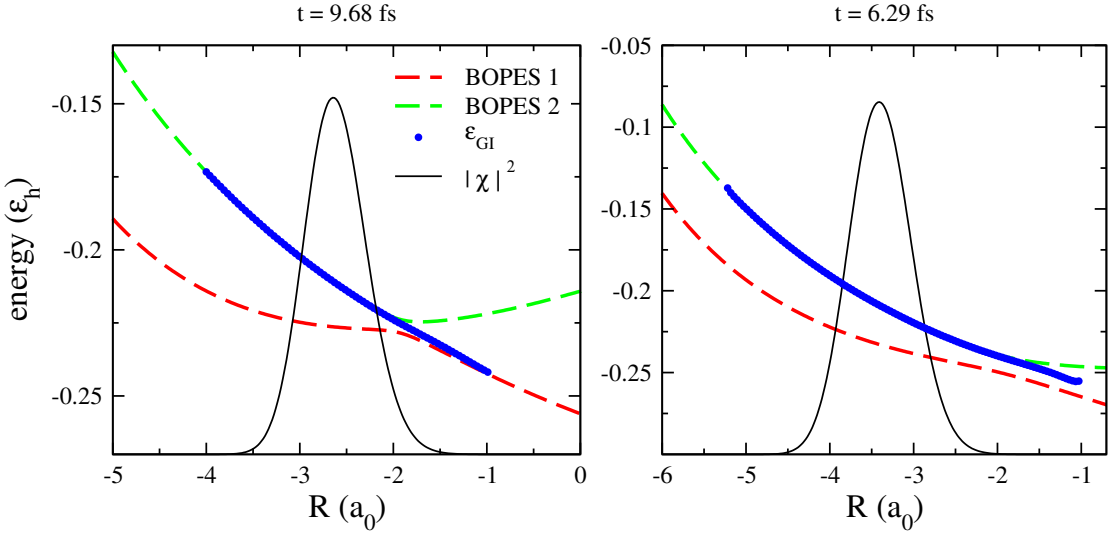

FIGURE 4.6: Diabatization feature of $\epsilon_{GI}(R,t)$ (blue dots) for the two model systems (left panel, strong coupling at $t = 9.68\ fs$, and right panel, weak coupling at $t = 6.29\ fs$) presented here. The dashed lines represent the BO surfaces ($\epsilon^{(1)}_{BO}(R)$ red line and $\epsilon^{(2)}_{BO}(R)$ green line) and the continuous black line represents the nuclear density (reduced by a factor 10 and rigidly shifted along the y-axis).

coupling and, in general, can be viewed as a transient configuration of the GI part of the TDPES before the formation of the steps.

4.2.4 Classical dynamics on the TDPES

In the previous sections (4.2.1-4.2.3), we have addressed and analyzed some of the generic features of the TDPES that governs the nuclear dynamics in the presence of non-adiabatic electronic transitions. As discussed before, some of these features, in particular, the steps that bridge between the two parts of the TDPES that are parallel to the BOPESs, are reminiscent of the jumping between the BOPESs in the algorithms such as Tully's surface hopping [60]. These algorithms are usually based on the mixed quantum-classical treatment of the electronic and nuclear dynamics using stochastic jumps between BO surfaces. Therefore, an ensemble of classical trajectories with different initial conditions is needed to achieve reasonable outcomes. On the other hand, the TDPES is the exact time-dependent potential that governs the nuclear dynamics (in general together with the vector potential) and contains the quantum backreaction resulting from the exact coupling to the electronic subsystem. This brings us to investigate how the TDPES drives the classical point-like nuclei.

In order to understand how the generic features of the TDPES affect the classical nuclear dynamics, we have employed the surfaces presented in the previous sections (4.2.1 and 4.2.3) to calculate the forces acting on the nuclear degree of freedom. We compare the resulting dynamics using the forces that are calculated from the gradient of the TDPES and from the gradient of its GI part. The classical propagation starts at the initial position $R_c = -4.0\ a_0$ with zero initial velocity. Here, we use the velocity-Verlet algorithm to integrate the Hamilton's equations,

$$\begin{cases} \dot{R} &= \dfrac{P}{M} \\ \\ \dot{P} &= -\nabla_R \epsilon(R) \quad \text{or} \quad -\nabla_R \epsilon_{GI}(R), \end{cases} \tag{4.33}$$

using the same time-steps as in the quantum propagation ($\delta t = 2.4\times10^{-3}\ fs$). In Fig. 4.7 (upper panels) we present the evolution of the classical position compared to the average nuclear position from the quantum calculation, for strong and weak coupling. In both cases, a single trajectory, evolving on the exact surface (blue lines in Fig. 4.7), is able to reproduce the mean nuclear path (dashed black lines) fairly well. A slight deviation from the quantum results happens only towards the end of the simulated trajectories. When the classical forces are calculated from the GI part of the TDPES, the corresponding classical trajectory in the strong coupling case, does not show a large deviation from the exact calculation. However, in the weak coupling case, after 20 fs, the classical trajectory deviates considerably from the quantum mean path. This behavior is also confirmed by the pronounced increase of the velocity of the classical particle moving on ϵ_{GI}, shown in Fig. 4.7 (lower panels). Interestingly, in the strong coupling regime (Fig. 4.7, lower panel-left), the velocity calculated from the classical dynamics on the full TDPES presents a similar, less enhanced, behavior compared to the velocity calculated from the classical dynamics on the GI part of the TDPES.

We now have a closer look at the classical dynamics and try to find out the source of the deviations, specially in the weaker coupling case. Fig. (4.8) shows the classical positions calculated from the full TDPES (blue dots) and the GI part of it (orange dots) together with the corresponding potentials and the exact nuclear densities at the times indicated in the plots. It can be seen in the figure that the classical particle evolving on the GI part of the potential, in the case of weaker coupling, at the moment of the step formation feels an intense force, as its position is exactly in the region of the step.

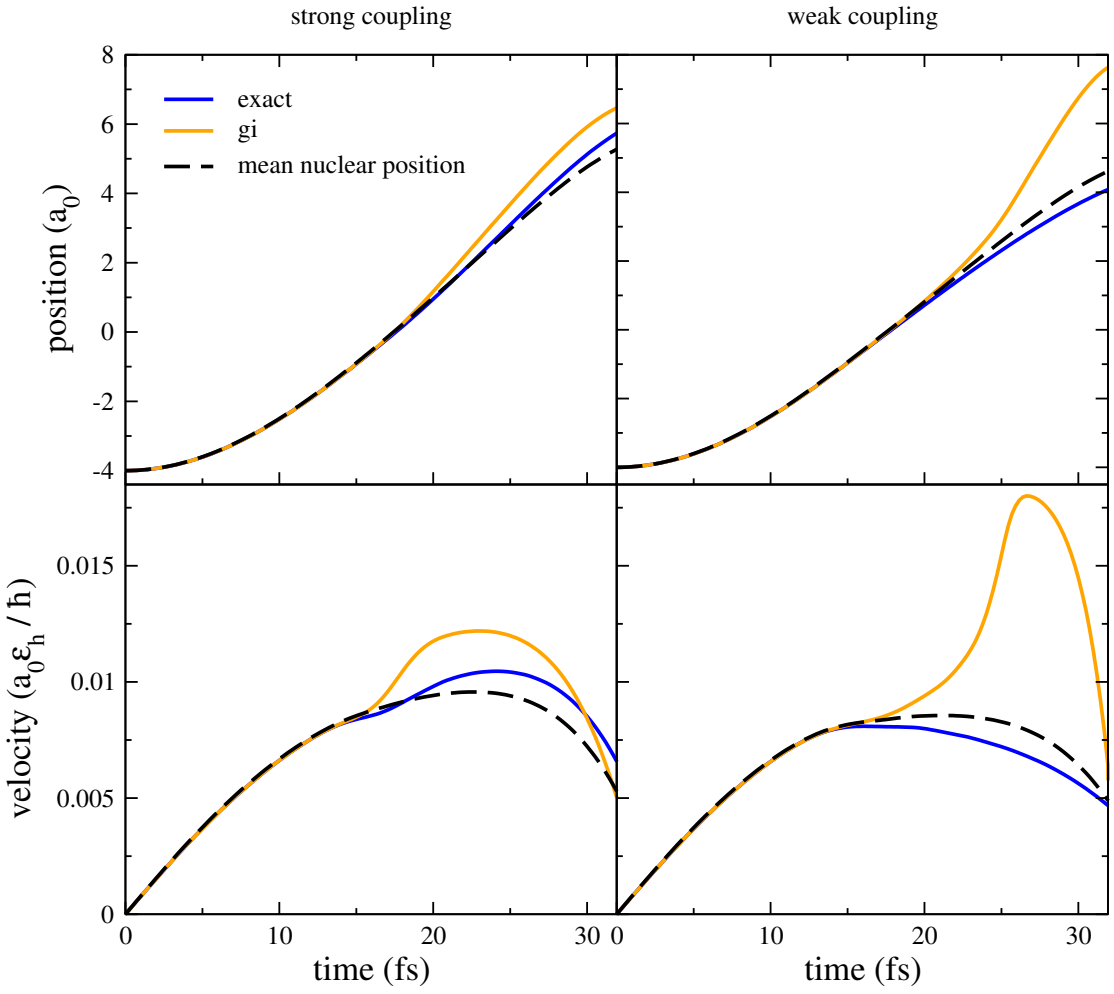

FIGURE 4.7: Classical position (upper panels) and velocity (lower panels) and average nuclear position and velocity as functions of time for the systems in the presence of strong non-adiabatic coupling (left) and of weak non-adiabatic coupling (right). The dashed black line represents the average nuclear values from quantum calculation, the blue and orange lines are the positions (upper panels) and velocities (lower panel) of the classical particle when it evolves on the exact potential and on the GI part of the potential, respectively.

This happens also in the case of the strong coupling (see the blue line referring to the velocity in Fig. 4.7, left plot), to a lesser extent and the velocity of the classical particle does not present a strong peak. The evolution of the classical particle on the GI part, in the case of the strong coupling, shows that the step forms in the direction of larger nuclear density (see plot at $t = 22.25\ fs$), hence, the classical particle correctly follows the step and its position is approximately the mean nuclear position. However, in the case of weaker coupling, the step forms in the direction of smaller nuclear density and the classical particle cannot move "up the hill" to follow the nuclear mean path and remains in the step region until an intense force drives it down the step. In the later

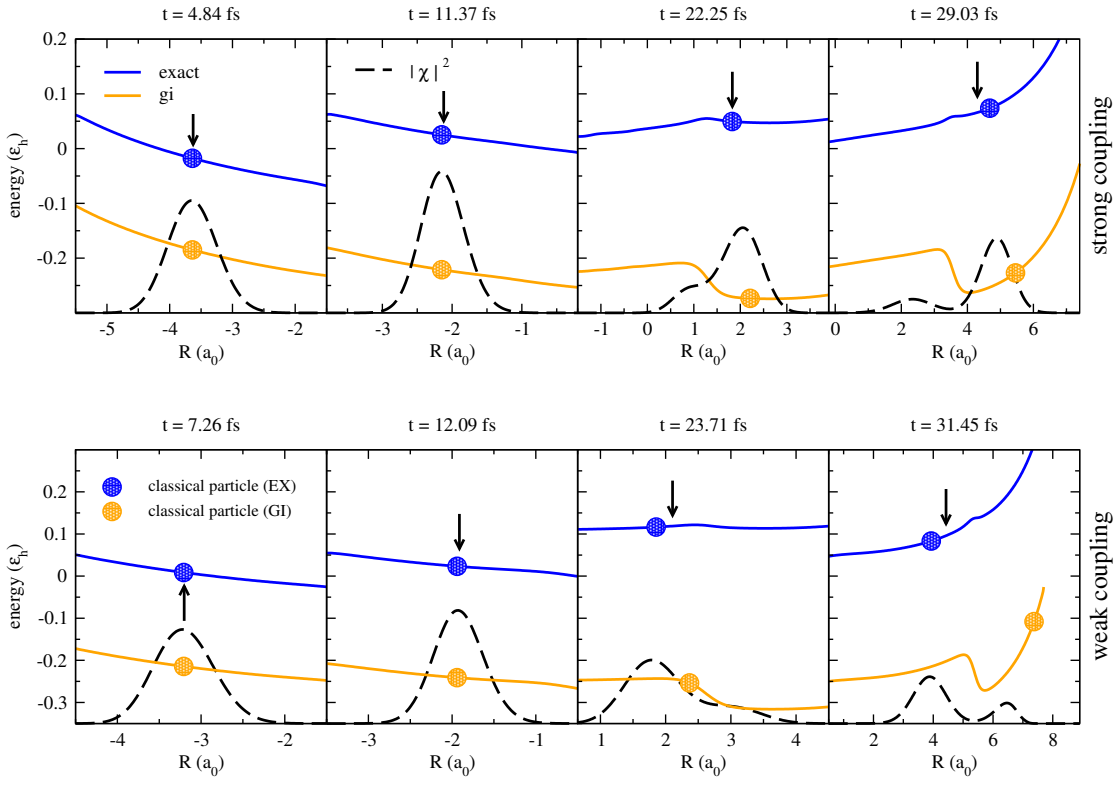

FIGURE 4.8: Upper panels: strong coupling results. Lower panels: weak coupling results. The figure shows classical positions (dots) at different times, as indicated in the plots, with the corresponding potentials, $\epsilon_{GI}(R,t)$ (orange lines) and $\epsilon(R,t)$ (blue lines). The nuclear density (dashed black line) is plotted as reference, along with the mean position (black arrows).

case, an exaggerated increase of the velocity is responsible for the large deviation of the classical position from the quantum mean position.

From comparing the classical and quantum dynamics shown in Fig. 4.8, we observe that in the strong coupling case (upper panel), at $t = 4.84\ fs$ and at $t = 11.37\ fs$, the nuclear wave-packet has not yet crossed the avoided crossing, thus the GD part of the TDPES is a constant. Therefore, the classical force calculated from the TDPES is identical with the one calculated from its GI part. At these times, the classical positions of the nuclei evolving on the GI part of the potential (orange dots in the figure) and on the full TDPES (blue dots) coincide with the mean position of the nuclear wave-packet (black arrows). On the other hand, in the weaker coupling case (lower panels), a similar behavior is seen before the wave-packet splitting, at $t = 7.26\ fs$ and $t = 12.09\ fs$. At later times, namely $t = 22.25\ fs$ for the strong coupling case and $t = 23.71\ fs$ for the weaker coupling case, the steps develop in ϵ_{GI} and the classical particle evolving on this potential follows the direction in which the step is forming: in the case of strong

coupling, this region coincides with the region associated with larger nuclear density, whereas this is not the case for the weaker coupling case. As discussed above, this feature explains why the positions of the particles on $\epsilon(R,t)$ and on $\epsilon_{GI}(R,t)$, for the system in the presence of strong non-adiabatic coupling, are close to each other also at later times ($t = 29.03\ fs$ in Fig. 4.8), whereas they deviate in the weaker coupling regime as clearly shown in the figure at time $t = 31.45\ fs$.

4.2.5 Ehrenfest theorem for the nuclear wave-function

In the previous section (4.2.4) we studied the classical nuclear dynamics on the TDPES. However, we did not provide any argument how that study can be associated with a classical limit of the nuclear motion that is able to, approximately, reproduces the expectation values of the nuclear position and momentum of the complete electron-nuclear system.

Here, using the Ehrenfest theorem, we show how the nuclear position and momentum calculated from Eq. (4.33) can be linked to the expectation values of the nuclear position and momentum of the complete electron-nuclear system. The Ehrenfest theorem relates the time-derivative of the expectation value of a quantum-mechanical operator $\hat{O}$ to the expectation value of the commutator of that operator with the Hamiltonian, i.e.

$$\frac{d}{dt}\langle\hat{O}(t)\rangle = \frac{1}{i\hbar}\left\langle\left[\hat{O}(t),\hat{H}\right]\right\rangle + \langle\partial_t\hat{O}(t)\rangle. \tag{4.34}$$

The second term on the r.h.s. refers to the explicit time-dependence of $\hat{O}$. In particular, the theorem leads to the classical-like equations of motion for the mean value of position and momentum operators. For a system of electrons and nuclei, described by the Hamiltonian in Eq. (2.2) and the wave-function $\Psi(\underline{\mathbf{r}},\underline{\underline{\mathbf{R}}},t)$, the mean values of the ν-th nuclear position $\hat{\mathbf{R}}_\nu$ and momentum $\hat{\mathbf{P}}_\nu$ operators evolve according to the classical Hamilton's equations

$$\frac{d}{dt}\langle\hat{\mathbf{R}}_\nu\rangle_\Psi = \frac{1}{i\hbar}\left\langle\left[\hat{\mathbf{R}}_\nu,\hat{H}(\underline{\mathbf{r}},\underline{\underline{\mathbf{R}}})\right]\right\rangle_\Psi = \frac{\langle\hat{\mathbf{P}}_\nu\rangle_\Psi}{M_\nu} \tag{4.35}$$

$$\frac{d}{dt}\langle\hat{\mathbf{P}}_\nu\rangle_\Psi = \frac{1}{i\hbar}\left\langle\left[\hat{\mathbf{P}}_\nu,\hat{H}(\underline{\mathbf{r}},\underline{\underline{\mathbf{R}}})\right]\right\rangle_\Psi = \langle-\nabla_\nu\big(\hat{V}_{en}(\underline{\mathbf{r}},\underline{\underline{\mathbf{R}}}) + \hat{W}_{nn}(\underline{\underline{\mathbf{R}}})\big)\rangle_\Psi. \tag{4.36}$$

Here, the operators do not depend explicitly on time and we indicate the integration over the full wave-function (electronic and nuclear coordinates) by $\langle\cdot\rangle_\Psi$. On the other hand, the nuclear equation (2.30) is a Schrödinger equation that contains a time-dependent

vector potential and a time-dependent scalar potential. Therefore, the Ehrenfest theorem for the nuclear subsystem reads

$$\frac{d}{dt}\langle\hat{\mathbf{R}}_\nu\rangle_\chi = \frac{1}{i\hbar}\left\langle\left[\hat{\mathbf{R}}_\nu, \hat{H}_n(\underline{\underline{\mathbf{R}}})\right]\right\rangle_\chi = \frac{\langle\hat{\hat{\mathbf{P}}}_\nu\rangle_\chi}{M_\nu} \tag{4.37}$$

$$\frac{d}{dt}\langle\hat{\hat{\mathbf{P}}}_\nu\rangle_\chi = \frac{1}{i\hbar}\left\langle\left[\hat{\hat{\mathbf{P}}}_\nu, \hat{H}_n(\underline{\underline{\mathbf{R}}})\right]\right\rangle_\chi + \left\langle\partial_t\mathbf{A}_\nu(\underline{\underline{\mathbf{R}}}, t)\right\rangle_\chi , \tag{4.38}$$

where

$$\hat{\hat{\mathbf{P}}}_\nu = -i\hbar\nabla_\nu + \mathbf{A}_\nu(\underline{\underline{\mathbf{R}}}, t) \tag{4.39}$$

is the expression of the nuclear momentum operator in position representation, and

$$\hat{H}_n(\underline{\underline{\mathbf{R}}}) = \sum_{\nu=1}^{N_n}\frac{\left[-i\hbar\nabla_\nu + \mathbf{A}_\nu(\underline{\underline{\mathbf{R}}}, t)\right]^2}{2M_\nu} + \epsilon(\underline{\underline{\mathbf{R}}}, t) \tag{4.40}$$

is the nuclear Hamiltonian of the Eq. (2.30). Note that the average operation is performed only on the nuclear wave-function as indicated by $\langle\cdot\rangle_\chi$. An explicit time-dependence appears in the expression of the momentum operator, due to the presence of the vector potential. This dependence is accounted for in the second term on the r.h.s of Eq. (4.38).

Eq. (4.37) can be easily obtained from Eq. (4.35) by using the relation

$$\hat{\mathbf{P}}_\nu\Psi(\underline{\mathbf{r}}, \underline{\underline{\mathbf{R}}}, t) = \hat{\mathbf{P}}_\nu\chi(\underline{\underline{\mathbf{R}}}, t)\Phi_{\underline{\underline{\mathbf{R}}}}(\underline{\mathbf{r}}, t) = \left(\hat{\mathbf{P}}_\nu\chi(\underline{\underline{\mathbf{R}}}, t)\right)\Phi_{\underline{\underline{\mathbf{R}}}}(\underline{\mathbf{r}}, t) + \chi(\underline{\underline{\mathbf{R}}}, t)\left(\hat{\mathbf{P}}_\nu\Phi_{\underline{\underline{\mathbf{R}}}}(\underline{\mathbf{r}}, t)\right) \tag{4.41}$$

and integrating out the electronic coordinates in both sides of the equation. To obtain Eq. (4.38) from Eq. (4.36), we rewrite Eq. (4.36) as

$$\begin{aligned}\frac{d}{dt}\langle\hat{\mathbf{P}}_\nu\rangle_\Psi = &\int d\underline{\mathbf{r}}d\underline{\underline{\mathbf{R}}}\left[\Phi^*_{\underline{\underline{\mathbf{R}}}}(\underline{\mathbf{r}}, t)\partial_t\chi^*(\underline{\underline{\mathbf{R}}}, t) + \chi^*(\underline{\underline{\mathbf{R}}}, t)\partial_t\Phi^*_{\underline{\underline{\mathbf{R}}}}(\underline{\mathbf{r}}, t)\right]\hat{\mathbf{P}}_\nu\chi(\underline{\underline{\mathbf{R}}}, t)\Phi_{\underline{\underline{\mathbf{R}}}}(\underline{\mathbf{r}}, t)\\ &+ \int d\underline{\mathbf{r}}d\underline{\underline{\mathbf{R}}}\,\chi^*(\underline{\underline{\mathbf{R}}}, t)\Phi^*_{\underline{\underline{\mathbf{R}}}}(\underline{\mathbf{r}}, t)\hat{\mathbf{P}}_\nu\left[\Phi_{\underline{\underline{\mathbf{R}}}}(\underline{\mathbf{r}}, t)\partial_t\chi(\underline{\underline{\mathbf{R}}}, t) + \chi(\underline{\underline{\mathbf{R}}}, t)\partial_t\Phi_{\underline{\underline{\mathbf{R}}}}(\underline{\mathbf{r}}, t)\right].\end{aligned} \tag{4.42}$$

Then we use the nuclear equation (2.30) for

$$\partial_t\chi(\underline{\underline{\mathbf{R}}}, t) = \frac{1}{i\hbar}\hat{H}_n(\underline{\underline{\mathbf{R}}})\chi(\underline{\underline{\mathbf{R}}}, t) \tag{4.43}$$

and its complex-conjugated ($\hat{H}_n(\underline{\underline{\mathbf{R}}})$ is hermitian), the definition of the (real) vector potential

$$\mathbf{A}_\nu(\underline{\underline{\mathbf{R}}}, t) = \int d\underline{\mathbf{r}}\Phi^*_{\underline{\underline{\mathbf{R}}}}(\underline{\mathbf{r}}, t)\hat{\mathbf{P}}_\nu\Phi_{\underline{\underline{\mathbf{R}}}}(\underline{\mathbf{r}}, t) \tag{4.44}$$

and the PNC, to derive

$$\frac{d}{dt}\langle\hat{\mathbf{P}}_\nu\rangle_\Psi = \frac{1}{i\hbar}\int d\underline{\underline{\mathbf{R}}}\,\chi^*(\underline{\underline{\mathbf{R}}},t)\left(\hat{\tilde{\mathbf{P}}}_\nu\hat{H}_n(\underline{\underline{\mathbf{R}}}) - \hat{H}_n(\underline{\underline{\mathbf{R}}})\hat{\tilde{\mathbf{P}}}_\nu\right)\chi(\underline{\underline{\mathbf{R}}},t) + \int d\underline{\underline{\mathbf{R}}}\,\left|\chi(\underline{\underline{\mathbf{R}}},t)\right|^2\int d\underline{\mathbf{r}}\left[\left(\partial_t\Phi^*_{\underline{\underline{\mathbf{R}}}}(\underline{\mathbf{r}},t)\right)\hat{\mathbf{P}}_\nu\Phi_{\underline{\underline{\mathbf{R}}}}(\underline{\mathbf{r}},t) + \Phi^*_{\underline{\underline{\mathbf{R}}}}(\underline{\mathbf{r}},t)\hat{\mathbf{P}}_\nu\partial_t\Phi_{\underline{\underline{\mathbf{R}}}}(\underline{\mathbf{r}},t)\right] \quad (4.45)$$

with $\hat{\tilde{\mathbf{P}}}_\nu = \hat{\mathbf{P}}_\nu + \mathbf{A}_\nu(\underline{\underline{\mathbf{R}}},t)$. Using

$$\left(\partial_t\Phi^*_{\underline{\underline{\mathbf{R}}}}(\underline{\mathbf{r}},t)\right)\hat{\mathbf{P}}_\nu\Phi_{\underline{\underline{\mathbf{R}}}}(\underline{\mathbf{r}},t) = \partial_t\left(\Phi^*_{\underline{\underline{\mathbf{R}}}}(\underline{\mathbf{r}},t)\hat{\mathbf{P}}_\nu\Phi_{\underline{\underline{\mathbf{R}}}}(\underline{\mathbf{r}},t)\right) - \Phi^*_{\underline{\underline{\mathbf{R}}}}(\underline{\mathbf{r}},t)\hat{\mathbf{P}}_\nu\partial_t\Phi_{\underline{\underline{\mathbf{R}}}}(\underline{\mathbf{r}},t), \quad (4.46)$$

for the term in the square brackets leads to

$$\frac{d}{dt}\langle\hat{\mathbf{P}}_\nu\rangle_\Psi = \int d\underline{\underline{\mathbf{R}}}\,\chi^*(\underline{\underline{\mathbf{R}}},t)\left(\frac{1}{i\hbar}\left[\hat{\tilde{\mathbf{P}}}_\nu,\hat{H}_n(\underline{\underline{\mathbf{R}}})\right] + \partial_t\mathbf{A}_\nu(\underline{\underline{\mathbf{R}}},t)\right)\chi(\underline{\underline{\mathbf{R}}},t), \quad (4.47)$$

recovering the term on the r.h.s. of Eq. (4.38). A similar procedure [56] yields the relation

$$\begin{aligned}\langle\hat{\mathbf{P}}_\nu\rangle_\Psi &= \int d\underline{\mathbf{r}}d\underline{\underline{\mathbf{R}}}\,\Phi^*_{\underline{\underline{\mathbf{R}}}}(\underline{\mathbf{r}},t)\chi^*(\underline{\underline{\mathbf{R}}},t)\left[\left(\hat{\mathbf{P}}_\nu\chi(\underline{\underline{\mathbf{R}}},t)\right)\Phi_{\underline{\underline{\mathbf{R}}}}(\underline{\mathbf{r}},t) + \chi(\underline{\underline{\mathbf{R}}},t)\hat{\mathbf{P}}_\nu\Phi_{\underline{\underline{\mathbf{R}}}}(\underline{\mathbf{r}},t)\right]\\ &= \int d\underline{\underline{\mathbf{R}}}\,\chi^*(\underline{\underline{\mathbf{R}}},t)\left[\hat{\mathbf{P}}_\nu + \mathbf{A}_\nu(\underline{\underline{\mathbf{R}}},t)\right]\chi(\underline{\underline{\mathbf{R}}},t) = \langle\hat{\tilde{\mathbf{P}}}_\nu\rangle_\chi, \end{aligned} \quad (4.48)$$

which proves the identity of the LHSs of Eqs. (4.36) and (4.38).

We have shown that from the Ehrenfest theorem that follows the nuclear equation (2.30) we can reproduce the expectation values of the nuclear position and momentum operators of the complete electron-nuclear system. This outcome is consistent with the interpretation of $\chi(R,t)$ as the proper nuclear wave-function that reproduces the nuclear density and current density of the complete system (see the discussion in Chapter 2).

In the one-dimensional system we studied here, the gauge is chosen such that $A(R,t) \equiv 0$, therefore, the Ehrenfest equations become

$$\frac{d}{dt}\langle\hat{R}\rangle_\chi = \frac{1}{i\hbar}\langle\left[\hat{R},\hat{H}_n\right]\rangle_\chi = \frac{\langle\hat{P}\rangle_\chi}{M} \quad (4.49)$$

$$\frac{d}{dt}\langle\hat{P}\rangle_\chi = \frac{1}{i\hbar}\langle\left[\hat{P},\hat{H}_n\right]\rangle_\chi = \langle-\nabla_R\epsilon(R,t)\rangle_\chi, \quad (4.50)$$

where the mean force generating the classical-like evolution is determined as the expectation value, on the nuclear wave-function, of the gradient of the TDPES. If we replace the nuclear wave-function in (4.50) by a delta function, we get Eq. (4.33) that was used in the previous section (4.2.4). That is why the classical nuclear dynamics on the TDPES could actually approximate the mean nuclear position and momentum.

4.2.6 Evolution of the electronic conditional wave-function

We conclude this section (4.2) by discussing the evolution of the electronic wave-function, $\Phi_R(r,t)$, for the set of parameters, used in sec. (4.2.1). In order to have a complete picture of the non-adiabatic process, happening in the system, in terms of $\chi(R,t)$, $\Phi_R(r,t)$ and $\epsilon(R,t)$, we repeat part of the discussions on the features of the TDPES. The first three BOPES are shown in Fig. 4.9 (left panel), together with the BO conditional electronic densities $|\phi_R^{(1)}(r)|^2$ and $|\phi_R^{(2)}(r)|^2$ (right panels). As expected, $|\phi_R^{(1)}(r)|^2$ and $|\phi_R^{(2)}(r)|^2$ exhibit abrupt changes, along the R-axis, at the position of the avoided crossing, R_{ac}: $|\phi_R^{(1)}(r)|^2$ switches from being localized around the fixed ion on the left ($r = -9.5\ a_0$), to be localized around the one on the right ($r = 9.5\ a_0$); $|\phi_R^{(2)}(r)|^2$ on the other hand, presents a single-peak structure for $R < R_{ac}$ and a double-peak structure for $R > R_{ac}$.

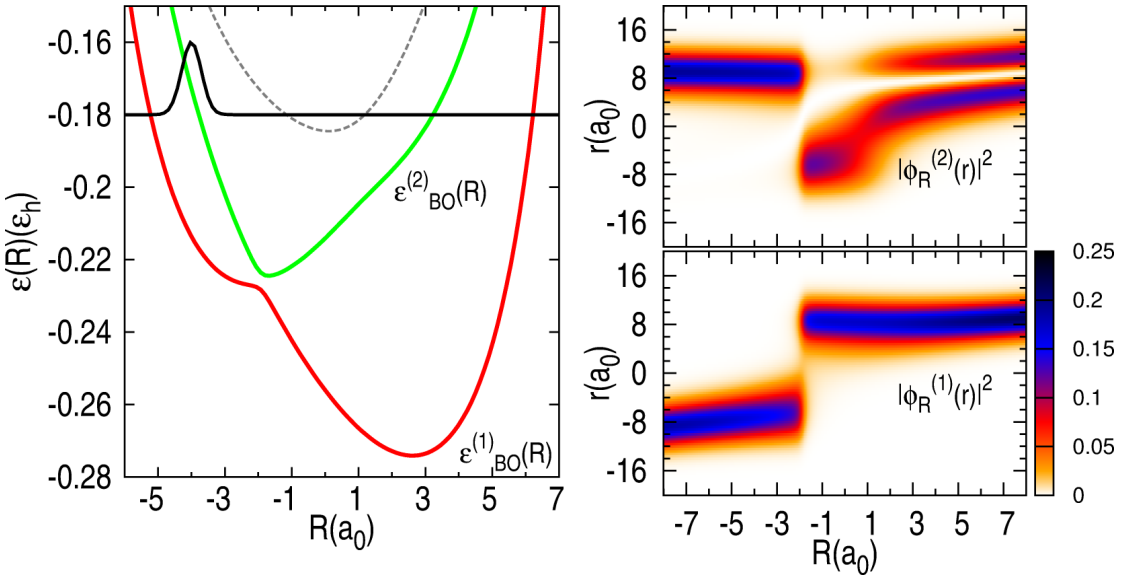

FIGURE 4.9: Left: The first two BOPESs (indicated in the figure) together with the 3rd BOPES (black dashed-line) and the initial nuclear wave-function (black solid-line) . Right: Adiabatic electronic conditional densities as indicated in the figures

Again, we suppose that the system is initially excited to $\epsilon_{BO}^{(2)}$ and the initial nuclear wave-function is a wave-packet with the width $\sigma = 1/\sqrt{2.85}$, centered at $R = -4.0\ a_0$ (see Fig. 4.9, black solid-line). In Fig. 4.10 (upper panel) the gauge-invariant part of the TDPES (4.3), ϵ_{GI}, is plotted (black solid-line) at four different times, along with the two lowest BOPESs, $\epsilon_{BO}^{(1)}$ (red dashed-line) and $\epsilon_{BO}^{(2)}$ (green dashed-line). In the second panel (from the top), the gauge-dependent part of the TDPES (4.4), ϵ_{GD}, is plotted at the

same times. In the third panel (from the top), the exact nuclear density (black dashed-line), $|\chi(R,t)|^2$, is shown together with the absolute value squared of the projection of the full wave-function on the first and second BO electronic states, i.e., $|F_1(R,t)|^2 = |\int dr\, \phi_R^{(1)*}(r)\, \Psi(r,R,t)|^2$ (red solid-line) and $|F_2(R,t)|^2 = |\int dr\, \phi_R^{(2)*}(r)\, \Psi(r,R,t)|^2$ (green solid-line). In the lowest panel, $|\Phi_R(r,t)|^2$ is presented.

As discussed in sec. (4.2.1), at the initial time ($t = 0$), due to the choice of the initial state, the TDPES coincides with $\epsilon_{BO}^{(2)}$. Since $\Psi_0(r,R)$ is not an eigenstate of the Hamiltonian (3.15), it evolves in time. At $t = 9.0fs$, ϵ_{GI} coincides with $\epsilon_{BO}^{(2)}$ for $R < R_{ac}$, goes smoothly through the avoided crossing region and follows $\epsilon_{BO}^{(1)}$ for $R > R_{ac}$, resembling the *diabatic* PES of state 2 in Ref. [54], in which the electron interacts with the fixed ion on the right ($r = 9.5\ a_0$) and with the moving ion, but not with the fixed ion on the left ($r = -9.5\ a_0$). As ϵ_{GD} is constant in this region (Fig. 4.10), the TDPES is identical with ϵ_{GI} [4]. The nuclear wave-packet is driven by the TDPES to spread towards the avoided crossing of two BOPESs, where a significant non-adiabatic transition happens and the exact nuclear density splits. Already at this moment, a slight transition of the nuclear wave-packet to the lower surface is visible around the avoided crossing. At later times, e.g., $t = 16.22\ fs$, $t = 26.24\ fs$ and $t = 57.35\ fs$., far from the avoided crossing, ϵ_{GI} contains steps that connect its different pieces that are on top of different BOPESs in different slices of R-space. In the region around R_{ac}, it follows the diabatic surface that passes smoothly through the avoided crossing. On the other hand, ϵ_{GD} is piecewise constant and presents similar steps as ϵ_{GI}. Therefore, the TDPES, $\epsilon_{GI} + \epsilon_{GD}$, preserves the features mentioned before, i.e., (i) far from the avoided crossing, it presents steps that connect the regions in R-space in which the TDPES has the shape of one BOPES to the regions in which it has the shape of the other BOPES; (ii) around the avoided crossing, it follows the diabatic surface that smoothly connects one BOPES to the other.

The exact time-dependent electronic conditional density, shown in the lower panels of Fig. 4.10 at different times, behaves similarly to the TDPES: (i) it smoothly connects a $|\phi_R^{(2)}(r)|^2$-like structure, by crossing R_{ac}, with a $|\phi_R^{(1)}(r)|^2$-like structure, or vice versa, presenting a diabatic behavior, e.g. at $t = 9.0\ fs$; (ii) it displays abrupt changes, between regions that piecewise match different adiabatic conditional densities.

[4] In Fig. 4.10, curves representing ϵ_{GD} have been rigidly shifted along the energy axis

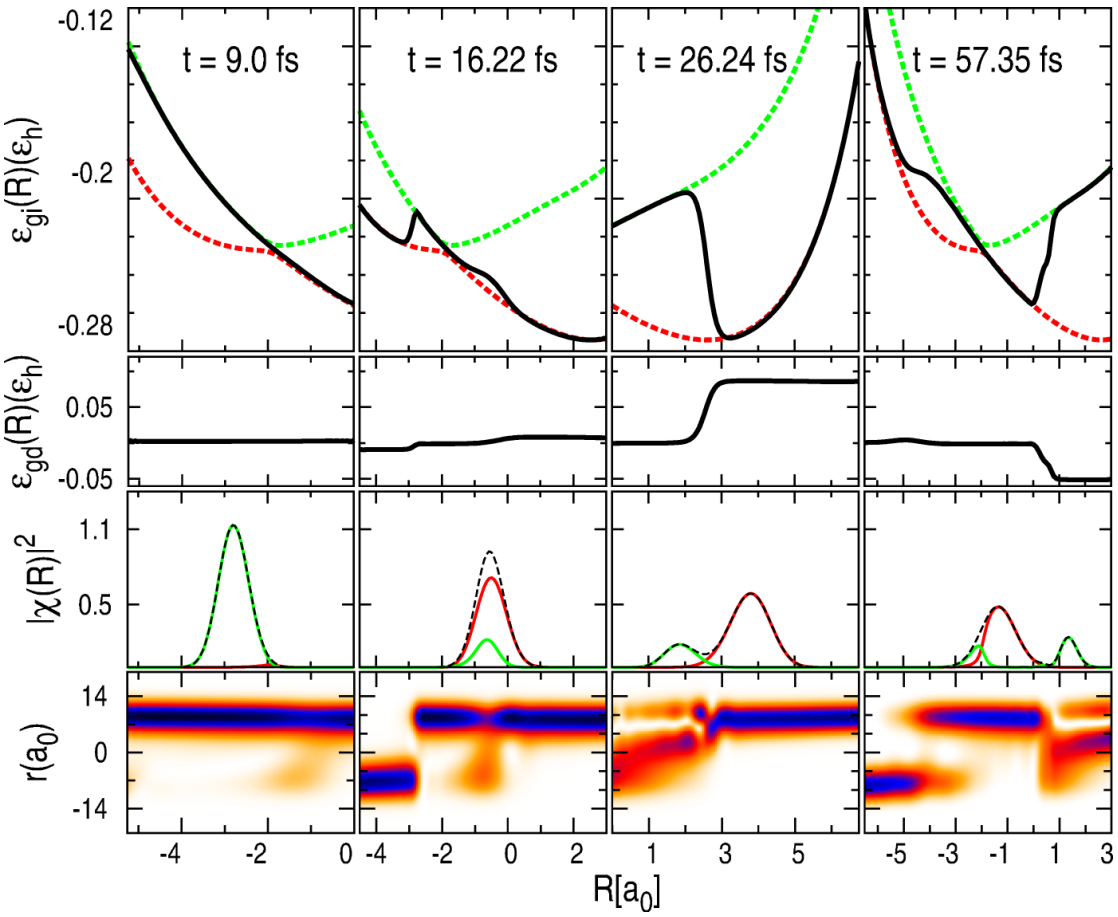

FIGURE 4.10: First panel (top): The gauge independent part of the TDPES (black solid-line) plotted at four different times (indicated), $\epsilon_{BO}^{(1)}$ (red dashed-line) and $\epsilon_{BO}^{(2)}$ (green dashed-line). Second panel (from the top): the gauge dependent part of the TDPES is plotted at the same times. Third panel (from the top): the exact nuclear density (black dashed-line) is shown together with $|F_1(R,t)|^2$ (red solid-line) and $|F_2(R,t)|^2$ (green solid-line). Lowest panel: the exact time-dependent electronic conditional density, $|\Phi_R(r,t)|^2$, is plotted. The color range is the same as Fig. 4.9.

As an example, we discuss the TDPES at $t = 31.87\ fs$ in Fig. 4.11. As it is seen, ϵ_{GI} switches from $\epsilon_{BO}^{(1)}(R)$ to $\epsilon_{BO}^{(2)}(R)$ over the region where $|F_1|$ and $|F_2|$ cross (see the bottom plot). As $|F_1|$ and $|F_2|$ have opposite slopes and cross where they are small, α is large yielding a small ΔR. Outside the switching region, one of the $|C_k|^2$s becomes dominant. Interestingly, the exact electron-nuclear density contains signatures of the behavior ϵ_{GI}, i.e., where ϵ_{GI} coincides with $\epsilon_{BO}^{(1)}(R)$, presents one peak in analogy with $|\phi_R^{(1)}(r)|^2$ (see Fig. 4.9), while, it displays two peaks, like $|\phi_R^{(2)}(r)|^2$ (Fig. 4.9), where $\epsilon_{GI}(R,t)$ follows $\epsilon_{BO}^{(2)}(R)$. The step of ϵ_{GI} in the intermediate region is indicated by scars in the full electron-nuclear density.

4.3 Model of H_2^+ in a laser field

The interplay of nuclear and electronic dynamics in the presence of time-dependent external fields leads to fascinating phenomena, especially beyond the perturbative regime, e.g. photo-induced molecular dissociation, charge-resonance enhanced ionization, control of electron localization, electron-hole migration after photo-excitation, to name a few [9–13]. In this section, we illustrate the usefulness of the TDPES using a simple, numerically exactly solvable model: the H_2^+ molecular ion subject to a linearly polarized laser field (3.2.1).

We study the dynamics of the model H_2^+ system under a $\lambda = 228$ nm (5.4eV) UV-laser pulse which is represented by

$$E(t) = E_0 f(t) \sin(\omega t), \tag{4.51}$$

with two peak intensities, $I_1 = |E_0|^2 = 10^{14} W/\mathrm{cm}^2$ and $I_2 = |E_0|^2 = 2.5 \times 10^{13} W/\mathrm{cm}^2$. With this frequency an energy that is about twice as much as the dissociation energy

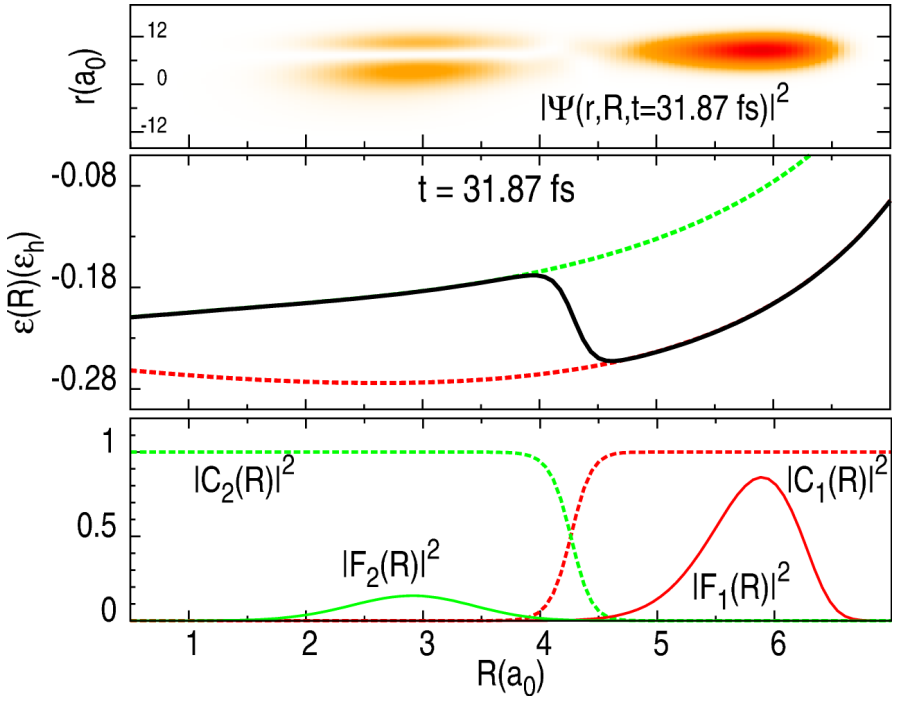

FIGURE 4.11: Top: the full electron-nuclear density at the $t = 31.87\ fs$. Middle: a snapshot of the gauge invariant part of the TDPES (solid black line) at the $t = 31.87\ fs$. For reference, $\epsilon_{BO}^{(1)}$ (red dashed-line) and $\epsilon_{BO}^{(2)}$ (green dashed-line) are shown. Bottom: Expansion coefficients (indicated in the figure) of the (two states) adiabatic expansion of the full wave-function and the exact electronic conditional wave-function (see the text) at the $t = 31.87 fs$.

of the model molecule (2.8782eV) is achieved, so dissociation is expected. The envelope function $f(t)$ is chosen such that the field is linearly ramped from zero to its maximum strength at $t = T_{ramp}$ and thereafter held constant (Fig. 4.12):

$$f(t) = \begin{cases} t/T_{ramp} & 0 < t < T_{ramp} \\ 1 & T_{ramp} < t < T_{tot} \end{cases} , \tag{4.52}$$

The rise-time was chosen as $T_{ramp} = 10\tau$ while the total simulation time was $T_{tot} = 25\tau$, where $\tau = \frac{2\pi}{\omega}$ denotes the optical cycle.

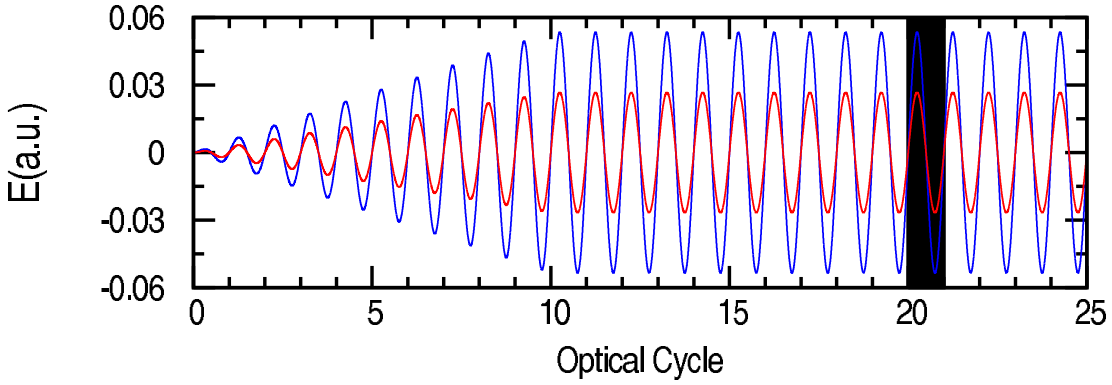

FIGURE 4.12: $\lambda = 228$ nm laser field, represented by $E(t) = E_0 f(t)\sin(\omega t)$, for two peak intensities, $I_1 = |E_0|^2 = 10^{14} W/\text{cm}^2$ and $I_2 = |E_0|^2 = 2.5 \times 10^{13} W/\text{cm}^2$. The envelope function $f(t)$ is chosen such that the field is linearly ramped from zero to its maximum strength at $t = 7.6$ fs and thereafter held constant. The highlighted area represents the optical cycle that will be focussed on in later graphs.

The same system and parameters were studied in Ref. [48] where the importance of electron-nuclear correlation was highlighted: a two-configuration correlated ansatz for the time-dependent electron-nuclear wavefunction was able to describe photodissociation processes in many cases, while a simple uncorrelated Hartree product of an electronic and a nuclear wavefunction almost always failed. In the present work we analyse the dynamics via the numerically exact TDPES, finding it very useful in understanding and interpreting the motion. We note that the laser-field does not couple directly to the nuclear relative coordinate R, but only indirectly via the TDPES.

We will compare the exact dynamics with the following three approximations: (i) the usual Ehrenfest approximation, where the nuclei are treated via classical dynamics, evolving under the force $-\nabla V_{Ehr} = -\nabla_{\underline{\underline{\mathbf{R}}}} W_{nn}(\underline{\underline{\mathbf{R}}}) - \int d\underline{\underline{\mathbf{r}}}\, n(\boldsymbol{r}, t) \nabla_{\underline{\underline{\mathbf{R}}}} W_{en}(\underline{\underline{\mathbf{r}}}, \underline{\underline{\mathbf{R}}})$, with $n(\boldsymbol{r}, t)$ being the one-body electron density , (ii) the "exact-Ehrenfest" approximation, which

N_R	ΔR (a_0)	R_{max} (a_0)	N_z	Δz (a_0)	$\lvert z_{max}\rvert$ (a_0)	Δt $(a.u)$
384	0.1	38.8	768	0.4	153.4	0.1

TABLE 4.2: Numerical parameters employed for the numerical simulations of the H_2^+ in $I_1 = 10^{14} W/\text{cm}^2$ and $I_2 = 2.5 \times 10^{13} W/\text{cm}^2$ laser fields.

substitutes the exact TDPES for the Ehrenfest potential V_{Ehr} in the usual Ehrenfest approach and, (iii) an uncorrelated approach, the time-dependent Hartree (self-consistent field) approximation, $\Psi_H(\underline{\mathbf{r}}, \underline{\underline{\mathbf{R}}}, t) = \phi(\underline{\mathbf{r}}, t)\chi(\underline{\underline{\mathbf{R}}}, t)$, where the electronic part does not depend on $\underline{\underline{\mathbf{R}}}$ at all. This includes a quantum treatment of the nuclei, but no electron-nuclear correlation.

For the numerical integration of the TDPES, we have used the parameters of table (4.2) that provide a very good convergence of the results.

4.3.1 High intensity: $I_1 = 10^{14} W/\text{cm}^2$

The exact TDPES, along with the corresponding nuclear density, $|\chi(R,t)|^2$, are plotted in Fig. 4.13 at six snapshots of time. The initial TDPES lies practically on top of the ground-state BO surface, plotted in all the snapshots for comparison.

The dissociation of the molecule is dramatically reflected in the exact TDPES, whose well flattens out, causing the nuclear density to spill to larger separations. Importantly, the tail of the TDPES alternately falls sharply and returns in correspondence with the field, letting the density out; the TDPES is the only potential acting on the nuclear system and transfers energy from the accelerated electron to the nuclei.

In Figure 4.14 we focus on six equally-spaced time snap-shots during the optical cycle shaded in Figure 4.12. The lower panel shows the TDPES, with its characteristic oscillations, along with the nuclear density as a function of the internuclear coordinate, $|\chi(R,t)|^2$. The upper panel shows a color map of the conditional electronic probability density, $|\Phi_R(x,t)|^2$, i.e. the probability of finding an electron at x at a fixed nuclear separation R. While at small internuclear distances (around and below the equilibrium separation) the electron remains localized in the middle between the two nuclei, at larger separations one clearly sees the preferential localization of the electron density near the two nuclei, i.e. on one side or the other. At even larger separations we see streaks of ionizing electron density in both directions. For the full story, we must multiply the

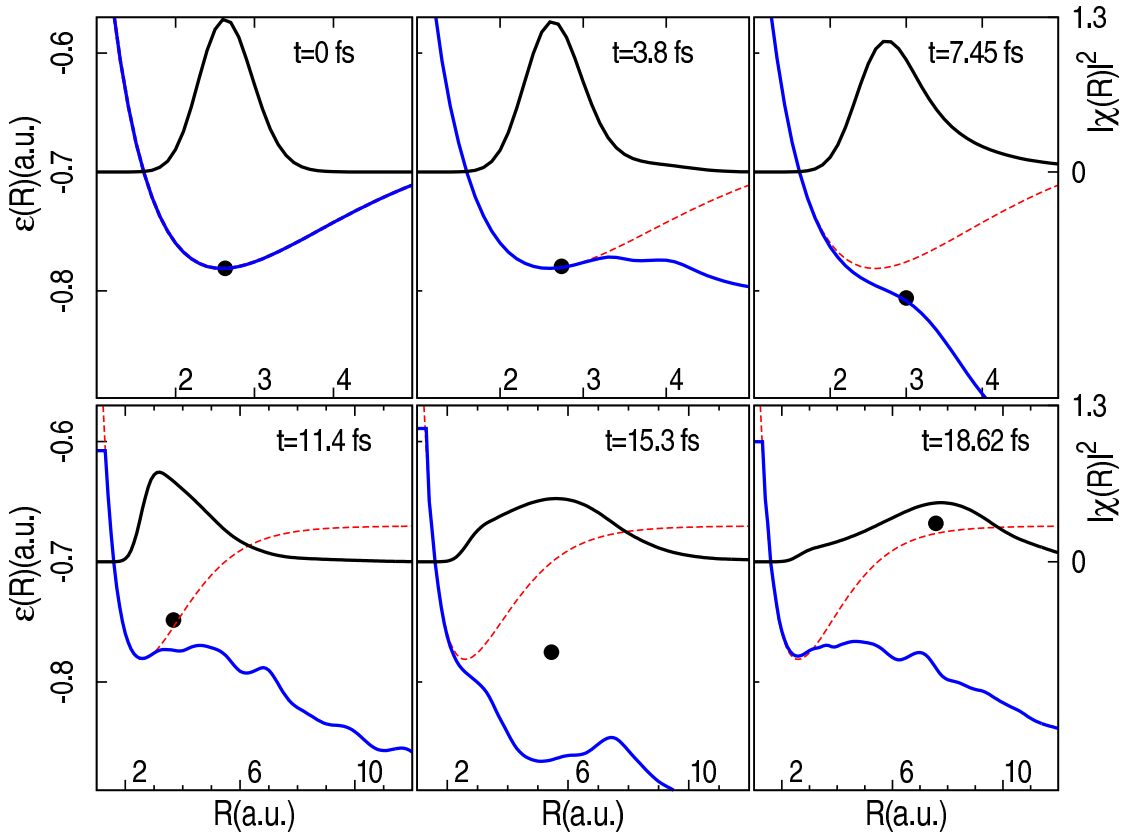

FIGURE 4.13: Snapshots of the TDPES (blue solid lines) and nuclear density (black solid lines) at times indicated, for the H_2^+ molecule subject to the laser-field with the peak intensity $I_1 = 10^{14}$W/cm^2. The solid circles indicate the position and energy of the classical particle in the exact-Ehrenfest calculation. For reference, the ground-state BO surface (red dashed lines) is shown.

conditional probability density of the upper panels with the nuclear density shown in the lower panel, to obtain the total electron-nuclear density; this is shown in Figure 4.15, indicating the probability of finding, at the time indicated, an electron at position x and the nuclear separation R.

The top left-hand panel of Fig. 4.16 shows the expectation value of the internuclear distance

$$< \hat{R} >= \langle \Psi(t) | \, \hat{R} \, | \Psi(t) \rangle \, , \tag{4.53}$$

along with the results from the three approximate methods described earlier. The lower left-hand panel shows the ionization probabilities. In principle, the latter requires projections of the full wavefunction on all continuum states which, in practice, are difficult to calculate. Alternatively, we use a geometrical concept [63], according to which the

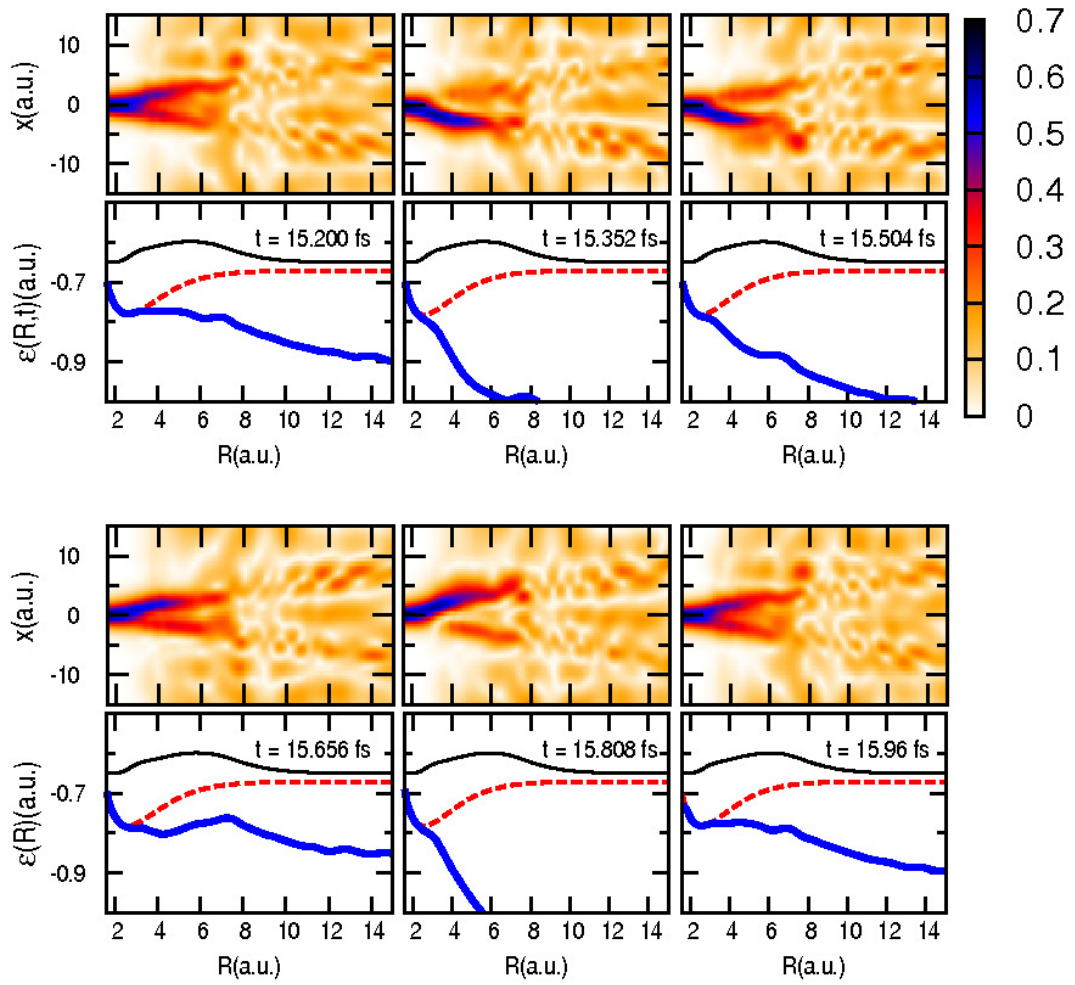

FIGURE 4.14: Snapshots of the TDPES (blue lines), nuclear density (black) and the electronic conditional-density (color map) at times indicated during an optical cycle, for the H_2^+ molecule subject to the laser-field with the peak intensity $I_1 = 10^{14}\mathrm{W/cm^2}$. For reference, the ground-state BO surface is shown as the red line.

total ionization probabilities can be obtained from

$$P_{ion}(t) = 1 - \int_{box_e} dx \left(\int dR |\Psi(t)|^2 \right). \tag{4.54}$$

The electrons leaving the "electronic analyzing box" (box_e) are thereby identified with ionized electrons. The ionization box here was chosen to be $|x| \leq 10$. The internuclear distance together with the ionization probability support a Coulomb-explosion interpretation of the dissociation: first, the system begins to ionize, then the nuclei begin to rapidly move apart under their mutual Coulomb repulsion increasingly sensed due to weaker screening by the reduced electron density. Turning now to the approximations, we observe that all the methods yield dissociation and some ionization. The expectation

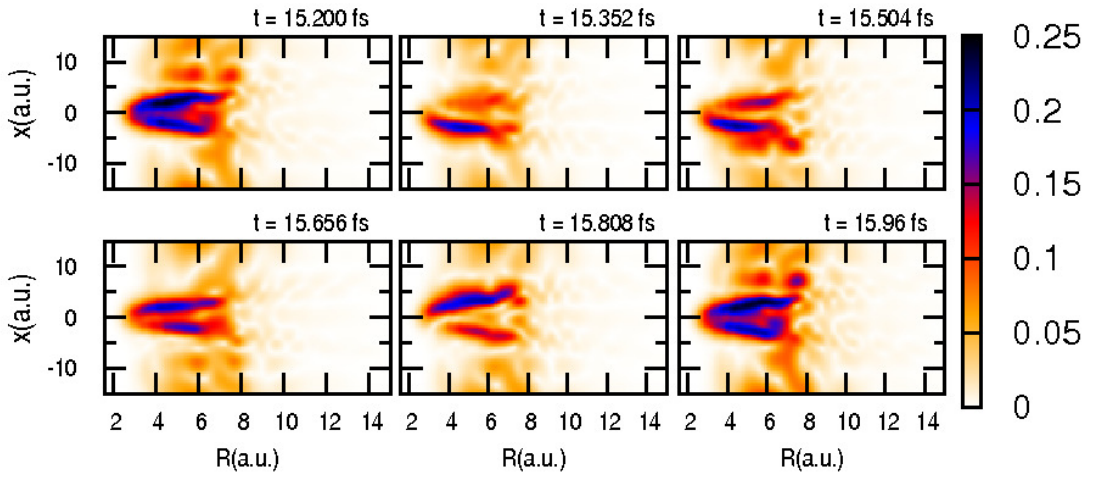

FIGURE 4.15: Snapshots of the total electron-nuclear density at times indicated during an optical cycle, for the H_2^+ molecule subject to the laser-field with the peak intensity $I_1 = 10^{14}\mathrm{W/cm}^2$.

value of the internuclear distance in Fig. 4.16, demonstrates that among all the approximate calculations employed here, the exact-Ehrenfest is most accurate. Referring back to Figure 4.13: the solid circles indicate the classical nuclear position and energy of a particle driven by the exact-Ehrenfest force. One can see that it rapidly picks up kinetic energy above the TDPES, supporting the fact that the nuclear dissociation mechanism is an essentially classical one in this case. The exact-Ehrenfest calculation even does better than TD-Hartree which treats the protons quantum mechanically, thus showing the overarching importance of electron-nuclear correlation in this case.

In fact, the Hartree description is worse than it may seem from just looking at the internuclear separation in Fig. 4.16. In Figure 4.17 we plot the time-dependent Hartree potential energy surface and Hartree nuclear-density. Both are dramatically different from the exact TDPES and exact nuclear density of Figure 4.13. At the initial time, the Hartree potential is reasonably good near equilibrium but poor at large separations [48]: this is a consequence of the conditional electron probability being independent of the nuclear coordinate, and therefore only yielding a realistic result where the energy is optimized, which is at equilibrium separation. As time evolves the minimum of the Hartree surface moves out and begins to widen, cradling the nuclear density, which more or less retains its Gaussian shape, unlike the exact density; only at larger times does the surface open out.

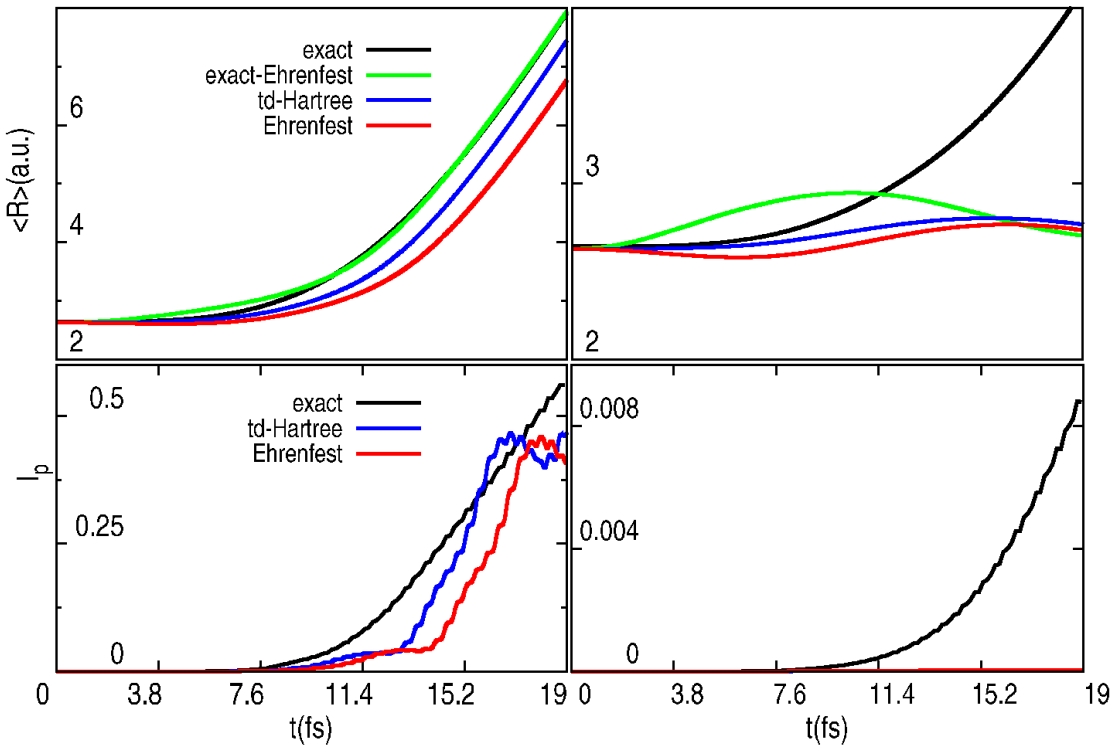

FIGURE 4.16: Dissociation and ionization for intensity I_1 (left) and I_2 (right). Top panels: the internuclear separation $\langle R \rangle(t)$. Lower panels: The ionization probability.

4.3.2 Lower intensity: $I_2 = 2.5 \times 10^{13} W/\text{cm}^2$

We now consider the dynamics under a field of weaker intensity. Figure 4.18 plots the TDPES, whose tail displays similar oscillations as in the higher intensity case. The nuclear density appears to leak out to larger separations, although more slowly than in the previous case; indeed from the right panels in Fig. 4.16, we see that the exact calculation leads to dissociation. However, Fig. 4.16 (upper right panel)also shows that none of the approximations dissociate, in contrast to the previous case. The Hartree and Ehrenfest methods also show negligible ionization, compared to the exact case; but even in the exact case the ionization probability is very small, indicating a different mechanism of dissociation than in the stronger field case. It may be at first surprising that the exact-Ehrenfest calculation does not dissociate the molecule, given that it is based on the exact TDPES, however an examination of classical dynamics in the TDPES of Fig. 4.13 can explain what is happening. The solid dot in Fig. 4.13 indicates the classical position and energy, and we see that it is always trapped inside a well in the TDPES, that remains at all times. This suggests that tunneling is the leading mechanism for the dissociation: a classical particle can only oscillate inside the well, while a quantum particle may tunnel

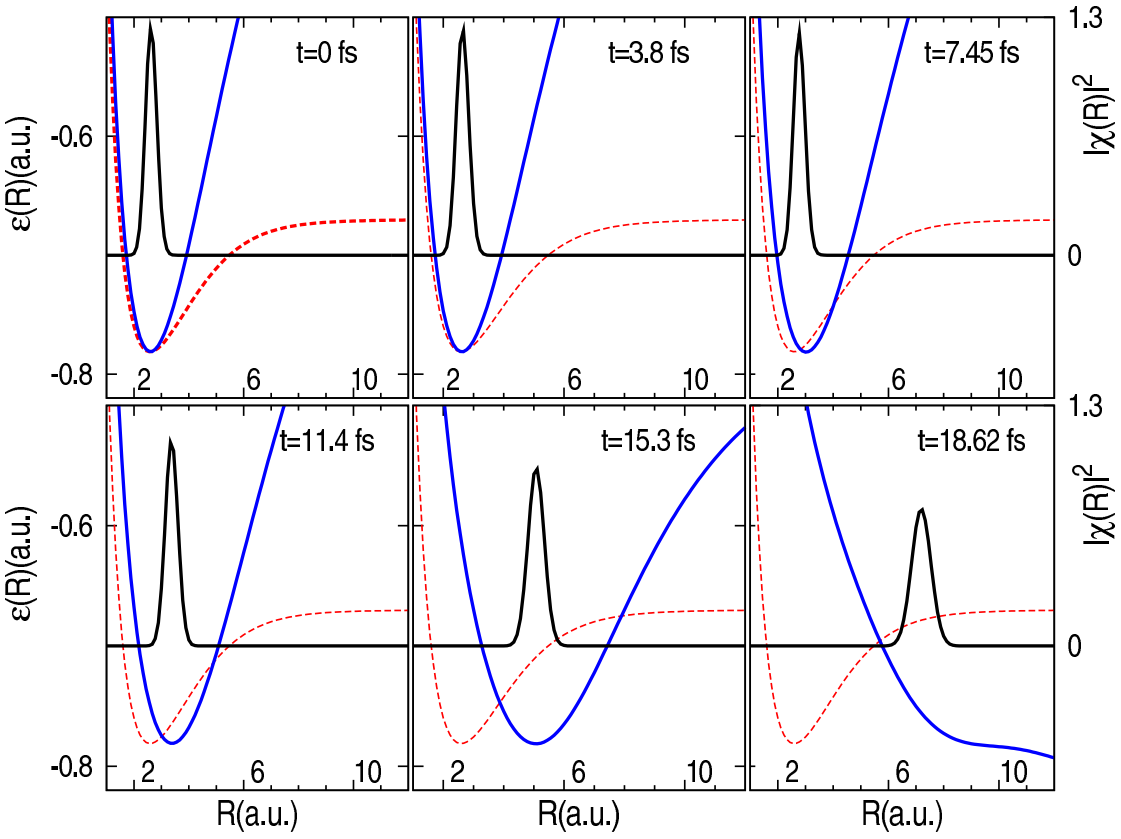

FIGURE 4.17: Snapshots of the time-dependent Hartree nuclear-potential (blue lines) and nuclear density (black) at times indicated, for the H_2^+ molecule subject to the laser-field with the peak intensity $I_1 = 10^{14}$W/cm^2. For reference, the ground-state BO surface is shown as the red line.

out, as indeed reflected in Fig. 4.16. Although the tail has similar oscillations as for I_1, this does not lead to dissociation of classical nuclei due to the barrier; the TDPES in this case transfers the field energy to the nuclei via tunneling. Although the exact-Ehrenfest calculation shows a larger amplitude of oscillation than the others, it ultimately cannot tunnel through the barrier.

As in the previous case, we plot in the top panels of Fig. 4.19 the electronic conditional density $|\Phi_R(x,t)|^2$ over one optical cycle, while the lower panels illustrate again the opening and closing of the TDPES as the field oscillates. Like in the previous case, for small R near equilibrium, the electron density is localized in between the nuclei, while for larger R, there is some polarization towards one side or the other. To get the full picture, one must multiply the top panels by the nuclear density $|\chi(R,t)|^2$, to obtain the total electron-nuclear probability density, shown in Figure 4.20. It is evident in this graph that there is much less ionization than in the previous case, and the dissociation is slower.

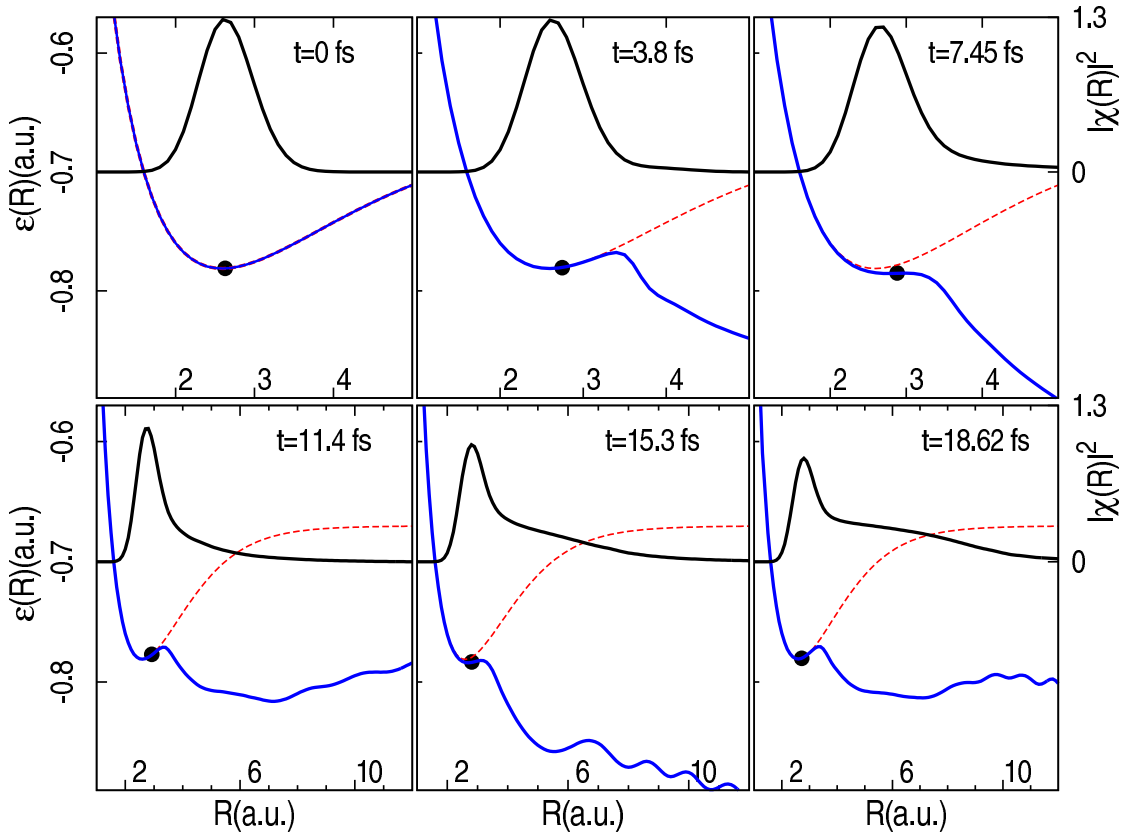

FIGURE 4.18: Snapshots of the TDPES (blue) and nuclear density (black) at times indicated, for the H_2^+ molecule subject to the laser-field with the peak intensity $I_2 = 2.5 \times 10^{13}$W/cm^2. The solid circles indicate the position and energy of the classical particle in the exact-Ehrenfest calculation. For reference, the ground-state BO surface (dashed red) is shown.

Although the Hartree approximation treats the nuclei quantum mechanically, and therefore allowing tunneling in principle, tunneling and dissociation do not actually occur. The reason for this is clear from the shape of the Hartree potential, plotted in Fig. 4.21: the Hartree potential essentially retains its initial shape at all times, making very small oscillations near the equilibrium separation. As in the more intense field case, this is due to its uncorrelated treatment of the electron-nuclear system: the electronic wavefunction at any nuclear configuration is always the same, and is best at equilibrium since initially it is determined by energy-optimization, from where it does not deviate far, due to the weak field strength. Unlike in the stronger field case, the Hartree surface never opens out. Dissociation via tunneling requires both a quantum mechanical description of the nuclei and an adequate accounting of electron-nuclear correlation.

We do not expect the TDPES to be so different from the BO surfaces in all cases. For example, in the case of field-free vibrational dynamics of the H2+ molecule, where we

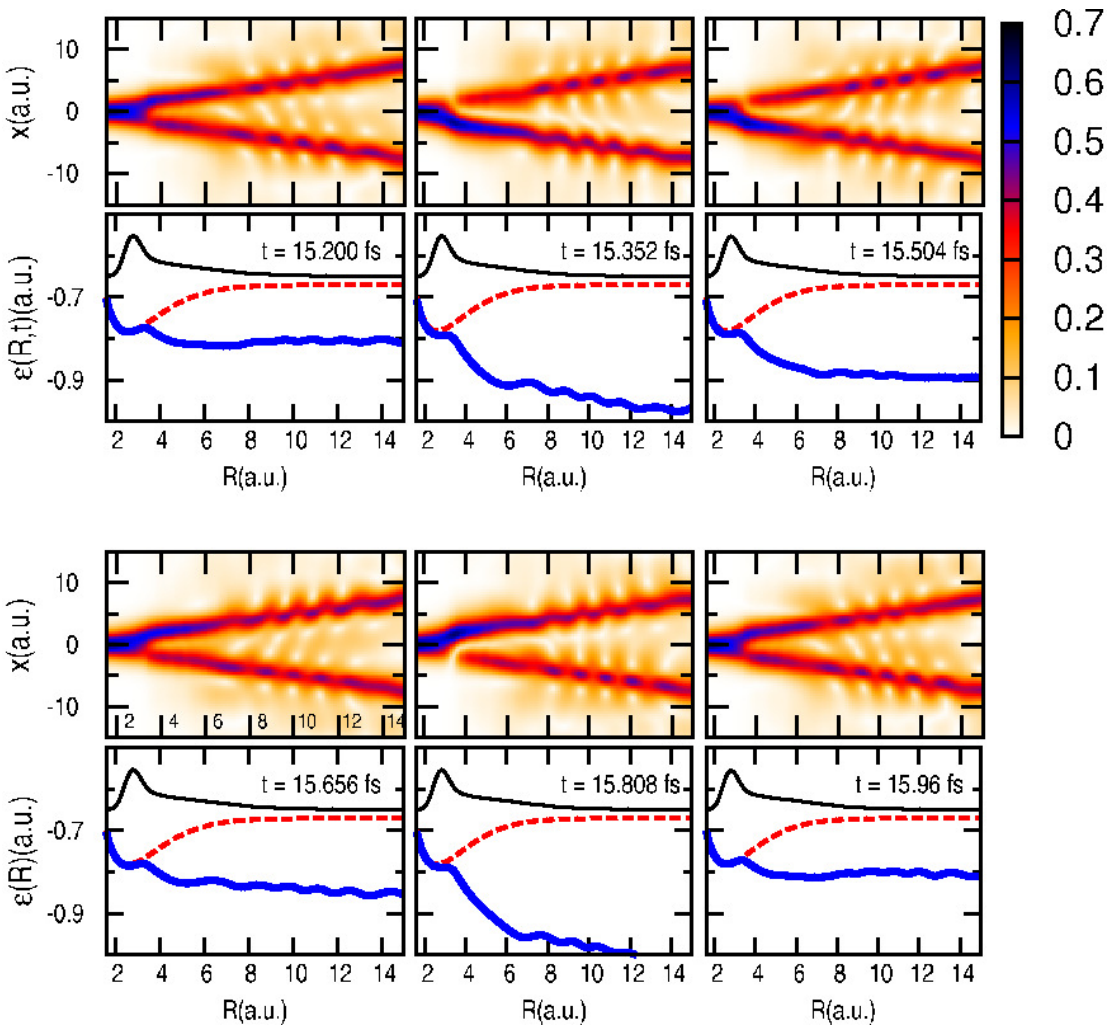

FIGURE 4.19: Snapshots of the TDPES (blue lines), nuclear density (black) and the electronic conditional-density (color map) at times indicated during an optical cycle, for the H_2^+ molecule subject to the laser-field with the peak intensity $I_2 = 2.5\times10^{13}$W/cm^2 . For reference, the ground-state BO surface is shown as the dashed red line.

start with a nuclear wavepacket displaced from equilibrium on the ground BO surface, we find the TDPES follows closely the BO surface throughout. The non-adiabatic couplings are weak in this case. The TDPES for field-free dynamics was discussed in (4.2).

The purpose of comparing the exact results with these methods (TD-Hartree, Ehrenfest and exact-Ehrenfest) was primarily to support the conclusions drawn from the exact TDPES regarding the dissociation mechanisms. An interesting question is how well do the more accurate approximate PES's proposed recently (e.g. Ref [64]) compare with the exact TDPES; this will be investigated in the future.

The example of the one-dimensional H_2^+ molecule in an oscillating electric field, presented here, demonstrates that the TDPES is a powerful tool to analyze and interpret different

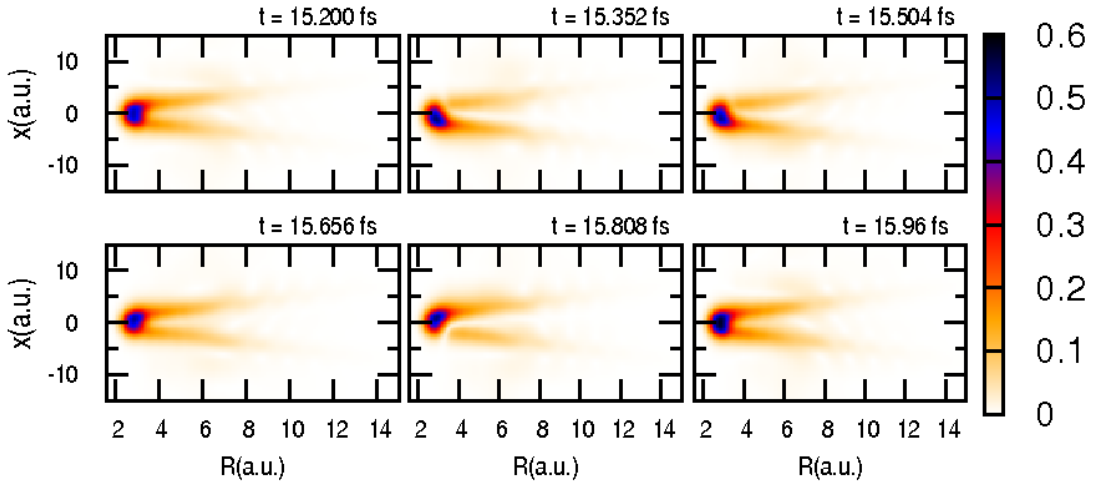

FIGURE 4.20: Snapshots of the total electron-nuclear density at times indicated during an optical cycle, for the H_2^+ molecule subject to the laser-field with the peak $I_2 = 2.5 \times 10^{13}\mathrm{W/cm^2}$.

types of dissociation processes. By studying the shape and evolution of the TDPES, comparing classical dynamics in this exact potential to the exact quantum dynamics, we were able to distinguish whether the dissociation proceeded via nuclear tunneling or more directly in Coulomb-explosion. For this example, the TDPES is the only potential determining the nuclear dynamics, exactly containing the coupling with electronic dynamics. The example demonstrates the importance of capturing both quantum effects in nuclear motion and electron-nuclear coupling; the Hartree approach, for example, despite treating the nuclei quantum mechanically, was unable to capture dissociation via tunneling as the shape of its potential surface was completely wrong.

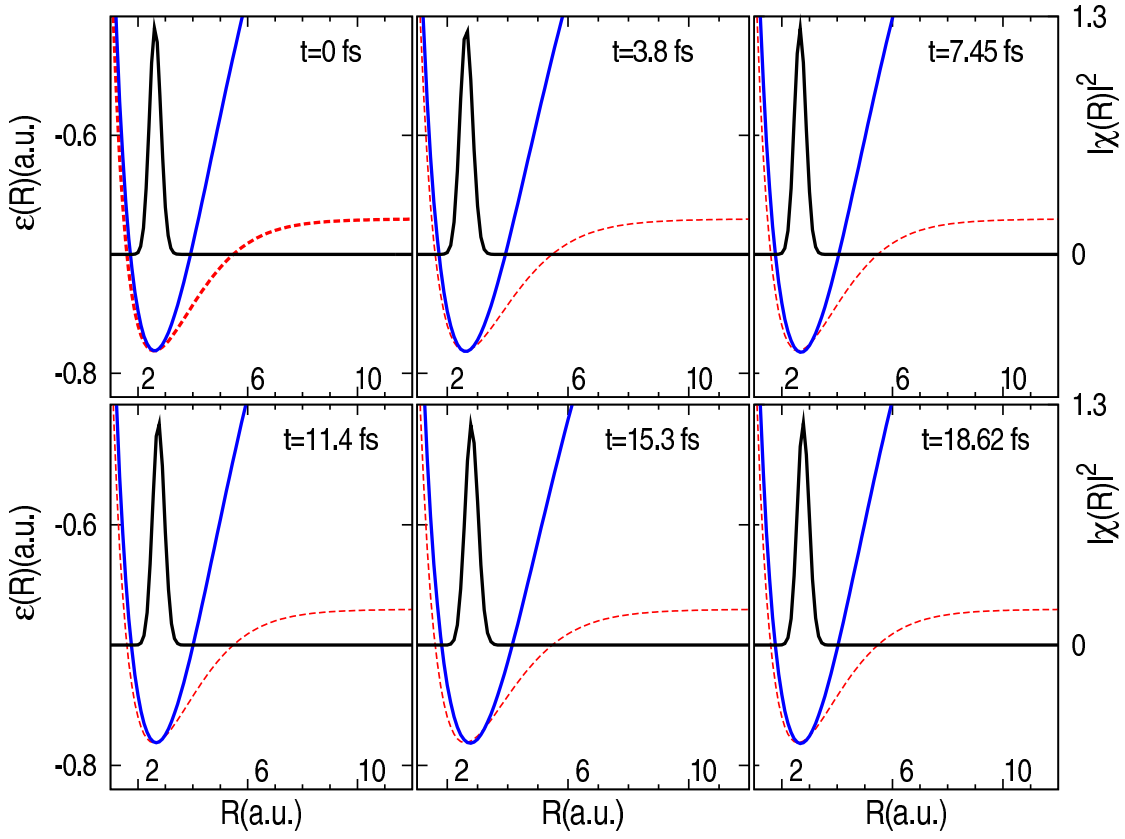

FIGURE 4.21: Snapshots of the time-dependent Hartree nuclear-potential (blue lines) and nuclear density (black) at times indicated, for the H_2^+ molecule subject to the laser-field with the peak intensity $I_1 = 10^{14}\mathrm{W/cm^2}$ $I_2 = 2.5 \times 10^{13}\mathrm{W/cm^2}$. For reference, the ground-state BO surface is shown as the dashed red line.

Chapter 5

Mixed quantum-classical scheme

The theoretical description of molecular processes that involve electronic non-adiabatic transitions is a major challenge. Solving the time-dependent Schrödinger equation (2.11) is a computational task that stretches the capacity of today's computers to their limits already for very simple molecules, containing only a few degrees of freedom such as H_2^+. Therefore, there is a need to develop efficient and at the same time accurate methods to approximately describe the dynamical processes. The idea of combining classical description of the nuclear degrees of freedom with the quantum dynamics of electrons has led to a huge variety of methods to study non-adiabatic processes [62, 65–82]. The main issues in developing a mixed quantum-classical (MQC) procedure to study the coupled electron-nuclear dynamics can be identified as

(i) the decomposition of electronic and nuclear motions,

(ii) the representation of the back reaction of quantum transitions on the classical motion.

In most of the existing methods, the approximations are introduced in a very early stage with decomposing the full system into a subsystem that is treated classically and a part that requires quantum treatment. The approximate decomposition of the full system to classical and quantum subsystems makes it very difficult to account for the quantum back reaction on the classical motion.

With the theoretical framework, presented in Chapter (2), and the numerical study of Chapter (3) and (4), we set the stage for developing systematic and controlled approximations. Here, as the last curtain of this thesis we present a mixed quantum-classical

scheme, based on the exact decomposition of the electronic and nuclear motions (2). This is indeed the beginning of a new path towards a full ab initio treatment of the coupled electron-nuclear dynamics.

In this chapter, we first represent the exact equations (2.29-2.34) in terms of the BO states. Then we discuss the classical limit of the nuclear motion and introduce the consecutive approximations in the exact equations that leads to a mixed quantum-classical scheme. We further show the performance of the scheme by presenting some numerical results in comparison with the exact quantum dynamics. At the end, we provide a detailed investigation of the classical approximation and its consequences.

5.1 Exact equations in adiabatic representation

In this section we express the exact equations (2.29-2.34) in terms of the BO basis but first we summarize the exact factorization of electronic and nuclear dynamics, presented in chapter (2). Ultimately, we are interested in the classical treatment of the nuclear motion that is achieved by taking $\hbar \to 0$ limit in a semi-classical expansion of the nuclear wave-function. Therefore, in order to get the $\hbar$ back in our equations we leave the realm of atomic units.

In chapter (2) we have proved that, $\Psi(\underline{\mathbf{r}}, \underline{\underline{\mathbf{R}}}, t)$, the exact solution of the TDSE (2.11) can be exactly factorized and written as a single product of the nuclear wave-function, $\chi(\underline{\underline{\mathbf{R}}}, t)$, and the electronic wave-function, $\Phi_{\underline{\underline{\mathbf{R}}}}(\underline{\mathbf{r}}, t)$,

$$\Psi(\underline{\mathbf{r}}, \underline{\underline{\mathbf{R}}}, t) = \chi(\underline{\underline{\mathbf{R}}}, t)\Phi_{\underline{\underline{\mathbf{R}}}}(\underline{\mathbf{r}}, t), \tag{5.1}$$

where $\Phi_{\underline{\underline{\mathbf{R}}}}(\underline{\mathbf{r}}, t)$ satisfies the PNC,

$$\int d\underline{\mathbf{r}} \left|\Phi_{\underline{\underline{\mathbf{R}}}}(\underline{\mathbf{r}}, t)\right|^2 = 1 \quad \forall \ \underline{\underline{\mathbf{R}}}, t. \tag{5.2}$$

The time evolution of $\Phi_{\underline{\underline{\mathbf{R}}}}(\underline{\mathbf{r}}, t)$ and $\chi(\underline{\underline{\mathbf{R}}}, t)$ are governed by

$$\Big(\hat{H}_{el}(\underline{\mathbf{r}}, \underline{\underline{\mathbf{R}}}, t) - \epsilon(\underline{\underline{\mathbf{R}}}, t)\Big)\Phi_{\underline{\underline{\mathbf{R}}}}(\underline{\mathbf{r}}, t) = i\,\hbar\,\partial_t \Phi_{\underline{\underline{\mathbf{R}}}}(\underline{\mathbf{r}}, t), \tag{5.3}$$

and

$$\Big(\sum_{\alpha=1}^{N_n} \frac{1}{2M_\alpha}(-i\hbar\nabla_\alpha + \mathbf{A}_\alpha(\underline{\underline{\mathbf{R}}}, t))^2 + \hat{V}_n^{ext}(\underline{\underline{\mathbf{R}}}, t) + \epsilon(\underline{\underline{\mathbf{R}}}, t)\Big)\chi(\underline{\underline{\mathbf{R}}}, t) = i\,\hbar\,\partial_t \chi(\underline{\underline{\mathbf{R}}}, t), \tag{5.4}$$

where the electronic Hamiltonian is

$$\hat{H}_{el}(\underline{\underline{\mathbf{r}}},\underline{\underline{\mathbf{R}}},t)=\hat{H}_{BO}(\underline{\underline{\mathbf{r}}},\underline{\underline{\mathbf{R}}},t)+\hat{V}_{e}^{ext}(\underline{\underline{\mathbf{r}}},t)+\hat{U}_{en}^{coup}\left[\Phi_{\underline{\underline{\mathbf{R}}}},\chi\right]. \tag{5.5}$$

The electron-nuclear coupling operator, $\hat{U}_{en}^{coup}\left[\Phi_{\underline{\underline{\mathbf{R}}}},\chi\right]$,

$$\hat{U}_{en}^{coup}\left[\Phi_{\underline{\underline{\mathbf{R}}}},\chi\right]=\sum_{\alpha=1}^{N_n}\frac{1}{M_\alpha}\Big[\frac{(-i\hbar\nabla_\alpha-\mathbf{A}_\alpha(\underline{\underline{\mathbf{R}}},t))^2}{2}+\Big(\frac{-i\hbar\nabla_\alpha\chi}{\chi}+\mathbf{A}_\alpha(\underline{\underline{\mathbf{R}}},t)\Big)\cdot\big(-i\hbar\nabla_\alpha-\mathbf{A}_\alpha(\underline{\underline{\mathbf{R}}},t)\big)\Big] \tag{5.6}$$

in the electronic equation (5.3), the scalar potential,

$$\epsilon(\underline{\underline{\mathbf{R}}},t)=\left\langle\Phi_{\underline{\underline{\mathbf{R}}}}(t)\right|\hat{H}_{el}((\underline{\underline{\mathbf{r}}},\underline{\underline{\mathbf{R}}},t)-i\hbar\partial_t\left|\Phi_{\underline{\underline{\mathbf{R}}}}(t)\right\rangle_{\underline{\underline{\mathbf{r}}}}, \tag{5.7}$$

and the vector potential,

$$\mathbf{A}_\alpha(\underline{\underline{\mathbf{R}}},t)=\left\langle\Phi_{\underline{\underline{\mathbf{R}}}}(t)\right|-i\hbar\nabla_\alpha\Phi_{\underline{\underline{\mathbf{R}}}}(t)\Big\rangle_{\underline{\underline{\mathbf{r}}}}, \tag{5.8}$$

in both equations (5.3 and 5.3), mediate the coupling between electronic and nuclear motions in a formally exact way.

As the first step, towards developing a practical and accurate method to deal with real systems, we represent the electronic equation (5.3) in terms of the BO electronic basis $\{\phi^j_{\underline{\underline{\mathbf{R}}}}(\underline{\underline{\mathbf{r}}})\}$ by using the expression of the electronic wave-function, $\Phi_{\underline{\underline{\mathbf{R}}}}(\underline{\underline{\mathbf{r}}},t)$, in terms of the BO electronic basis (2.63):

$$\hat{H}_{el}(\underline{\underline{\mathbf{r}}},\underline{\underline{\mathbf{R}}},t)\sum_j C_j(\underline{\underline{\mathbf{R}}},t)\phi^j_{\underline{\underline{\mathbf{R}}}}(\underline{\underline{\mathbf{r}}})=i\hbar\sum_j\left(\partial_t C_j(\underline{\underline{\mathbf{R}}},t)\right)\phi^j_{\underline{\underline{\mathbf{R}}}}(\underline{\underline{\mathbf{r}}}), \tag{5.9}$$

multiply both sides of the equation by $\phi^{k*}_{\underline{\underline{\mathbf{R}}}}(\underline{\underline{\mathbf{r}}})$ and integrating over the electronic coordinates. These, after some straightforward algebra, lead to an infinite set of partial differential equations for the coefficients, $C_j(\underline{\underline{\mathbf{R}}},t)$,

$$\dot{C}_j(\underline{\underline{\mathbf{R}}},t)=f\left(\{C_k(\underline{\underline{\mathbf{R}}},t)\},\{\nabla_{\underline{\underline{\mathbf{R}}}}C_k(\underline{\underline{\mathbf{R}}},t)\},\{\nabla^2_{\underline{\underline{\mathbf{R}}}}C_k(\underline{\underline{\mathbf{R}}},t)\}\right), \tag{5.10}$$

where $k=1,\ldots,j,\ldots$ and f is a function of the coefficients and their spatial derivatives at the space-time point $(\underline{\underline{\mathbf{R}}},t)$. In deriving the explicit form of the equations that determine the evolution of the expansion coefficients, $C_j(\underline{\underline{\mathbf{R}}},t)$, we act with the Hamiltonian operator, $\hat{H}_{el}$, on the expansion (2.63). The most complicated part of the action, comes

from acting with the electron-nuclear coupling operator (5.6) on the expansion (2.63). Before performing the action, we rewrite $\hat{U}_{en}^{corr}$ as

$$\begin{aligned}\hat{U}_{en}^{corr} &= \sum_{\alpha=1}^{N_n}\frac{1}{2M_\alpha}\Big[-\hbar^2\nabla_\alpha^2 + i\hbar\nabla_\alpha\cdot\mathbf{A}_\alpha + 2i\hbar\mathbf{A}_\alpha\cdot\nabla_\alpha + \mathbf{A}_\alpha^2 \\ &+ 2\Big(\frac{-i\hbar\nabla_\alpha\chi}{\chi} + \mathbf{A}_\alpha(\underline{\underline{\mathbf{R}}},t)\Big)\cdot\Big(-i\hbar\nabla_\alpha - \mathbf{A}_\alpha(\underline{\underline{\mathbf{R}}},t)\Big)\Big]. \end{aligned} \tag{5.11}$$

Then, we use the relations,

$$\begin{aligned}\nabla_\alpha\Phi_{\underline{\underline{\mathbf{R}}}}(\underline{\mathbf{r}},t) &= \sum_{j=1}^{\infty}\big(\nabla_\alpha C_j\big)\phi^j_{\underline{\underline{\mathbf{R}}}} + C_j\big(\nabla_\alpha\phi^j_{\underline{\underline{\mathbf{R}}}}\big) \\ \nabla_\alpha^2\Phi_{\underline{\underline{\mathbf{R}}}}(\underline{\mathbf{r}},t) &= \sum_{j}\big(\nabla_\alpha^2 C_j\big)\,\phi^j_{\underline{\underline{\mathbf{R}}}} + C_j\nabla_\alpha^2\phi^j_{\underline{\underline{\mathbf{R}}}} + 2\nabla_\alpha C_j\cdot\nabla_\alpha\phi^j_{\underline{\underline{\mathbf{R}}}}\end{aligned} \tag{5.12}$$

and perform the action

$$\begin{aligned}\hat{U}_{en}^{corr}\Phi_{\underline{\underline{\mathbf{R}}}} &= \sum_{\alpha=1}^{N_n}\frac{1}{2M_\alpha}\Big(\sum_j\phi^j_{\underline{\underline{\mathbf{R}}}}\Big[-\hbar^2\nabla_\alpha^2 + i\hbar\nabla_\alpha\cdot\mathbf{A}_\alpha + 2i\hbar\mathbf{A}_\alpha\cdot\nabla_\alpha + \mathbf{A}_\alpha^2 \\ &+ 2\Big(\frac{-i\hbar\nabla_\alpha\chi}{\chi} + \mathbf{A}_\alpha\Big)\cdot\big(-i\hbar\nabla_\alpha - \mathbf{A}_\alpha\big)\Big]C_j(\underline{\underline{\mathbf{R}}},t) \\ &+ C_j(\underline{\underline{\mathbf{R}}},t)\Big[-\hbar^2\nabla_\alpha^2 + 2i\hbar\mathbf{A}_\alpha\cdot\nabla_\alpha + 2\Big(\frac{-i\hbar\nabla_\alpha\chi}{\chi} + \mathbf{A}_\alpha\Big)\cdot\big(-i\hbar\nabla_\alpha\big)\Big]\phi^j_{\underline{\underline{\mathbf{R}}}} \\ &- 2\hbar^2\nabla_\alpha C_j(\underline{\underline{\mathbf{R}}},t)\cdot\nabla_\alpha\phi^j_{\underline{\underline{\mathbf{R}}}}\Big)\end{aligned} \tag{5.13}$$

that can be written in a more compact form:

$$\begin{aligned}\hat{U}_{en}^{corr}\Phi_{\underline{\underline{\mathbf{R}}}} = \sum_j\phi^j_{\underline{\underline{\mathbf{R}}}}\hat{U}_{en}^{corr}C_j &+ \sum_{\alpha=1}^{N_n}\frac{1}{2M_\alpha}\Big(C_j\Big[-\hbar^2\nabla_\alpha^2 + 2\Big(\frac{-i\hbar\nabla_\alpha\chi}{\chi}\Big)\cdot\big(-i\hbar\nabla_\alpha\big)\Big]\phi^j_{\underline{\underline{\mathbf{R}}}} \\ &- 2\hbar^2\nabla_\alpha C_j\cdot\nabla_\alpha\phi^j_{\underline{\underline{\mathbf{R}}}}\Big).\end{aligned} \tag{5.14}$$

Therefore, Eq. (5.10), is explicitly written as

$$\Big[\epsilon^j_{BO} + \hat{U}_{en}^{corr} - \epsilon(\underline{\underline{\mathbf{R}}},t)\Big]C_j + \sum_k\Big[H^c_{jk} - \sum_\alpha^{N_n}\Big(\Lambda^{BO}_{kj,\alpha}(\underline{\underline{\mathbf{R}}}) + \frac{1}{M_\alpha}\frac{i\hbar\nabla_\alpha\chi}{\chi}\cdot\mathcal{F}^\alpha_{jk}\Big)\Big]C_k = i\hbar\partial_t C_j \tag{5.15}$$

where

$$H^c_{jk} = \langle\phi^j_{\underline{\underline{\mathbf{R}}}}|\hat{V}^e_{\text{ext}}|\phi^k_{\underline{\underline{\mathbf{R}}}}\rangle_{\underline{\mathbf{r}}} \tag{5.16}$$

and the terms

$$\Lambda^{BO}_{kj,\alpha}(\underline{\underline{\mathbf{R}}}) = \frac{1}{2M_\alpha}\Big[\mathcal{G}^{BO}_{kj,\alpha}(\underline{\underline{\mathbf{R}}}) + 2\mathcal{F}^{BO}_{kj,\alpha}(\underline{\underline{\mathbf{R}}})\cdot(i\hbar\nabla_\alpha)\Big] \tag{5.17}$$

are called the "nonadiabatic couplings", defined also in (2.1.2),

$$\mathcal{F}^{BO}_{kj,\alpha}(\underline{\underline{\mathbf{R}}}) = -i\hbar < \phi^{k}_{\underline{\underline{\mathbf{R}}}\ \underline{\sigma}} | \nabla_\alpha \phi^{j}_{\underline{\underline{\mathbf{R}}}\ \underline{\sigma}} >$$
$$\mathcal{G}^{BO}_{kj,\alpha}(\underline{\underline{\mathbf{R}}}) = \hbar^2 < \phi^{k}_{\underline{\underline{\mathbf{R}}}\ \underline{\sigma}} | \nabla^2_\alpha \phi^{j}_{\underline{\underline{\mathbf{R}}}\ \underline{\sigma}} > . \tag{5.18}$$

The TDPES, $\epsilon(\underline{\underline{\mathbf{R}}}, t)$, and the time-dependent vector potential, $\mathbf{A}_\alpha(\underline{\underline{\mathbf{R}}}, t)$, in (5.15) are expressed in terms of the BO states as shown in (2.68) and (2.66).

As mentioned previously, the dynamics of $\chi(\underline{\underline{\mathbf{R}}}, t)$ and $\Phi_{\underline{\underline{\mathbf{R}}}}(\underline{\mathbf{r}}, t)$ are determined by Eqs. (5.3) and (5.4) uniquely, up to within a gauge. Therefore, in order to make approximations, the gauge freedom must be fixed. Here, a suitable way of fixing the gauge is to set the GI part of the TDPES to zero, i.e.,

$$\left\langle \Phi_{\underline{\underline{\mathbf{R}}}}(t) | i\,\hbar\,\partial_t \Phi_{\underline{\underline{\mathbf{R}}}}(t) \right\rangle_{\underline{\mathbf{r}}} = 0, \tag{5.19}$$

that in terms of the BO basis is expressed as

$$i\hbar \sum_j C^*_j(\underline{\underline{\mathbf{R}}}, t) \partial_t C_j(\underline{\underline{\mathbf{R}}}, t) = 0. \tag{5.20}$$

So far, we have expressed the exact equations and the gauge condition (5.20) in terms of the BO basis, without introducing any approximation. In the following section, we turn to view the nuclei as classical point-like particles and based on that develop a MQC scheme.

5.2 Classical limit of the nuclear motion

It was shown in (2.3.1) and emphasized throughout this work that $\chi(\underline{\underline{\mathbf{R}}}, t)$ that satisfies (5.4) leads to a nuclear N-body density and a nuclear N-body current density, hence, can be viewed as the proper nuclear wave-function. Using the Ehrenfest theorem (4.2.5), we have also proved that this wave-function reproduces the mean nuclear position and momentum of the complete electron-nuclear system. The time evolution of $\chi(\underline{\underline{\mathbf{R}}}, t)$, on the other hand, is completely determined by a *single* PES, $\epsilon(\underline{\underline{\mathbf{R}}}, t)$, and a *single* vector potential, $\mathbf{A}_\nu(\underline{\underline{\mathbf{R}}}, t)$, that are *unique* up to within a gauge transformation (2.47) and the exact coupling to the electronic motion is taken care of by the electron-nuclear coupling operator (5.6) in the electronic equation (5.3). Therefore, Eqs. (5.3) and (5.4), offer a promising starting point to develop systematic approximations.

Here, we develop a MQC scheme by taking the classical limit of the nuclear motion in (5.3) and (5.4). Since we have started from the full quantum description of nuclear dynamics that is coupled to the electronic dynamics, we may view this approximation from the nuclear wave-function perspective. The nuclear wave-function, without loss of generality and as discussed in [83], maybe written as

$$\chi(\underline{\underline{\mathbf{R}}}, t) = e^{\frac{i}{\hbar}\mathcal{S}(\underline{\underline{\mathbf{R}}}, t)}, \tag{5.21}$$

with the assumption that the complex function $\mathcal{S}(\underline{\underline{\mathbf{R}}}, t)$ can be expanded as an asymptotic series in powers of $\hbar$,

$$\mathcal{S}(\underline{\underline{\mathbf{R}}}, t) = \sum_{\alpha} \hbar^{\alpha} S_{\alpha}(\underline{\underline{\mathbf{R}}}, t). \tag{5.22}$$

Inserting Eq. (5.21) in Eq. (5.4) and keeping the terms only up to within $\mathcal{O}(\hbar^0)$ leads to

$$-\partial_t S_0(\underline{\underline{\mathbf{R}}}^c, t) = H_n\left(\underline{\underline{\mathbf{R}}}, \left\{\nabla_\nu S_0(\underline{\underline{\mathbf{R}}}^c, t)\right\}_{\nu=1,N_n}, t\right) \tag{5.23}$$

that gives the classical limit of the nuclear dynamics as the zero-th order $\hbar$ expansion of the nuclear wave-function, if $S_0(\underline{\underline{\mathbf{R}}}, t)$ is the classical action. Here,

$$\underline{\underline{\mathbf{R}}}^c(t) = (\boldsymbol{R}_1^c(t) ... \boldsymbol{R}_{N_n}^c(t)), \tag{5.24}$$

is the classical path along which the action, $S_0(\underline{\underline{\mathbf{R}}}^c(t))$, is stationary and $\nabla_\nu S_0$ is the conjugate momenta,

$$\mathbf{P}_\nu^c = \nabla_\nu S_0, \tag{5.25}$$

associated to the ν-th nucleus and evaluated along the classical trajectory and Eq. (5.23) is the Hamilton-Jacobi equation [84]. The classical evolution is, therefore, generated by the classical Hamiltonian

$$H_n = \sum_{\nu=1}^{N_n} \frac{\left|\mathbf{P}_\nu^c + \mathbf{A}_\nu(\underline{\underline{\mathbf{R}}}^c(t))\right|^2}{2M_\nu} + \epsilon(\underline{\underline{\mathbf{R}}}^c, t), \tag{5.26}$$

and the canonical momentum, as in the case of a classical charge moving in an electromagnetic field, is

$$M_\nu \mathbf{V}_\nu = \mathbf{P}_\nu^c + \mathbf{A}_\nu(\underline{\underline{\mathbf{R}}}^c(t)). \tag{5.27}$$

Employing Hamilton's equation of motion and after some algebra we arrive at the classical equation of motion,

$$M_\nu \dot{\mathbf{V}}_\nu = \mathbf{E}_\nu + \sum_{\nu'\nu} \mathbf{F}_{\nu\nu'}, \tag{5.28}$$

that determines the classical trajectory [85]. Here,

$$\mathbf{E}_\nu = -\nabla_\nu \epsilon + \partial_t \mathbf{A}_\nu, \tag{5.29}$$

is an *electric-like field* and

$$\begin{aligned} \mathbf{F}_{\nu\nu'}(\underline{\underline{\mathbf{R}}}^c) &= -\mathbf{V}_{\nu'} \times \mathbf{B}_{\nu\nu'}(\underline{\underline{\mathbf{R}}}^c) \\ &+ \left[(\mathbf{V}_{\nu'} \cdot \nabla_{\nu'})\, \mathbf{A}_\nu(\underline{\underline{\mathbf{R}}}^c) - (\mathbf{V}_{\nu'} \cdot \nabla_\nu)\, \mathbf{A}_{\nu'}(\underline{\underline{\mathbf{R}}}^c) \right] , \end{aligned} \tag{5.30}$$

contains a *generalized magnetic-like field*,

$$\mathbf{B}_{\nu\nu'}(\underline{\underline{\mathbf{R}}}^c) = \nabla_\nu \times \mathbf{A}_{\nu'}(\underline{\underline{\mathbf{R}}}^c), \tag{5.31}$$

and together with (5.29) gives the *generalized Lorentz force*,

$$\mathbf{F}^g_\nu = \mathbf{E} + \sum_{\nu'\nu} \mathbf{F}_{\nu\nu'}, \tag{5.32}$$

that influences the nucleus ν and couples its motion to the motion of all the other nuclei via the time-dependent vector potential (5.40) and the nuclear velocities. The effect of the electric-like field, the first term in (5.32), on the classical trajectory is clear. In order to understand the effect of the second term of the generalized Lorentz force (5.32), we recall a discussion in (2.3.1) stating that the vector potential is the difference of paramagnetic nuclear velocity fields derived from the full and nuclear wavefunctions. In the classical treatment of the nuclear degrees of freedom, what we call a generalized magnetic-field is actually the *generalized vorticity* of this difference which now is $\mathbf{A}_\nu(\underline{\underline{\mathbf{R}}}^c(t))$. The vector potential, $\mathbf{A}_\nu(\underline{\underline{\mathbf{R}}}^c(t))$, that explicitly expresses the coupling between electrons and nuclei as the variation of the electronic wavefunction in terms of the nuclear displacement, contributes to an effective inter-nuclear force. These are referred to as *current-induced forces* that have been observed experimentally [86, 87] and attracted extensive theoretical attention [88–95] due to the importance of the interplay between electronic and mechanical (nuclear) degrees of freedom in nanoelectromechanical systems (NEMS).

Note that Eq. (A.12) is derived by acting with the gradient operator, ∇_ν, on Eq. (5.23) and using the hydrodynamic time derivative,

$$d/dt = \partial_t + \sum_{\nu'} \mathbf{V}_{\nu'} \cdot \nabla_{\nu'}. \tag{5.33}$$

The full derivation of the equation (A.12) is presented in an appendix.

Now we approximate the nuclear wavefunction that appears explicitly in the electronic Hamiltonian (5.3) by its classical expression that is derived using (5.21),

$$\frac{-i\hbar\nabla_\nu\chi}{\chi} = \nabla_\nu S_0 + \mathcal{O}(\hbar), \tag{5.34}$$

up to within the zero-th order terms in $\hbar$,

$$\frac{-i\hbar\nabla_\nu\chi}{\chi} \to \mathbf{P}^c_\nu, \tag{5.35}$$

and we assume that in the classical limit, the spatial derivatives of the expansion coefficients, C_j, are zero, i.e.,

$$\begin{aligned} \nabla_\nu C_j(\underline{\underline{\mathbf{R}}}^c(t)) &= 0 \\ \nabla^2_\nu C_j(\underline{\underline{\mathbf{R}}}^c(t)) &= 0. \end{aligned} \tag{5.36}$$

This will be proved in section (5.3). For the sake of simplicity, we further consider that the BO states, ϕ^j_R, are real and introduce new forms of non-adiabatic couplings

$$\mathbf{d}^{(1)}_{jl,\alpha} = \langle \varphi^{(j)}_{\underline{\underline{\mathbf{R}}}} | \nabla_{\underline{\underline{\mathbf{R}}}} \varphi^{(l)}_{\underline{\underline{\mathbf{R}}}} \rangle_{\underline{\mathbf{r}}} = i\mathcal{F}^{BO}_{jl,\alpha} \tag{5.37}$$

and

$$d^{(2)}_{jl,\alpha} = \langle \nabla_{\underline{\underline{\mathbf{R}}}} \varphi^{(j)}_{\underline{\underline{\mathbf{R}}}} | \nabla_{\underline{\underline{\mathbf{R}}}} \varphi^{(l)}_{\underline{\underline{\mathbf{R}}}} \rangle_{\underline{\mathbf{r}}} = i\nabla_\alpha \cdot \mathcal{F}^{BO}_{jl,\alpha} - \mathcal{G}^{BO}_{jl,\alpha}. \tag{5.38}$$

$\mathbf{d}^{(1)}_{jl}$ and $d^{(2)}_{jl}$ fulfil the following symmetry relations

$$\begin{aligned} \mathbf{d}^{(1)}_{lj,\alpha} &= -\mathbf{d}^{(1)}_{jl,\alpha} \\ d^{(2)}_{lj,\alpha} &= d^{(2)}_{jl,\alpha}. \end{aligned} \tag{5.39}$$

Using the approximations (5.35) and (5.36), and the relation (5.37-5.39), the coupling potentials (5.6-5.8) become

$$\begin{aligned}
\hat{U}_{en}^{corr} &\rightarrow \sum_{\alpha=1}^{N_n} \frac{1}{M_\alpha}\Big[\frac{i\hbar\nabla_\alpha\cdot\mathbf{A}_\alpha(\underline{\underline{\mathbf{R}}}^c(t)) - \mathbf{A}_\alpha^2(\underline{\underline{\mathbf{R}}}^c(t))}{2} - \mathbf{P}_\alpha^c\cdot\mathbf{A}_\alpha(\underline{\underline{\mathbf{R}}}^c(t))\Big], \\
\epsilon(\underline{\underline{\mathbf{R}}},t) &\rightarrow \sum_j |C_j(\underline{\underline{\mathbf{R}}}^c(t))|^2\epsilon_{BO}^j(\underline{\underline{\mathbf{R}}}^c(t)) + \sum_{jl} C_j^*(\underline{\underline{\mathbf{R}}}^c(t))C_l(\underline{\underline{\mathbf{R}}}^c(t))H_{jk}^c \\
&+ \sum_\alpha \frac{\hbar^2}{M_\alpha}\Big[\sum_{j<l}\Re\left[C_j^*C_l\right]d_{jl,\alpha}^{(2)}(\underline{\underline{\mathbf{R}}}^c(t)) - \mathbf{A}_\alpha^2(\underline{\underline{\mathbf{R}}}^c(t))\Big], \\
\mathbf{A}_\alpha(\underline{\underline{\mathbf{R}}}^c(t)) &\rightarrow 2\hbar\sum_{j<l}^{\infty}\Im\left[C_j^*C_l\right]\mathbf{d}_{jl,\alpha}^{(1)}(\underline{\underline{\mathbf{R}}}^c(t)).
\end{aligned} \tag{5.40}$$

Then, the electronic equation (5.15) that is coupled to the classical nuclear motion reads

$$\dot{C}_j(t) = -\frac{i}{\hbar}\left[\epsilon_{BO}^{(j)} - \left(V_{eff}^R + iV_{eff}^{(I)}\right)\right]C_j(t) - \sum_l C_l(t)D_{jl}, \tag{5.41}$$

where

$$\begin{aligned}
V_{eff}^{(R)} =& \sum_j |C_j|^2\,\epsilon_{BO}^{(j)}(\underline{\underline{\mathbf{R}}}^c) + \sum_{j<l}\Re\left[C_j^*C_l\right]\sum_\alpha\frac{\hbar^2}{M_\alpha}d_{jl,\alpha}^{(2)}(\underline{\underline{\mathbf{R}}}^c) \\
&+ 2\hbar\sum_{j<l}\Im\left[C_j^*C_l\right]\sum_\alpha\frac{\mathbf{P}_\alpha^c}{M_\alpha}\cdot\mathbf{d}_{jl,\alpha}^{(1)}(\underline{\underline{\mathbf{R}}}^c),
\end{aligned} \tag{5.42}$$

is the real effective potential, while

$$V_{eff}^{(I)} = -\sum_{j<l}\Im\left[C_j^*C_l\right]\sum_\alpha\frac{\hbar^2}{M_\alpha}\nabla_\alpha\cdot\mathbf{d}_{jl,\alpha}^{(1)}(\underline{\underline{\mathbf{R}}}^c), \tag{5.43}$$

is the imaginary effective potential, and

$$\begin{aligned}
D_{jl} =& \sum_\nu\frac{1}{M_\alpha}\nabla_\alpha\mathbf{P}_\alpha^c\cdot\mathbf{d}_{jl,\alpha}^{(1)}(\underline{\underline{\mathbf{R}}}^c) \\
&- \frac{i\hbar}{2M_\alpha}\left(\nabla_\alpha\cdot\mathbf{d}_{jl,\alpha}^{(1)}(\underline{\underline{\mathbf{R}}}^c) - d_{jl,\alpha}^{(2)}(\underline{\underline{\mathbf{R}}}^c)\right)
\end{aligned} \tag{5.44}$$

are the effective NACs that couple the evolution of the populations.

The electronic equation (5.41) describes the (norm-conserving) evolution of the time-dependent coefficients of the expansion (2.63). The first term on the r.h.s. of (5.42) is a diagonal term containing the BO potential energies corrected by the real effective potential from Eq. (5.42) and the imaginary effective potential (5.43), $V_{eff}^{(I)}$. In particular, the imaginary effective potential appears as a sink/source term and is responsible for

population exchange of the adiabatic states, even in the absence of the off-diagonal coupling terms. The last term in the r.h.s of (5.41) contains the off-diagonal terms (5.44), D_{jk}, that are expressed in terms of the NACs (5.38 and 5.38) and are responsible for driving the population exchange between state j and k.

Interestingly, the modulus squared of the expansion coefficients, $C_j(t)$, that are the solutions of the electronic equation (5.41), are actually the classical limit of the exact populations of the BO states (4.11), $\int d\underline{\underline{\mathbf{R}}}|F_j(\underline{\underline{\mathbf{R}}},t)|^2$. This can be seen by using Eq. (4.8),

$$\int d\underline{\underline{\mathbf{R}}}|F_j(\underline{\underline{\mathbf{R}}},t)|^2 = \int d\underline{\underline{\mathbf{R}}}|C_j(\underline{\underline{\mathbf{R}}},t)|^2|\chi(\underline{\underline{\mathbf{R}}},t)|^2, \tag{5.45}$$

and taking the classical limit of $|\chi(\underline{\underline{\mathbf{R}}},t)|^2$,

$$\begin{aligned}\int d\underline{\underline{\mathbf{R}}}|F_j(\underline{\underline{\mathbf{R}}},t)|^2 &= \int d\underline{\underline{\mathbf{R}}}|C_j(\underline{\underline{\mathbf{R}}},t)|^2\delta(\underline{\underline{\mathbf{R}}}-\underline{\underline{\mathbf{R}}}^c(t))\,, \\ &= |C_j(\underline{\underline{\mathbf{R}}}^c(t))|^2. \end{aligned}\tag{5.46}$$

The classical nuclear Hamiltonian (5.26), on the other hand, may be rewritten as

$$H_n = \sum_{\nu=1}^{N_n}\frac{|\mathbf{P}_\alpha^c|^2}{2M_\nu} + V_{eff}^{(R)}(\underline{\underline{\mathbf{R}}}^c,\underline{\underline{\mathbf{P}}}^c). \tag{5.47}$$

It contains the real effective potential (5.42), $V_{eff}^{(R)}(\underline{\underline{\mathbf{R}}})$, that effectively accounts for the coupling between the electronic and nuclear degrees of freedom via a *mean-field* term,

$$E_{mf}(\underline{\underline{\mathbf{R}}}^c) = \sum_j |C_j|^2\,\epsilon_{BO}^{(j)}(\underline{\underline{\mathbf{R}}}^c(t)) \tag{5.48}$$

which is the average of the BO energies weighted by the populations of the states, a *non-adiabatic* term,

$$E_{na}(\underline{\underline{\mathbf{R}}}^c) = \sum_{j<l}\Re\left[C_j^*C_l\right]\sum_\alpha\frac{\hbar^2}{M_\alpha}d_{jl,\alpha}^{(2)}(\underline{\underline{\mathbf{R}}}^c(t)) \tag{5.49}$$

that contains second-order NACs (5.38), and a *kinetic* term,

$$E_k(\underline{\underline{\mathbf{R}}}^c,\underline{\underline{\mathbf{P}}}^c) = 2\hbar\sum_{j<l}\Im\left[C_j^*C_l\right]\sum_\alpha\frac{\mathbf{P}_\alpha^c}{M_\alpha}\cdot\mathbf{d}_{jl,\alpha}^{(1)}(\underline{\underline{\mathbf{R}}}^c(t))\,, \tag{5.50}$$

which couples the nuclear momentum to the first-order NAC (5.38).

parameter	value (a.u.)
M	1836.1528
L	19.050
R_f	5.0
R_l	3.1
R_r	4.0

TABLE 5.1: List of parameters in the Hamiltonian (3.15).

The real effective potential

$$V_{eff}^{(R)}(\underline{\underline{\mathbf{R}}}^c, \underline{\underline{\mathbf{P}}}^c) = E_{mf}(\underline{\underline{\mathbf{R}}}^c) + E_{na}(\underline{\underline{\mathbf{R}}}^c) + E_k(\underline{\underline{\mathbf{R}}}^c, \underline{\underline{\mathbf{P}}}^c) \tag{5.51}$$

that governs the classical motion of the nuclei contains all electronic non-adiabatic effects, beyond mean-field, via the kinetic term, $E_k(\underline{\underline{\mathbf{R}}}^c(t)$, which couples the vector potential to the nuclear momentum, and the non-adiabatic term, $E_{na}(\underline{\underline{\mathbf{R}}}^c(t))$, containing second-order non-adiabatic couplings. The last two terms of (5.51), on the other hand, contribute to reproduce the nuclear kinetic energy corresponding to the mean nuclear kinetic energy, calculated from the full quantum calculations. This can be shown by taking the classical limit of (2.72) using (5.40) and (5.21) up to within the zeroth-order term in $\hbar$. Hence,

$$< \Psi|\hat{T}_N|\Psi > \rightarrow \sum_{\nu=1}^{N_n} \frac{|\mathbf{P}_\alpha^c|^2}{2M_\nu} + E_{na}(\underline{\underline{\mathbf{R}}}^c) + E_k(\underline{\underline{\mathbf{R}}}^c, \underline{\underline{\mathbf{P}}}^c). \tag{5.52}$$

5.2.1 Numerical results

Here, we employ the Shin-Metiu model (3.2.2), with the parameters used in (4.2.1) and summarized in table (5.1). The first four BO surfaces (left) and the NACs between the first two BO states (right) of the system are shown in Fig. 5.1. For this model we examine the performance of the MQC scheme, by using single-trajectory (ST) and multiple-trajectory (MT) approaches, in comparison with the exact solution of the TDSE. In a MT calculation the same equation of motion as the single trajectory calculation is applied to many initial conditions with the goal of recovering some quantum features of the nuclear dynamics such as spreading of the wave-packet.

The initial state for the quantum propagation is $\Psi(r, R, 0) = G_\sigma(R - R_0)\varphi_R^{(2)}(r)$, where G_σ is a normalized Gaussian centered at $R_0 = -4.0$ a.u. with $\sigma = 1/\sqrt{2.85}$ a.u. and $\varphi_R^{(2)}(r)$ is the excited BO state (see 4.10). Hence, the initial population of the second

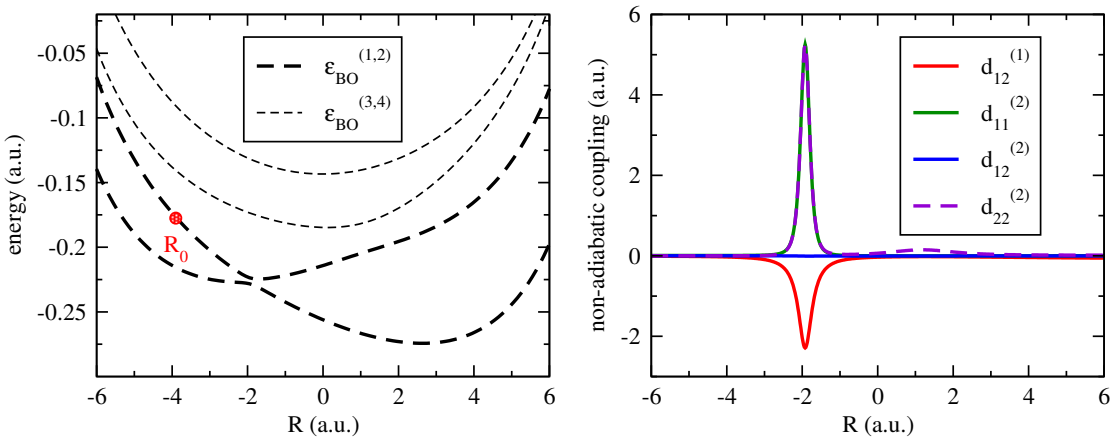

FIGURE 5.1: BO surfaces $\epsilon_{BO}^{(l)}(R)$ (left) from the Hamiltonian in Eq. (3.15) and NACs (right). The red dot indicates R_0 (see text).

electronic state is one. The mean initial momentum is zero, i.e., the initial nuclear wave-function is real. We propagate the TDSE numerically with the time-step 0.05 a.u. using the second order split operator technique [59], to obtain the full molecular wave-function, $\Psi(r, R, t)$, and from that we calculate the expectation values.

The classical trajectory starts in the position R_0 with zero initial momentum. If multiple independent trajectories (6000 in this case) are used, initial conditions are sampled according to the Wigner distribution associated to $\Psi_{initial}(r, R)$. The electronic and nuclear equations, in the MQC scheme, are integrated with the time-step 0.1 a.u. and using the fourth-order Runge-Kutta and the velocity-Verlet algorithm, respectively.

The populations of the BO states and the nuclear kinetic energy, as functions of time, calculated from the full electron-nuclear wave-function and from the MQC scheme (using $|C_j(t)|^2$ and 5.52) are depicted in Fig. 5.2. It is shown (left panel) that the MQC evolution (red line, ST-MQC, and dashed green line, MT-MQC) is able to reproduce the branching of the populations of the electronic states after the passage through the avoided crossing ($t \sim 500$ .a.u.) in a close agreement with the quantum calculations (blue line). The use of several trajectories improves the agreement during the time interval in which the population exchange takes place. The nuclear kinetic energy (right panel) from MQC calculations shows a qualitative agreement with exact results, though presenting a slight deviation after the passage through the avoided crossing: this small deviation reveals the fact that quantum corrections, quasi-classically or semi-classically, need to be added to the purely classical nuclear dynamics. Here, deviation from quantum

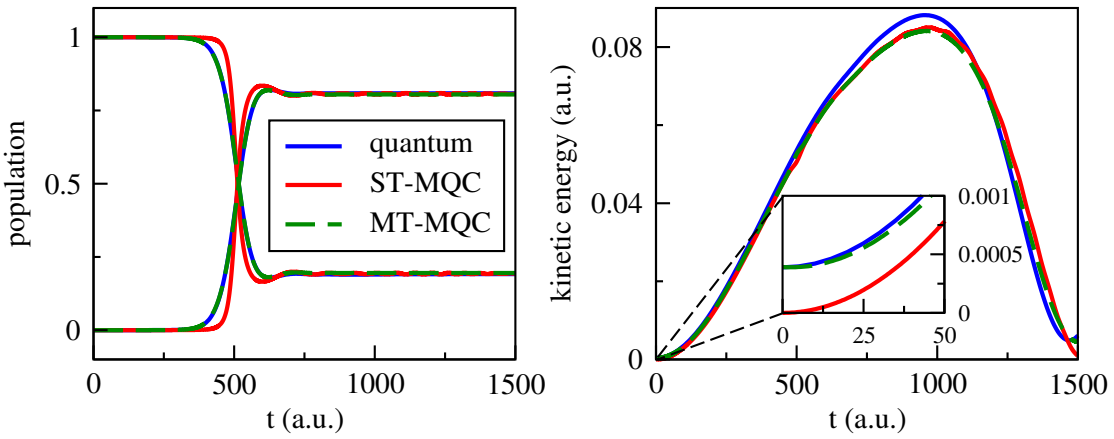

FIGURE 5.2: Left panel: populations of the BO states as functions of time determined by quantum (blue), ST-MQC (red) and MT-MQC (dashed green) propagation schemes. Right panel: nuclear kinetic energy as function of time.

behavior occurs at the nuclear position $R \sim 2.0$ a.u., where the lower BO surface has a negative slope and the upper BO surface has a slightly positive slope. Therefore, in the quantum evolution the nuclear wave-packet propagating "on" the upper surface is slowed down while the wave-packet "on" the lower surface is accelerated, producing the splitting of the nuclear wave-packet. This feature cannot be captured by a simple independent trajectories approach. Note that a better agreement with exact calculations is achieved within the MT-MQC scheme at initial (inset in Fig. 5.2) and final times, where the nuclear kinetic energy does not become zero as consequence of the spreading of the quantum nuclear wave-packets.

5.3 The classical limit of the nuclear motion: an extensive study

The classical limit of the nuclear motion has been discussed briefly in (5.2). Here, we delve deeper into the derivation and interpretation of the classical limit of nuclear motion.

The general nuclear wave-function may be written in polar representation as

$$\chi(\underline{\underline{\mathbf{R}}}, t) = e^{\frac{i}{\hbar} S_0(\underline{\underline{\mathbf{R}}}, t)} \left| \chi(\underline{\underline{\mathbf{R}}}, t) \right|, \tag{5.53}$$

in the classical limit amplitude and phase have to satisfy the following requirements

$$\begin{aligned} \left|\chi(\underline{\underline{\mathbf{R}}}^c, t)\right|^2 &= \delta\left(\underline{\underline{\mathbf{R}}} - \underline{\underline{\mathbf{R}}}^c(t)\right) \quad \text{(i)} \\ \nabla_{\underline{\underline{\mathbf{R}}}} S_0(\underline{\underline{\mathbf{R}}}^c, t) &= \underline{\underline{\mathbf{P}}}^c(\underline{\underline{\mathbf{R}}}^c, t). \quad \text{(ii)} \end{aligned} \tag{5.54}$$

Here, $\underline{\underline{\mathbf{R}}}^c(t)$ is the classical trajectory and $\underline{\underline{\mathbf{P}}}^c(t)$ is the classical nuclear momentum, evaluated along the classical trajectory. Condition (5.54 - i) can be understood intuitively, since we expect the density of a classically moving point particle to be infinitely localized, at each time, at its position $\underline{\underline{\mathbf{R}}}^c(t)$. Condition (5.54 - ii) must hold in order to recover classical dynamics, at the lowest order in $\hbar$, starting from quantum dynamics. Formally, conditions (5.54 - i) and (5.54 - ii) involve the limits

$$\begin{aligned} \Sigma &\to 0 \quad \text{(a)} \\ \hbar &\to 0, \quad \text{(b)} \end{aligned} \tag{5.55}$$

where Σ in (5.55 - a) is the variance associated to the nuclear density and (5.55 - b) is performed in all terms containing the nuclear wave-function (see 5.2). We anticipate that the effect of (5.55 - a) and (5.55 - b) is

$$\nabla_{\underline{\underline{\mathbf{R}}}} C_j(\underline{\underline{\mathbf{R}}}, t),\ \nabla^2_{\underline{\underline{\mathbf{R}}}} C_j(\underline{\underline{\mathbf{R}}}, t) \to 0 \quad \text{if} \quad \Sigma \to 0 \tag{5.56}$$

$$\frac{-i\hbar \nabla_{\underline{\underline{\mathbf{R}}}} \chi(\underline{\underline{\mathbf{R}}}, t)}{\chi(\underline{\underline{\mathbf{R}}}, t)} \to \underline{\underline{\mathbf{P}}}^c(t) \quad \text{if} \quad \hbar \to 0. \tag{5.57}$$

Eq. (5.56) is valid when the first and second derivatives of the modulus $|C_j(\underline{\underline{\mathbf{R}}}, t)|$ and the phase $\vartheta_j(\underline{\underline{\mathbf{R}}}, t)$ of the expansion coefficients are zero. At each time t, it is sufficient to require that Eq. (5.56) holds in $\underline{\underline{\mathbf{R}}}^c$, however, in the classical limit, $|C_j(\underline{\underline{\mathbf{R}}}, t)|$ is a constant function of $\underline{\underline{\mathbf{R}}}$. This is usually taken for granted [72–74] in the expansion (2.63), given that the nuclei are classical and will be proved here, together with Eq. (5.57). To this end, we suppose that $\chi(\underline{\underline{\mathbf{R}}}, t)$ is a Gaussian wave-packet,

$$\left|\chi(\underline{\underline{\mathbf{R}}}, t)\right|^2 = G_\Sigma\left(\underline{\underline{\mathbf{R}}} - \underline{\underline{\mathbf{R}}}^c(t)\right), \tag{5.58}$$

with $G_\Sigma\left(\underline{\underline{\mathbf{R}}} - \underline{\underline{\mathbf{R}}}^c(t)\right)$ a normalized Gaussian centered at $\underline{\underline{\mathbf{R}}}^c(t)$ with variance Σ. The Gaussian moves with mean momentum $\underline{\underline{\mathbf{P}}}^c$. The partial normalization condition of the electronic wave-function is used to derive the relation

$$\left|\chi(\underline{\underline{\mathbf{R}}}, t)\right|^2 = \sum_j \left|F_j(\underline{\underline{\mathbf{R}}}, t)\right|^2. \tag{5.59}$$

In the classical limit, the term on the l.h.s. reduces to a δ-function at $\underline{\underline{\mathbf{R}}}^c(t)$, consequently

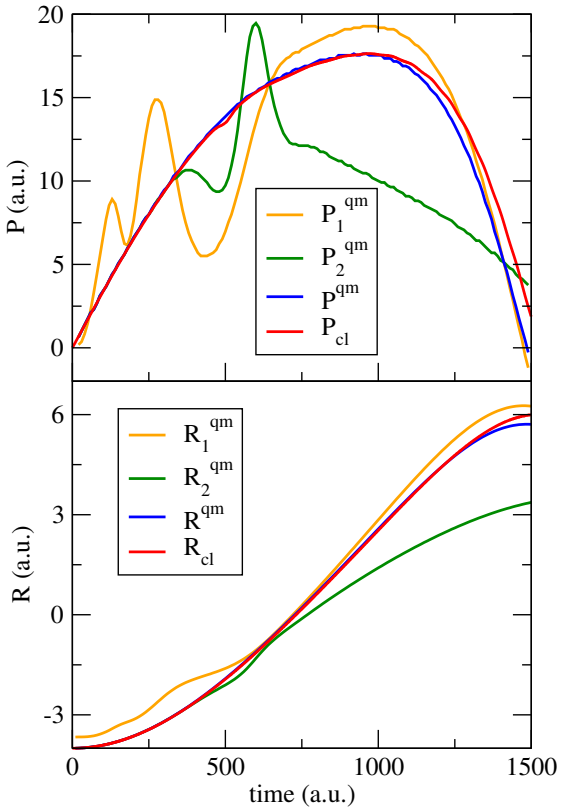

FIGURE 5.3: Lower panel: classical position (red line) as function of time, compared to the mean positions calculated from $|F_j(R,t)|^2$ ($j = 1$ orange line and $j = 2$ green line) and $|\chi(R,t)|^2$ (blue line). Upper panel: classical momentum as function of time, compared with (M times) the rate of variation of the mean positions from quantum propagation.

at each point $\underline{\underline{\mathbf{R}}}$ where $\left|\chi(\underline{\underline{\mathbf{R}}},t)\right|^2$ is zero, all terms on the r.h.s. have to be zero, since they are all non-negative. Therefore, $\left|F_j(\underline{\underline{\mathbf{R}}},t)\right|^2$ should become δ-functions at $\underline{\underline{\mathbf{R}}}^c(t)$. Since we are interested in this limit, we represent each term of the sum on the r.h.s. by a non-normalized Gaussian ($F_j(\underline{\underline{\mathbf{R}}},t)$ is not normalized), but centered at different positions, $\underline{\underline{\mathbf{R}}}^j(t)$, than $\underline{\underline{\mathbf{R}}}^c(t)$. Using this hypothesis, Eq. (5.59) becomes

$$G_\Sigma\left(\underline{\underline{\mathbf{R}}}-\underline{\underline{\mathbf{R}}}^c(t)\right)=\sum_j B_j^2(t)G_{\sigma_j}\left(\underline{\underline{\mathbf{R}}}-\underline{\underline{\mathbf{R}}}^j(t)\right), \tag{5.60}$$

where $\sum_j B_j^2(t) = 1$ accounts for the normalization of $\chi(\underline{\underline{\mathbf{R}}},t)$. The pre-factors $B_j^2(t)$ have been introduced because F_js are not normalized. Then we show that

$$\Sigma = \sigma_j \quad \text{(i)} \tag{5.61}$$

$$\underline{\underline{\mathbf{R}}}^j(t) = \underline{\underline{\mathbf{R}}}^c(t) \quad \forall j,\, t. \quad \text{(ii)} \tag{5.62}$$

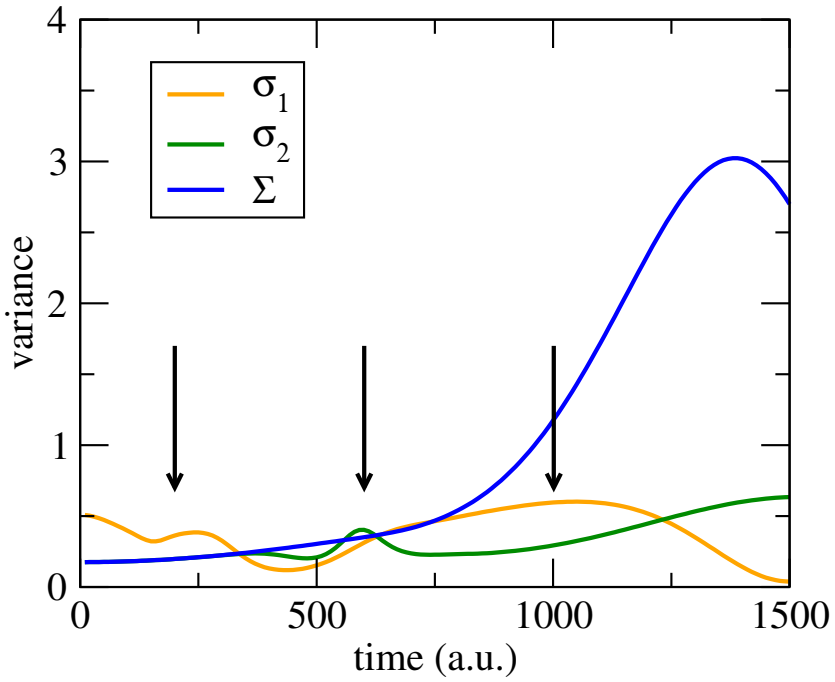

FIGURE 5.4: Variances of $|\chi(R,t)|^2$ (blue line) and of $|F_j(R,t)|^2$ ($j=1$ orange line and $j=2$ green line) as functions of time. The arrows indicate the times, 200, 600 and 1000 a.u., at which we observe the nuclear densities, in Fig. 5.5.

To this end, we compare the behavior of both sides of eq. (5.60) for $\underline{\underline{\mathbf{R}}} \to \pm\infty$: we need to show that

$$1 = \lim_{\underline{\underline{\mathbf{R}}}\to\pm\infty} \sum_j B_j^2(t) \frac{\Sigma}{\sigma_j} \exp\left[-\frac{\left(\underline{\underline{\mathbf{R}}} - \underline{\underline{\mathbf{R}}}^j(t)\right)^2}{\sigma_j^2} + \frac{\left(\underline{\underline{\mathbf{R}}} - \underline{\underline{\mathbf{R}}}^c(t)\right)^2}{\Sigma^2} \right], \tag{5.63}$$

where the explicit expressions of the Gaussians Eq. (5.60) is used. The limit (5.63) implies that

$$\lim_{\underline{\underline{\mathbf{R}}}\to\pm\infty} e^{-\left(\sigma_j^{-2}-\Sigma^{-2}\right)\underline{\underline{\mathbf{R}}}^2} < \infty \tag{5.64}$$

or, equivalently,

$$\sigma_j^{-2} - \Sigma^{-2} \geq 0 \Rightarrow \sigma_j^2 \leq \Sigma^2. \tag{5.65}$$

A similar argument is applied to the Fourier Transform (FT) of both sides of eq. (5.60)

$$\hat{G}_{\tilde{\Sigma},\underline{\underline{\mathbf{R}}}^c}(\underline{\underline{\mathbf{k}}}) = \sum_j B_j^2(t) \hat{G}_{\tilde{\sigma}_j,\underline{\underline{\mathbf{R}}}_j}(\underline{\underline{\mathbf{k}}}), \tag{5.66}$$

where

$$\hat{G}_{\tilde{\Sigma},\underline{\underline{\mathbf{R}}}^c}(\underline{\underline{\mathbf{k}}}) = FT\left[G_\Sigma(\underline{\underline{\mathbf{R}}} - \underline{\underline{\mathbf{R}}}^c)\right](\underline{\underline{\mathbf{k}}}) = \frac{e^{-i\underline{\underline{\mathbf{R}}}^c\cdot\underline{\underline{\mathbf{k}}}}}{2\pi} e^{\tilde{\Sigma}^2\underline{\underline{\mathbf{k}}}^2} \tag{5.67}$$

(a similarly for $\hat{G}_{\tilde{\sigma}_j,\underline{\underline{\mathbf{R}}}_j}(\underline{\underline{\mathbf{k}}})$) with $\tilde{\Sigma} = \Sigma/2$. The Gaussian transforms in another Gaussian

with inverse variance, and if we calculate the limit $\underline{\underline{\mathbf{k}}} \to \pm\infty$, we obtain a relation similar to Eq. (5.65), namely

$$\tilde{\sigma}_j^2 - \tilde{\Sigma}^2 \geq 0 \Rightarrow \sigma_j^2 \geq \Sigma^2. \tag{5.68}$$

Eqs. (5.65) and (5.68) must be simultaneously satisfied, then

$$\sigma_j^2 = \Sigma^2 \Rightarrow \sigma_j = \Sigma, \tag{5.69}$$

and this proves statement (i). On the other hand. Eq. (5.60) at $\underline{\underline{\mathbf{R}}} = \underline{\underline{\mathbf{R}}}^c(t)$, becomes

$$1 = \sum_j B_j^2(t) \exp\left[-\frac{(\underline{\underline{\mathbf{R}}}^c(t) - \underline{\underline{\mathbf{R}}}^j(t))^2}{\Sigma^2}\right] \tag{5.70}$$

and, since the pre-factors $B_j^2(t)$ sum up to unity, the relation

$$\underline{\underline{\mathbf{R}}}^j(t) = \underline{\underline{\mathbf{R}}}^c(t) \tag{5.71}$$

must hold, otherwise

$$0 \leq \exp\left[-\frac{(\underline{\underline{\mathbf{R}}}^c(t) - \underline{\underline{\mathbf{R}}}^j(t))^2}{\Sigma^2}\right] < 1 \quad if \quad \underline{\underline{\mathbf{R}}}_j(t) \neq \underline{\underline{\mathbf{R}}}^c(t). \tag{5.72}$$

This proves statement (ii). Consequently,

$$\left|C_j(\underline{\underline{\mathbf{R}}}, t)\right| = \left[\frac{B_j^2(t) G_{\sigma_j}\left(\underline{\underline{\mathbf{R}}} - \underline{\underline{\mathbf{R}}}_j(t)\right)}{G_\Sigma\left(\underline{\underline{\mathbf{R}}} - \underline{\underline{\mathbf{R}}}^c(t)\right)}\right]^{\frac{1}{2}} = B_j(t) \tag{5.73}$$

is only a function of time and is constant in space. The first and second derivatives of phase, $\vartheta_j(\underline{\underline{\mathbf{R}}}, t)$, of the coefficient $C_j(\underline{\underline{\mathbf{R}}}, t)$ satisfy the relations

$$\nabla_{\underline{\underline{\mathbf{R}}}} \vartheta_j(\underline{\underline{\mathbf{R}}}, t) = \nabla_{\underline{\underline{\mathbf{R}}}} \lambda_j(\underline{\underline{\mathbf{R}}}, t) - \underline{\underline{\mathbf{P}}}^c(\underline{\underline{\mathbf{R}}}, t) \tag{5.74}$$

$$\nabla^2_{\underline{\underline{\mathbf{R}}}} \vartheta_j(\underline{\underline{\mathbf{R}}}, t) = \nabla_{\underline{\underline{\mathbf{R}}}} \left(\nabla_{\underline{\underline{\mathbf{R}}}} \lambda_j(\underline{\underline{\mathbf{R}}}, t) - \underline{\underline{\mathbf{P}}}^c(\underline{\underline{\mathbf{R}}}, t)\right) \tag{5.75}$$

where we used Eq. (4.8) to represent $\lambda_j(\underline{\underline{\mathbf{R}}}, t)$ in terms of the phases of $F_j(\underline{\underline{\mathbf{R}}}, t)$, $\lambda_j(\underline{\underline{\mathbf{R}}}, t)$, and $\chi(\underline{\underline{\mathbf{R}}}, t)$, $S_0(\underline{\underline{\mathbf{R}}}, t)$ and the relation, $\underline{\underline{\mathbf{P}}}^c(\underline{\underline{\mathbf{R}}}, t) = \nabla_{\underline{\underline{\mathbf{R}}}} S_0(\underline{\underline{\mathbf{R}}}, t)$, is imposed by the classical limit (Eq. (5.54 - ii)). Classically (or semi-classically), $\underline{\underline{\mathbf{P}}}^c(\underline{\underline{\mathbf{R}}}, t)$ governs the motion of $\underline{\underline{\mathbf{R}}}^c(t)$ and, since $\underline{\underline{\mathbf{R}}}^j(t) = \underline{\underline{\mathbf{R}}}^c(t)$ $\forall t$, it also determines $\underline{\underline{\mathbf{R}}}^j(t)$,

$$\underline{\underline{\mathbf{P}}}^j(\underline{\underline{\mathbf{R}}}, t) = \nabla_{\underline{\underline{\mathbf{R}}}} \lambda_j(\underline{\underline{\mathbf{R}}}, t) = \underline{\underline{\mathbf{P}}}^c(\underline{\underline{\mathbf{R}}}, t). \tag{5.76}$$

This observation proves that $\nabla_{\underline{\underline{\mathbf{R}}}}\vartheta_j(\underline{\underline{\mathbf{R}}},t) = \nabla^2_{\underline{\underline{\mathbf{R}}}}\vartheta_j(\underline{\underline{\mathbf{R}}},t) = 0$, and together with Eq. (5.73), shows the validity of Eq. (5.56).

5.3.1 Validity of the classical approximation

The classical approximation of the nuclear motion is valid if the nuclear density remains localized around the classical position $R^c(t)$. Due to the fact that $|\chi(R,t)|^2$ is the sum of contributions, or partial densities, evolving "on" different BO surfaces, this condition is also applied to each contribution. Moreover, in a classical evolution, the displacement of the nuclear wave-function, as well as of the partial contributions, are driven by the classical nuclear momentum P^c. This further guarantees that the previous condition is satisfied at all times. In this very last section, by discussing some numerical results, we investigate limits of validity of the classical approximation of the nuclear motion.

We compare the position of the classical movable ion in Fig. (3.1) with the expectation value of the position operator calculated using the nuclear wave-function, $\chi(R,t)$,

$$R^{qm}(t) = \int dR\, R\, |\chi(R,t)|^2 \tag{5.77}$$

and using the partial contributions, $F_j(R,t)$,

$$R_j^{qm}(t) = \frac{1}{\rho_j(t)} \int dR\, R\, |F_j(R,t)|^2 \tag{5.78}$$

with the normalization factor from Eq. (4.11). Fig. (5.3) (lower panel) shows that the classical position R_{cl} (red line) almost coincides at all times, up to about 1200 a.u., with the mean position R^{qm} calculated from the nuclear density (blue line). Here we should mention that R^{qm} is the average of R_1^{qm} and R_2^{qm} (orange and green lines), weighted by the populations of the states, namely

$$R^{qm}(t) = \sum_j \rho_j(t) R_j^{qm}(t). \tag{5.79}$$

Larger deviations are observed in the comparison between the classical position and R_1^{qm}, before the passage through the avoided crossing at about 500 a.u., or R_2^{qm}, after this time. However, they do not negatively contribute to the overall agreement between R_{cl} and R^{qm}, because at short times, the population, and thus the weight of the BO state 1 is (much) smaller than that of the BO state 2, and vice-versa at longer times. Furthermore, it is evident that $|F_2(R,t)|$, moving on the upper BO surface, slows down

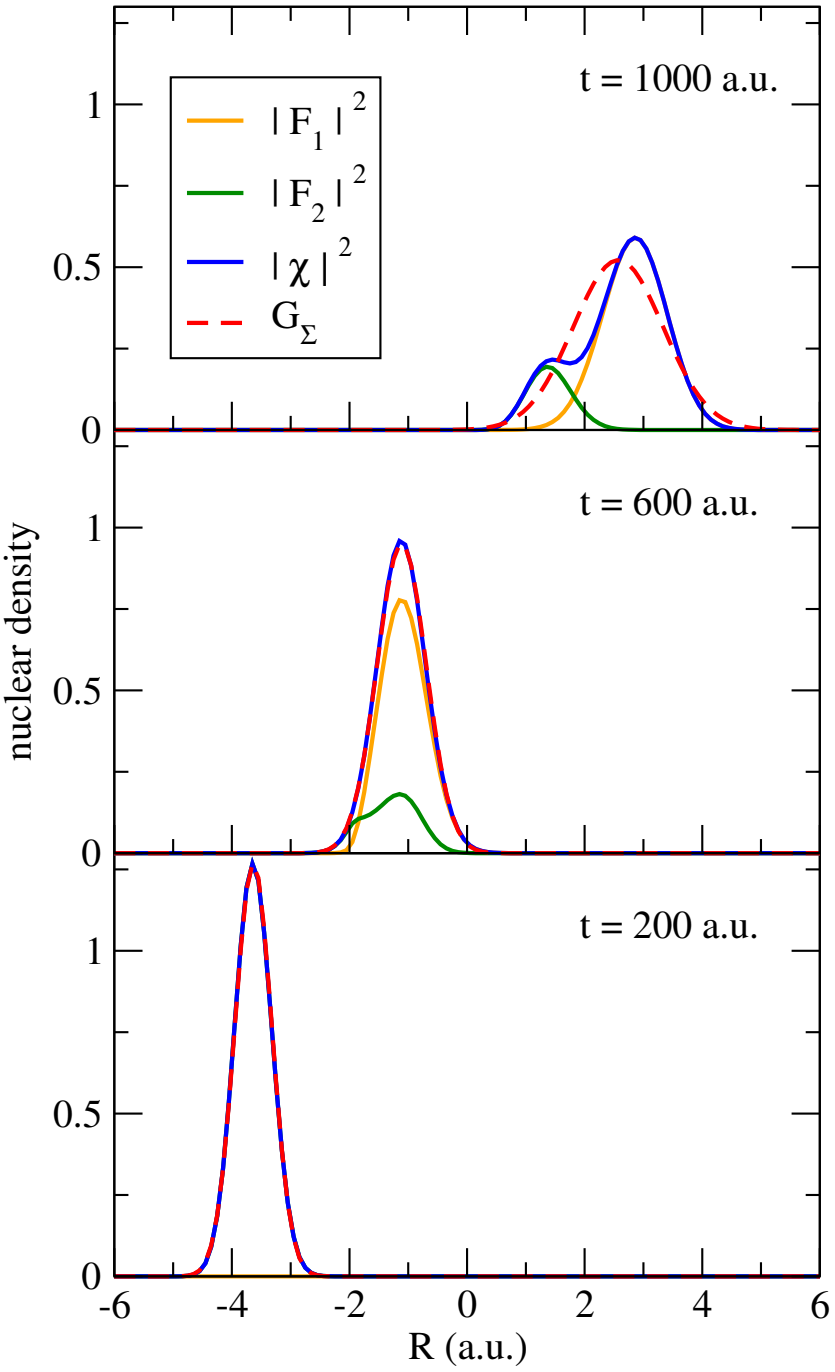

FIGURE 5.5: Nuclear density $|\chi(R,t)|^2$ (blue line) and partial contributions $|F_1(R,t)|^2$ (orange line) and $|F_2(R,t)|^2$ (blue line). They are shown at different times, namely 200, 600 and 1000 a.u., as indicated by the arrows in Fig. 5.4. The red dashed lines are the Gaussian functions $G_\Sigma(R - R^{qm})$ with the same mean value R^{qm} (from Fig. 5.3) and variance Σ (from Fig. 5.4) of the nuclear density.

at about 700 a.u., as the curve representing the momentum (computed as the rate of variation of the mean position) shows in Fig. (5.3) (upper panel). From the comparison between the classical momentum (red line) and $P^{qm} = M\dot{R}^{qm}$ (blue line), we notice that already at about 1000 a.u. classical evolution starts to deviate from quantum evolution. The oscillations of P_1^{qm} and P_2^{qm}, missing in the classical approach, in the time range 400 - 700 a.u., indicate the crossing of the strong non-adiabatic coupling region. The large oscillations of P_1^{qm}, before 400 a.u., do not affect the behavior of P^{qm}, since, as stated above, the population of the BO state 1 is very small before the passage through the coupling region.

In the previous section (5.3), it was shown that Eq. (5.56) is valid if the variance Σ associated to the nuclear density is equal (or close) to the variances σ_j of $|F_j(R,t)|^2$. Such condition is satisfied in the classical limit and shall be proven to be approximately verified in quantum calculations. In Fig (5.4), Σ and σ_j are shown, as functions of time. Up to about 700 a.u., the hypothesis at the basis of the classical treatment of nuclear dynamics are approximately fulfilled, since the variances Σ and σ_j do not deviate too much from each other. The deviation becomes important at 1000 a.u. and the effect on the nuclear density is shown in Fig. (5.5): it confirms that the classical approximation holds as long as the nuclear density is well localized at one center (as at $t = 200$ a.u. and $t = 600$ a.u.), whereas a single trajectory cannot capture the evolution when it develops different centers (as at $t = 1000$ a.u.). Moreover, the approximation of the nuclear density as a Gaussian wave-packet, in Eq. (5.58), is well-grounded at $t = 200$ and $t = 600$ a.u., as shown in Fig. (5.5), and fails at later times. This is clear from the comparison between the dashed red and blue curves in Fig. (5.5), where the red curves are normalized Gaussian functions with the same mean values and variances as the nuclear densities. At $t = 200$ and $t = 600$ a.u., $|\chi(R,t)|^2$ coincides with a Gaussian, while at $t = 1000$ a.u. the two curves are quite different from each other. At $t = 1000$ a.u., the classical approximation breaks down as the nuclear wave-function becomes delocalized and the hypothesis at the basis of Eqs. (5.56) and (5.57) are not fulfilled.

Fig. (5.6) shows the comparison between the mean-field potential $E_{mf}(R_{cl}(t))$ from Eq. (5.51), felt by the classical particle at R_{cl}, and

$$\epsilon_{mf}^{exact} = \langle \Phi_{\underline{\underline{\mathbf{R}}}}(t) | \hat{H}_{BO} | \Phi_{\underline{\underline{\mathbf{R}}}}(t) \rangle_{\underline{\mathbf{r}}} \tag{5.80}$$

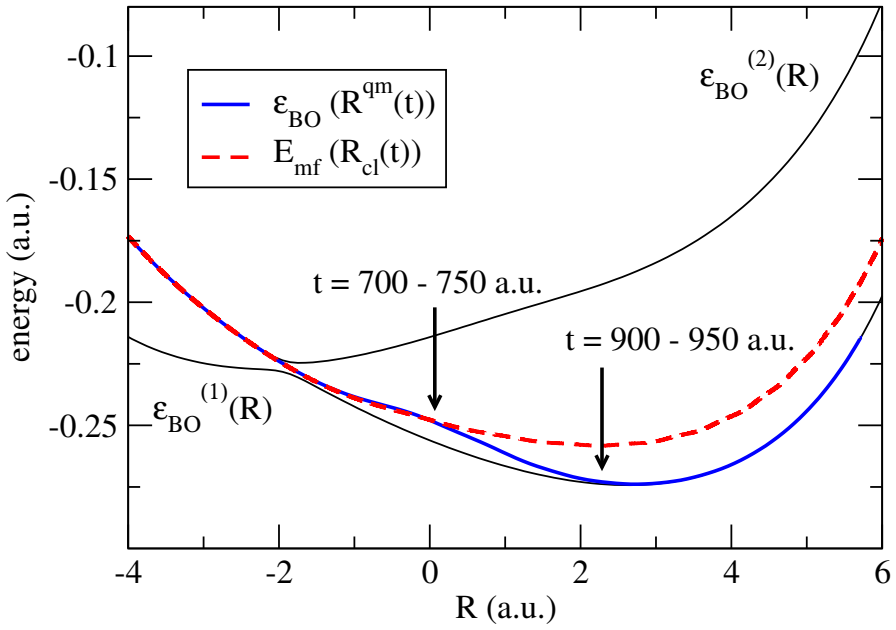

FIGURE 5.6: Comparison between the classical mean-field potential (dashed red line) and the BO contribution to the quantum TDPES (blue line). At each time, the classical nuclear position $R_{cl}(t)$ and the quantum mean position $R^{qm}(t)$ are determined. The mean-field energy E_{mf} and ϵ_{mf}^{exact} are evaluated at the classical and quantum positions, respectively. The BO surfaces (black lines) are also shown, as a reference. The arrows at $t = 750$ a.u. and $t = 900 - 950$ a.u. indicate the space points, with the corresponding time intervals, where, respectively, the potential energy curves start to disagree and ϵ_{mf}^{exact} coincides with $\epsilon_{BO}^{(1)}(R)$.

component of the exact TDPES, evaluated at the mean position R^{qm}. The BO surfaces are also shown as a reference. It can be seen in Fig. (5.6) that up to $t = 700 - 750$ a.u., the two curves are in very good agreement, meaning that an extremely (in the limit, infinitely) localized nuclear wave-function feels a "quantum" potential (the exact TDPES), due to the presence of the electrons, which coincides with the classical mean-field potential. We already observed that at longer times $|F_1|$ and $|F_2|$ follow different paths in R-space and a description in terms of a single trajectory cannot capture this feature. In particular, at $t = 900 - 950$ a.u., ϵ_{mf}^{exact} coincides with the lower BO surface $\epsilon_{BO}^{(1)}(R)$ because $R^{qm} \simeq R_1^{qm}$ as the population of the BO state 1 is larger than the population of the BO state 2.

Chapter 6

Summary and Outlook

The interplay between electronic and nuclear motion causes many fascinating phenomena in molecules and solids that usually cannot be described within the adiabatic approximation. The exact solution of the time-dependent Schrödinger equation for the coupled system of electrons and nuclei contains the complete information on the system but is currently out of computational reach except for the very simplest of molecules with a few degrees of freedom. To make numerical calculations feasible, the description usually involves approximations such as a classical or semiclassical description of the nuclear dynamics. In our journey towards a full ab initio description of the coupled electron-nuclear dynamics, we have presented an exact factorization of the complete electron-nuclear wavefunction into an electronic contribution, $\Phi_{\underline{\underline{\mathbf{R}}}}(\underline{\mathbf{r}},t)$, and a nuclear part, $\chi(\underline{\underline{\mathbf{R}}},t)$, that leads to a rigorous separation of electronic and nuclear motion (Chapter 2). The electronic and nuclear wavefunctions retain the usual probabilistic meaning, i.e., the exact nuclear N_n-body density is $|\chi(\underline{\underline{\mathbf{R}}},t)|^2$ while $|\Phi_{\underline{\underline{\mathbf{R}}}}(\underline{\mathbf{r}},t)|^2$ represents the exact conditional probability of finding the electrons at $\underline{\mathbf{r}}$, given the nuclear configuration $\underline{\underline{\mathbf{R}}}$. The equations of motion that the electronic and nuclear wavefunctions satisfy are given in (2.29)-(2.34), and show explicitly how the electronic and nuclear systems are coupled through the rigorous concepts of the time-dependent potential energy surface (2.33) and the time-dependent vector potential (2.34) as well as the electron-nuclear coupling operator (2.32).

The crucial point of this representation is that it provides a *unique* definition of the time-dependent potential energy surface and time-dependent vector potential (unique up to within a gauge transformation): If one wants the TD many-body Schrödinger

equation (2.30) to give the correct N_n-body density and current density of the nuclei, then the scalar potential and the vector potential *must* be given by eq. (2.33) and (2.34). There is no other choice apart from the gauge. That means that with any advanced technique that yields the molecular wavefunction, $\Psi(\underline{\mathbf{r}}, \underline{\underline{\mathbf{R}}}, t)$, one can evaluate the time-dependent potential energy surface and vector potential by first calculating the factors from Eqs. (2.26)-(2.27) and then evaluating the TDPES and vector potential from Eqs. (2.33)-(2.34).

We have shown a detailed study of the TDPES in two cases (Chapter 4). First, we have presented generic features of the exact TDPES for situations in which, according to the standard BO expansion framework, significant non-adiabatic transitions occur and the nuclear wave-packet splits at the avoided crossing of two BOPESs. For the one-dimensional model system studied here, the TDPES is the only potential that governs the dynamics of the nuclear wavefunction (the vector potential can be gauged away) and provides us with an alternative way of visualizing and interpreting the non-adiabatic processes. We have shown that the TDPES is characterized by two generic features: (i) in the vicinity of the avoided crossing the TDPES becomes identical with a diabatic PES in the direction of the wave-packet motion, (ii) far from the avoided crossing the TDPES as a function of nuclear coordinates, is piecewise parallel to different BOPESs and exhibits steps in between. The latter feature holds after the wave-packet branches and leaves the avoided crossing. These features of the TDPES support the use of diabatic surfaces as the driving potential when a wave-packet approaches a region of strong NAC. Moreover, they are in agreement with the semi-classical picture of non-adiabatic nuclear dynamics that suggests calculating the classical forces acting on the nuclei according to *the gradient of only one of the BOPESs*. We expect that these findings will ultimately lead to improved algorithms for the mixed quantum-classical treatment of electrons and nuclei.

Next, we have studied the one-dimensional H_2^+ molecule in an oscillating electric field and shown that the TDPES is a powerful tool to analyze and interpret different types of dissociation processes. By studying the shape and evolution of the TDPES, comparing classical dynamics in this exact potential to the exact quantum dynamics, we were able to distinguish whether the dissociation proceeded via nuclear tunnelling or more directly in Coulomb-explosion. The example demonstrated the importance of capturing both quantum effects in nuclear motion and electron-nuclear coupling; the Hartree approach,

for example, despite treating the nuclei quantum mechanically, was unable to capture dissociation via tunnelling as the shape of its potential surface was completely wrong. For both cases presented here, the TDPES is the only potential determining the nuclear dynamics, exactly containing the coupling with electronic dynamics. In more general cases than the ones studied here, the vector potential cannot always be set to zero and together with the TDPES governs the time evolution of the nuclei.

From a practical point of view, Eqs. (2.29)-(2.34) are not easier to solve than the time-dependent Schrödinger equation for the full electron-nuclear system. Rather they form the rigorous starting point for making approximations, especially for the systematic development of (semi)classical approximations. As a first step on this path, we have proposed a mixed quantum-classical scheme (Chapter 5) by taking the classical limit of the nuclear dynamics in Eqs. (2.29)-(2.34). The classical force, thus arising, is expressed as a generalized form of a Lorentz-like force that contains the gradient of the TDPES, the time derivative of the vector potential and coupling of the nuclear velocity to a generalized magnetic-like field that is defined as the curl of all of the vector potentials as well as the cross couplings of all the nuclear velocities to the vector potentials of all of the nuclei. We have evaluated the performance of the scheme by studying the nuclear dynamics through an avoided crossing in the Shin-Metiu model and showed that the result of the MQC scheme is in close agreement with the exact calculations in reproducing the nuclear kinetic energy and occupation of the BO states, especially using multiple trajectories. The domain of validity of the classical limit of the nuclear motion is investigated analytically and numerically.

A direction for future research is to capture some nuclear quantum effects by a semi-classical or quasiclassical procedure built on the exact foundational equations presented here without using the adiabatic basis. Another direction is to use the formalism as a possible starting point to develop electron-nuclear correlation functionals in a density-functionalized version of the electron-nuclear problem [96]. A promising route is to develop a time-dependent generalization of the optimized effective potential scheme proposed in Ref [33, 34].

The factorization, presented here, is a natural extension of the work of Hunter [1] and, Gidopoulos and Gross [33, 34], in which an exact decomposition was developed for the static problems. Both in the static and in the time-dependent cases, the factorization

leads to an exact definition of the PES, and also of the vector potential. In Chapter 3, we have investigated the exact PES in fully non-adiabatic situations, i.e., when the corresponding BOPESs exhibit points of avoided crossings or conical intersections. We have shown that the exact PESs have no conical intersection and behave in a similar way to the diabatic PESs. This is also in agreement with the results of Chapter (4) for the time-dependent case. These results may challenge the existence of the Berry-phase as an exact feature of molecular systems.

The alternative representation of the full electron-nuclear wavefunction in the factorized form, presented in this work, lends itself as a rigorous starting point to approach the coupled electron-nuclear dynamics in various different situations. For instance, the complete electron-nuclear wavefunction can be equally factorized into a nuclear contribution, $\chi_{\underline{\underline{\mathbf{r}}}}(\underline{\underline{\mathbf{R}}}, t)$, and an electronic part, $\Phi(\underline{\underline{\mathbf{r}}}, t)$, in which the nuclear part, parametrically depends on the electronic configuration, $\underline{\underline{\mathbf{r}}}$, and satisfies the PNC for every $\underline{\underline{\mathbf{r}}}$ and at any time. In this case the TDPES and time-dependent vector potential appear in a TDSE that describes the time evolution of the electronic wavefunction that reproduces the exact electronic density and current density of the complete system. These potentials account for the coupling of the electronic sub-system to the nuclear sub-system in a formally exact way and may lead to a better understanding of electronic processes in attosecond lasers such as the laser-induced localization of the electron in H_2^+ [97].

Appendix A

Generalized Force

In this appendix, we provide the details of the derivation of the generalized classical force presented in (5.32). Starting with the classical Hamiltonian (5.26):

$$H_n = \sum_{\nu=1}^{N_n} \frac{\left|\mathbf{P}_\nu^c + \mathbf{A}_\nu(\underline{\underline{\mathbf{R}}}^c(t))\right|^2}{2M_\nu} + \epsilon(\underline{\underline{\mathbf{R}}}^c, t), \tag{A.1}$$

we obtain the classical nuclear equation of motions using the Hamilton's equations

$$\dot{\mathbf{R}}_\nu = \frac{\partial H_n}{\partial \mathbf{P}_\nu} = \frac{\mathbf{P}_\nu + \mathbf{A}_\nu}{M_\nu} \equiv \mathbf{V}_\nu \tag{A.2}$$

$$\begin{aligned} \dot{\mathbf{P}}_\nu = -\frac{\partial H_n}{\partial \mathbf{R}_\nu} &= -\nabla_\nu \epsilon - \sum_{\nu'} \frac{\mathbf{P}_{\nu'} + \mathbf{A}_{\nu'}}{M_{\nu'}} \cdot \frac{\partial \mathbf{A}_{\nu'}}{\partial \mathbf{R}_\nu} \\ &= -\nabla_\nu \epsilon - \sum_{\nu'} \mathbf{V}_{\nu'} \cdot \frac{\partial \mathbf{A}_{\nu'}}{\partial \mathbf{R}_\nu}. \end{aligned} \tag{A.3}$$

Taking another time-derivative of the coordinate, then gives

$$M_\nu \frac{d^2\mathbf{R}_\nu}{dt^2} = \dot{\mathbf{P}}_\nu + \frac{\partial \mathbf{A}_\nu}{\partial t} + \sum_{\nu'} \mathbf{V}_{\nu'} \cdot \frac{\partial \mathbf{A}_\nu}{\partial \mathbf{R}_{\nu'}} \tag{A.4}$$

where we have used

$$\frac{d}{dt} = \frac{\partial}{\partial t} + \sum_{\nu'} \mathbf{V}_{\nu'} \cdot \nabla_{\nu'}. \tag{A.5}$$

Replacing $\dot{\mathbf{P}}_\nu$ in (A.4) with (A.3) leads to

$$M_\nu \frac{d^2 R_\nu^i}{dt^2} = E_\nu^i - \sum_{\nu'} \sum_{j=1}^{3} V_{\nu'}^j \left(\frac{\partial A_\nu^i}{\partial R_{\nu'}^j} - \frac{\partial A_{\nu'}^j}{\partial R_\nu^i} \right), \tag{A.6}$$

where

$$\mathbf{E}_\nu = -\nabla_\nu \epsilon + \frac{\partial \mathbf{A}_\nu}{\partial t}. \tag{A.7}$$

Here, Latin letters such as i and j refer to the Cartesian component of a vector. In order to write the second part on the l.h.s of Eq. A.6 in a closed form we define

$$\mathbf{B}_{\nu\nu'} = \nabla_\nu \times \mathbf{A}_{\nu'} \rightarrow B^k_{\nu\nu'} = \epsilon^{klm} \frac{\partial A^m_{\nu'}}{\partial R^l_\nu}, \tag{A.8}$$

hence,

$$\begin{aligned} (\mathbf{V}_{\nu'} \times \mathbf{B}_{\nu\nu'})^i &= \left(\epsilon_{kij} V^j_{\nu'}\right) \left(\epsilon^{klm} \frac{\partial A^m_{\nu'}}{\partial R^l_\nu}\right) \\ &= \sum_{jlm} \left(\delta_{il}\delta_{jm} - \delta_{im}\delta_{lj}\right) V^j_{\nu'} \frac{\partial A^m_{\nu'}}{\partial R^l_\nu} \\ &= \sum_j \left(V^j_{\nu'} \frac{\partial A^j_{\nu'}}{\partial R^i_\nu} - V^j_{\nu'} \frac{\partial A^i_{\nu'}}{\partial R^j_\nu} \right). \end{aligned} \tag{A.9}$$

Therefore,

$$\sum_j V^j_{\nu'} \frac{\partial A^j_{\nu'}}{\partial R^i_\nu} = (\mathbf{V}_{\nu'} \times \mathbf{B}_{\nu\nu'})^i + (\mathbf{V}_{\nu'} \cdot \nabla_\nu) A^i_{\nu'}, \tag{A.10}$$

and

$$\sum_j V^j_{\nu'} \frac{\partial A^i_\nu}{\partial R^j_{\nu'}} = (\mathbf{V}_{\nu'} \cdot \nabla_{\nu'}) A^i_\nu. \tag{A.11}$$

Plugging (A.10) and (A.11) into (A.6) leads to

$$M_\nu \dot{\mathbf{V}}_\nu = \mathbf{E}_\nu + \sum_{\nu'\nu} \mathbf{F}_{\nu\nu'}, \tag{A.12}$$

where

$$\begin{aligned} \mathbf{F}_{\nu\nu'}(\underline{\underline{\mathbf{R}}}^c) &= -\mathbf{V}_{\nu'} \times \mathbf{B}_{\nu\nu'}(\underline{\underline{\mathbf{R}}}^c) \\ &+ \left[(\mathbf{V}_{\nu'} \cdot \nabla_{\nu'}) \mathbf{A}_\nu(\underline{\underline{\mathbf{R}}}^c) - (\mathbf{V}_{\nu'} \cdot \nabla_\nu) \mathbf{A}_{\nu'}(\underline{\underline{\mathbf{R}}}^c) \right]. \end{aligned} \tag{A.13}$$

Bibliography

[1] G. Hunter, International Journal of Quantum Chemistry **9**, 237 (1975).

[2] H. Nakamura, *Nonadibatic Transition. Concepts, Basic Theories and Applications*, world scientific ed. (PUBLISHER, 2002).

[3] W. Domcke, D. R. Yarkony, and H. Köppel, *Conical Intersections. Electronic Structure, Dynamics and Spectroscopy*, world scientific ed. (PUBLISHER, 2004).

[4] W. Domcke, and D. R. Yarkony, Annu. Rev. Phys. Chem. **63**, 325 (2012).

[5] P. Cong, G. Roberts, J. L. Herek, A. Mohktari, and A. H. Zewail, J. Phys. Chem. **100**, 7832 (1996).

[6] T. J. Martinez, and R. D. Levine, Chem. Phys. Lett. **259**, 252 (1996).

[7] G. Hanna, and R. Kapral, J. Chem. Phys. **122**, 244505 (2005).

[8] M.Born, and R. J. Oppenheimer, Annalen der Physik **389**, 457 (1927).

[9] Bandrauk, A.D., and H. Kono, "Molecules in intense laser fields: nonlinear multiphoton spectroscopy and near-femtosecond to sub-femtosecond (attosecond) dynamics", in Advances in MultiPhoton Processes and Spectroscopy, vol. 15, edited by S.H. Lin, A.A. Villaeys, and Y. Fujimura, pp. 147–214 (World Scientific, Singapore, 2003).

[10] Marangos, J.P., "Molecules in a strong laser field", in Atoms and Plasmas in Super-Intense Laser Fields, edited by D. Batani, C. J. Joachain, and S. Martellucci, SIF Conference Proceedings, vol. 88, pp. 213–243 (Societ'a Italiana di Fisica, Bologna, 2004).

[11] M. Kling, C. Siedschlag, A. Verhoef, J. Khan, M. Schultze, T. Uphues, Y. Ni, M. Uiberacker, M. Drescher, F. Krausz *et al.*, Science **312**, 246 (2006).

[12] W. Duncan, and O. Prezhdo, Annu. Rev. Phys. Chem. **58**, 143 (2007).

[13] C. Rozzi et al., unpublished.

[14] M. Wohlgemuth, and V. B.-K. and. R. Mitrić, J. Chem. Phys. **135**, 054105 (2011).

[15] A. L. Sobolewski, W. Domcke, C. Dedonder-Lardeux, and C. Jouvet, Phys. Chem. Chem. Phys. **4**, 1093 (2002).

[16] T. S. Rose, M. J. Rosker, and A. H. Zewail, J. Chem. Phys. **91**, 7415 (1989).

[17] A. Abedi, N. T. Maitra, and E. K. U. Gross, Phys. Rev. Lett. **105**, 123002 (2010).

[18] A. Abedi, N. T. Maitra, and E. K. U. Gross, The Journal of Chemical Physics **137**, 22A530 (2012).

[19] G. Hunter, Int. J. Quantum Chem **9**, 237 (1975).

[20] A. Abedi, F. Agostini, Y. Suzuki, and E. Gross, Phys. Rev. Lett. **110**, 263001 (2013).

[21] F. Agostini, A. Abedi, Y. Suzuki, and E. Gross, Molecular Physics **111**, 3625 (2013).

[22] A. Abedi, F. Agostini, and E. Gross, Europhysics Letters **106**, 33001 (2014).

[23] S. Chelkowski, T. Zuo, O. Atabek, and A. Bandrauk, Phys. Rev. A. **52**, 2977 (1995).

[24] S. Chelkowski, C. Foisy, and A. Bandrauk, Phys. Rev. A **57**, 1176 (1998).

[25] C. A. Mead, Rev. Mod. Phys. **64**, 51 (1992).

[26] B. Kendrick, The Journal of Physical Chemistry A **107**, 6739 (2003).

[27] R. Resta, Journal of Physics: Condensed Matter **12**, R107 (2000).

[28] F. Bouakline, S. Althorpe, P. Larregaray, and L. Bonnet, Molecular Physics **108**, 969 (2010).

[29] S. Althorpe, J. Chem. Phys. **124**, 084105 (2006).

[30] M. Born, K. Huang, Dynamical Theory of Crystal Lattices, Oxford University, New York, 1954.

[31] L. S. Cederbaum, "Born-Oppenheimer Approximation and Beyond", in Advanced Series in Physical Chemistry, Vol. 15, "Conical intersections: electronic structure, dynamics and spectroscopy", edited by Wolfgang Domcke, David Yarkony and Horst Köppel, pp. 3–40 (World Scientific, Singapore, 2004).

[32] M. Baer, Ber. Bunsenges. Phys. Chem. **86**, 448 (1982).

[33] N. Gidopoulos, and E. Gross, Arxiv preprint cond-mat/0502433 (2005).

[34] N. Gidopoulos, and E. Gross, Phil. Trans. R. Soc. A **372**, 20130059 (2014).

[35] H. Meyer, U. Manthe, and L. Cederbaum, Chemical Physics Letters **165**, 73 (1990).

[36] G. Hunter, International Journal of Quantum Chemistry **17**, 133 (1980).

[37] J. Czub, and L. Wolniewicz, Molecular Physics **36**, 1301 (1978).

[38] I. Barth, H. Hege, H. Ikeda, A. Kenfack, M. Koppitz, J. Manz, F. Marquardt, and G. Paramonov, Chemical Physics Letters **481**, 118 (2009).

[39] D. M. Bishop, and G. Hunter, Molecular Physics **30**, 1433 (1975).

[40] G. Hunter, International Journal of Quantum Chemistry **19**, 755 (1981).

[41] C. A. Mead, and D. G. Truhlar, J. Chem. Phys. **70**, 2284 (1979).

[42] Y. DR., Rev. Mod. Phys. **68**, 985 (1996).

[43] G. Herzberg, and H. Longuet-Higgins, Discuss. Faraday Soc. **35**, 77 (1963).

[44] J. Javanainen, J. H. Eberly, and Q. Su, Phys. Rev. A **38**, 3430 (1988).

[45] D. Lappas, A. Sanpera, J. Watson, K. Burnett, P. Knight, R. Grobe, and J. Eberly, Journal of Physics B: Atomic, Molecular and Optical Physics **29**, L619 (1996).

[46] D. M. Villeneuve, M. Y. Ivanov, and P. B. Corkum, Phys. Rev. A **54**, 736 (1996).

[47] A. D. Bandrauk, and N. H. Shon, Phys. Rev. A **66**, 031401 (2002).

[48] T. Kreibich, R. van Leeuwen, and E. Gross, Chemical physics **304**, 183 (2004).

[49] D. G. Lappas, and R. van Leeuwen, J. Phys. B: At. Mol. Opt. Phys. **31**, L249 (1998).

[50] M. Lein, T. Kreibich, E. K. U. Gross, and V. Engel, Phys. Rev. A **65**, 033403 (2002).

[51] T. Kreibich, M. Lein, V. Engel, and E. K. U. Gross, Phys. Rev. Lett. **87**, 103901 (2001).

[52] A. D. Bandrauk, and H. Lu, Phys. Rev. A **72**, 023408 (2005).

[53] S. Chelkowski, A. Conjusteau, T. Zuo, and A. D. Bandrauk, Phys. Rev. A **54**, 3235 (1996).

[54] S. Shin, and H. Metiu, J. Chem. Phys. **102**, 23 (1995).

[55] M. Berry, Proceedings of the Royal Society of London. A. Mathematical and Physical Sciences **392**, 45 (1984).

[56] A. Abedi, N. T. Maitra, and E. K. U. Gross, J. Chem. Phys. **137**, 22A530 (2012).

[57] S. K. Ghosh, and A. K. Dhara, Phys. Rev. A **38**, 1149 (1988).

[58] E. Runge, and E. K. U. Gross, Phys. Rev. Lett. **52**, 997 (1984).

[59] J. A. Fleck, J. R. Morris, and M. D. Feit, Appl. Phys. A 10, 129 (1976).

[60] J. Tully, and R. Preston, J. Chem. Phys. **55**, 562 (1971).

[61] R. K. S. Nielsen, and G. Ciccotti, J. Chem. Phys. **112**, 6543 (2000).

[62] E. J. Heller, J. Chem. Phys. **62**, 1544 (1975).

[63] K. C. Kulander, Phys. Rev. A **35**, 445 (1987).

[64] H. Kono, Y. Sato, N. Tanaka, T. Kato, K. Nakai, S. Koseki, and Y. Fujimura, Chemical physics **304**, 203 (2004).

[65] J. Maddox, Nature **373**, 469 (1995).

[66] A. Anderson, Phys. Rev. Lett. **74**, 621 (1995).

[67] R. Kapral, and G. Ciccotti, J. Chem.Phys. **110**, 8916 (1999).

[68] I. V. Aleksandrov, Z. Naturforsch. Teil A **36**, 902 (1981).

[69] P. Pechukas, Phys. Rev. **181**, 166 (1969).

[70] J. C. Tully, and R. K. Preston, J. Chem. Phys. **55**, 562 (1971).

[71] H. D. Meyer, and W. H. Miller, J. Chem. Phys. **72**, 2272 (1980).

[72] J. C. Tully, J. Chem. Phys. **93**, 1061 (1990).

[73] J. C. Tully, in *Classical and quantum dynamics in condensed phase simulations*, *Proceedings of the international school of physics*, edited by B. B. Berne, G. Ciccotti, and D. F. Coker (PUBLISHER, 1997).

[74] M. Barbatti, Advanced Review **1**, 620 (2011).

[75] P. J. Kuntz, J. Chem. Phys. **95**, 141 (1991).

[76] A. D. McLachlan, Mol. Phys. **8**, 39 (1964).

[77] J. E. Subotnik, J. Chem. Phys. **132**, 134112 (2010).

[78] K. Drukker, J. Comput. Phys. **153**, 225 (1999).

[79] Y. Wu, and M. F. Herman, J. Chem. Phys. **123**, 1 (2005).

[80] D. F. Coker, and L. Xiao, J. Chem. Phys. **102**, 496 (1995).

[81] B. F. E. Curchod, I. Tavernelli, and U. Rothlisberger, Phys. Chem. Chem. Phys. **13**, 3231 (2011).

[82] O. Prezhdo, and P. J. Rossky, J. Chem. Phys. **107**, 825 (1997).

[83] J. H. van Vleck, Proc. Natl. Acad. Sci. **14**, 178 (1928).

[84] H. Goldstein, *Classical Mechanics*, 2nd ed. (Addison-Wesley, New York, 1988).

[85] S. A. Chin, Phys. Rev. E **77**, 066401 (2008).

[86] B. Lassagne, Y. Tarakanov2, J. Kinaret2, D. Garcia-Sanchez1, and A. Bachtold, Science **325**, 1107 (2009).

[87] G. A. Steele, A. K. Httel, B. Witkamp, M. Poot, H. B. Meerwaldt, L. P. Kouwenhoven, and H. S. J. van der Zant, Science **325**, 1103 (2009).

[88] R. S. Sorbello, Solid State Phys. **51**, 159 (1998).

[89] D. Dundas, E. J. McEniry, and T. N. Todorov, Nat. Nanotechnol. **4**, 99 (2009).

[90] T. N. Todorov, D. Dundas, and E. J. McEniry, Phys. Rev. B **81**, 075416 (2010).

[91] J. T. Lü, M. Brandbyge, and P. Hedegard, Nano Lett. **10**, 1657 (2010).

[92] T. N. Todorov, D. Dundas, A. T. Paxton, and A. P. Horsfield, J. Nanotechnol. **2**, 727 (2011).

[93] J.-T. Lü, T. Gunst, M. Brandbyge, and P. Hedegard, J. Nanotechnol. **2**, 814 (2011).

[94] N. Bode, S. V. Kusminskiy, R. Egger, and F. von Oppen, J. Nanotechnol. **3**, 144 (2012).

[95] N. Bode, S. V. Kusminskiy, R. Egger, and F. von Oppen, Phys. Rev. Lett. **107**, 036804 (2011).

[96] T. Kreibich, and E. K. U. Gross, Phys. Rev. Lett. **86**, 2984 (2001).

[97] F. Kelkensberg, G. Sansone, M. Ivanov, and M. Vrakking, Phys. Chem. Chem. Phys. **13**, 8647 (2011).

Deutsche Kurzfassung

Mit dem Ziel einer ab-initio-Beschreibung von Systemen aus Atomkernen und Elektronen, welche sich in einem zeitabhängigen externen Potential bewegen, leiten wir eine exakte Faktorisierung der Wellenfunktion eines Systems in Elektronen - und Atomkernwellenfunktion her. Wir präsentieren die exakten Gleichungen für diese Wellenfunktionen, welche zu strikten Definitionen der zeitabhängigen Potentialfläche (TDPES) und des zeitabhängigen Vektorpotentials führen. Diese Behandlung des korrelierten Kern-Elektron-Vielköperproblems ist zudem sehr vorteilhaft, da die Kernwellenfunktion die N-Körper-Teilchendichte und die N-Körper-Teilchenstromdichte der Gesamtwellenfunktion reproduziert. Die Zeitentwicklung der Kernwellenfunktion ist allein durch die TDPES und das zeitabhängige Vektorpotential bestimmt, welche bis auf eine Eichtransformation *eindeutig* bestimmt sind. Mit anderen Worten: Möchte man eine zeitabhängige Schrödingergleichung, welche die N-Körper-Teilchendichte und N-Körper-Teilchenstromdichte reproduziert, sind die darin auftretenden Potentiale (bis auf Eichtransformation) durch die TDPES und das zeitabhängige Vektorpotential eindeutig gegeben. Eine andere Wahl der Potentiale ist nicht möglich. Wir untersuchen den Zusammenhang dieser exakten Faktorisierung mit der Born-Oppenheimer-Entwicklung. Des weiteren untersuchen wir die exakte TDPES an zwei relevanten Beispielen: Moleküle in starken Feldern und die Aufspaltung des Kern-Wellenpackets an vermiedenen Kreuzungen von Born-Oppenheimer-Flächen. Wir zeigen wie die TDPES des H_2^+ Moleküls nachdem es einem Laser-Feld ausgesetzt wurde hilft, verschiedene Dissoziationsmechanismen zu identifizieren. Andrerseits zeigen wir, dass die TDPES Stufen zwichen stückweise adiabatisch geformten Potentialflächen entwickelt, wenn sich ein Kern-Wellenpacket an einer vermiedenen Kreuzung zweier Born-Oppenheimer-Flächen aufspaltet. Diese Untersuchungen bilden die Basis (grundlegende Bewegungsgleichungen sowie das Verständnis der Kopplungspotentiale) um Näherungen und insbesondere (semi-)klassische Näherungen

systematisch zu entwickeln. Wir entwickeln, ausgehend von den exakten Bewegungsgleichungen, eine Methode, die es erlaubt die Dynamik des gekoppelten Systems aus Elektronen und Kernen zu behandeln, indem für die Bewegung der Kerne der klassische Limes gebildet wird. Wir bewerten die Qualität dieses Ansatzes indem wir mit numerisch exakten Ergebnissen vergleichen und führen eine genaue Untersuchung des klassischen Grenzfalls der Kernbewegung durch.

Um die exakte Faktorisierung im statischen Fall [1] besser zu verstehen, untersuchen wir die exakten statischen Potentialflächen in Situationen starker Kopplung der entsprechenden adiabatischen Potentialflächen durch konische durchschneidungen oder vermiedene Kreuzungen. Wir zeigen, dass sich die exakten Potentialflächen in diesen Fällen ähnlich wie die diabatischen Flächen verhalten.

Acknowledgments

At the closing part of this thesis I would like to express my sincere gratitude to all those great people who have supported me to accomplish this work.

First and foremost, I would like to express my best gratitude to my PhD advisor, Prof. E. K. U. Gross. Thank you Hardy for giving me the opportunity and absolute freedom to follow my scientific interests. I learned a lot from your special way of thinking, understanding and approaching physics. Thank you for your great ideas, supports, trust, and for making the Gross-group such a warm and lovely place. It was a great pleasure to be part of it!

I am also thankful to all members of the committee for the time and effort they invested in reviewing my work, specially Prof. J. Bosse who accepted the burden of being my second referee.

My very special thanks go to my collaborators, Dr. Federica Agostini, Dr. Yasumitsu Suzuki, Dr. Seung Kyu Min, Prof. Neepa Maitra, Prof. César Proetto and Prof. Angel Rubio. I very much enjoyed working with them and appreciated their deep understanding of physics.

Many thanks to my former and current colleagues in AG-Gross Berlin and the Gross-department in Halle for such a wonderful, friendly and fun working environment. Specially, I would like to thank Gabi Herrmann, the group secretary in Berlin, for her kindness and support from the moment I landed in Berlin through all these years.

I would like to thank my officemates, Jan, Stefano, Florian and Danilo. I very much enjoyed their company and our discussions about physics and everyday life.

As this work was done in both Berlin and Halle I would like to thank all the staff members at the physics department of the Freie Universität in Berlin and the Max-Planck Institute für Mikrostrukturphysik in Halle. Without their efforts, there would have been hardly any time left for research.

Words fail me to express my appreciation to my family for their persistent support and love that has been an unstinting help and courage in this adventure. Hedieh, Madjid, Nima and Navid, thank you for being always there for me.

I would like to thank my parents-in-law, Ghadireh and Houshang, for their support and kindness.

A very special thanks to all my amazing friends for their support and friendship. In particular, I would like to thank Ali Akbari, Ali Barandov, Hossein, Javad, Maziar, Pari, Raheleh and Somi for being there for me whenever I needed them and also for all the wonderful moments we shared together.

I would also like to thank Mrs. Muriel Hopwood for proofreading my thesis.

Last but not least, my very special thanks to my best friend, my classmate, my colleague and my wife, Elham! Your ongoing love, care, kindness and support has kept me going specially during difficult times. I am also thankful for your points and corrections in the proofreading of my thesis.

Lebenslauf

For reasons of data protection, the Curriculum vitae is not published in the online version

Publications

• Abedi, A., Maitra, N. T., Gross, E. K. U.

Exact factorization of the time-dependent electron-nuclear wave function

Physical Review Letters **105**, 123002 (2010)

This paper was selected as an Editors' Suggestion.

• Abedi, A., Maitra, N. T., Gross, E. K. U.

Correlated electron-nuclear dynamics: Exact factorization of the molecular wavefunction

Journal of Chemical Physics **137**, 22A530 (2012)

This paper was selected by the Editors among a few of the many notable JCP articles published in 2012 that present ground-breaking research.

• Abedi, A., Maitra, N. T., Gross, E. K. U.

Response to "Comment on Correlated electron-nuclear dynamics: Exact factorization of the molecular wavefunction" [J. Chem. Phys.139, 087101 (2013)]

Journal of Chemical Physics **139**, 087102 (2013)

• Abedi, A., Agostini, F., Suzuki, Y., Gross, E. K. U.

Dynamical steps that bridge piecewise adiabatic shapes in the exact time-dependent potential energy surface

Physical Review Letters **110**, 263001 (2013)

• Agostini, F., Abedi, A., Suzuki, Y., Gross, E. K. U.

Mixed quantum-classical dynamics on the exact time-dependent potential energy surface: A fresh look at non-adiabatic processes

Molecular Physics **111** (22-23), 3625-3640 (2013)

• Abedi, A., Agostini, F., Gross, E. K. U.

A Mixed Quantum-Classical Scheme Based on the Exact Factorization of the Time-Dependent Electron-Nuclear Wave-Function

Europhysics Letters **106** (3), 33001 (2014)

• Min, S. K., Abedi, Kim, K. S., F., Gross, E. K. U.

Is the molecular Berry phase an artifact of the Born-Oppenheimer approximation?

arXiv preprint arXiv:1402.0227 (2014)

• Suzuki, Y., Abedi, A., Maitra, N. T., Yamashita, K., Gross, E. K. U.

Electronic Schrödinger equation with nonclassical nuclei

Physical Review A **89**, 040501(R) (2014)